TEMPERATURE-DEPENDENT THERMOELASTIC ANALYSIS OF MULTI-DIMENSIONAL FUNCTIONALLY GRADED MATERIALS

by

Yangzhan Yang

B.S., Harbin Institute of Technology, 2008

M.S., Harbin Institute of Technology, 2010

Submitted to the Graduate Faculty of

Swanson School of Engineering in partial fulfillment

of the requirements for the degree of

Doctor of Philosophy

University of Pittsburgh

2015

UNIVERSITY OF PITTSBURGH

SWANSON SCHOOL OF ENGINEERING

This dissertation was presented

by

Yangzhan Yang

It was defended on

November 24th, 2015

and approved by

John C. Brigham, Ph.D., Assistant Professor, Department of

Civil and Environmental Engineering

Ian Nettleship, Associate Professor, Ph.D., Department of

Mechanical Engineering and Materials Science

Guofeng Wang, Ph.D., Associate Professor, Department of

Mechanical Engineering and Materials Science

Dissertation Director: William S. Slaughter, Ph.D., Associate Professor, Department of

Mechanical Engineering and Materials Science

TEMPERATURE-DEPENDENT THERMOELASTIC ANALYSIS OF MULTI-DIMENSIONAL FUNCTIONALLY GRADED MATERIALS

Yangzhan Yang, Ph.D.

University of Pittsburgh, 2015

Functionally graded materials (FGMs) are advanced composites with material compositions varying continuously as a function of spatial position. The gradual change of material properties can be tailored to meet special requirements of different working environments. One of the main applications of FGMs is as thermal barrier coatings (TBCs) at high temperatures. Functionally graded TBCs are usually made with a mixture of ceramic at the top surface and metal at the bottom. The compositions of these one-dimensional FGMs are varied through the thickness with an optimized variation of volume fractions.

Under some practical conditions, such as the outer surface of an airplane, temperature changes drastically in two or three directions. Conventional one-dimensional FGMs have been shown to likely fail under these extreme circumstances. Therefore, it is necessary to develop FGMs with material properties varying in other dimensions to achieve multi-directional high-temperature resistance. However, this type of FGMs is not well studied due to their computational and experimental complexities. Based on such facts, we propose to study the thermoelastic behaviors of multi-dimensional FGMs. Most of the current researches assume temperature-independent material properties and uses simple rule of mixtures to estimate material properties at different positons, in order to simplify their calculations, but these assumptions ignore temperature effects as well as microscopic particle interactions and thus can be unrealistic. So we choose to include temperature dependent material properties to achieve

better accuracy. Also, a self-consistent mean-field micromechanics Wakashima-Tsukamoto (WT) model is used in this analysis to estimate physical properties of the FGM, which has been proved to produce more accurate results.

We propose to study a multi-dimensional FGM plate, composed of ZrO_2, Ti-6Al-4V and Al_2O_3. Finite element method is used to analyze temperature distributions, thermal stresses and failure criteria of the plate under steady state, heating and sudden cooling conditions. Simply supported and clamped boundary conditions are applied in the analysis. We also studied the influences of volume fraction laws and plate shape on the thermoelastic performance of FGMs. As a result, we obtained an optimal FGM structure by analyzing failure criteria.

TABLE OF CONTENTS

LIST OF TABLES

LIST OF FIGURES

PREFACE

First and foremost, I would like to sincerely thank my advisor, Dr. William S. Slaughter, for his invaluable guidance, understanding and support. His profound knowledge, patient instructions and constant encouragements were the biggest driving forces to make this dissertation happen. From him, I learnt the highest standard of integrity in research as well as in life.

I would also like to express my deepest gratitude to the Department of Mechanical Engineering and Materials Science of University of Pittsburgh for the opportunity to study and research here. My special thanks to all the department faculty members and students. They provided an excellent academic and research atmosphere.

I thank my dissertation committee members – Dr. John C. Brigham, Dr. Ian Nettleship and Dr. Guofeng Wang for their helpful guidance and insightful suggestions.

I also thank ANSYS Inc. for the opportunity of internship. This experience turned out to be very valuable in my research.

Last but not the least, my deepest thanks to my family. Their love and support are my biggest motivation.

1.0 INTRODUCTION

1.1 BACKGROUND

Functionally graded materials (FGMs) are heterogeneous composites with tailored microstructures to improve overall performance. By varying the relative volume fractions, physical states and geometrical configurations of two or more constituent materials, FGMs can exhibit a continuous spatial variation of material properties. FGMs were first introduced in 1984 (M. NIINO, 1984) when continuous texture control was used to manufacture reusable rocket engine. The concept of FGM is not new to nature. From the stems of plants to the trunks of trees, from seashells to animal bones, they all have continuous varying structures as a self-optimizing mechanism to adapt to the harsh living environments. Scientists are inspired to develop newer generation of FGMs with superior qualities to traditional materials. The continuous change in the microstructure of FGMs distinguishes them from the traditional composite, which have a mismatch of material properties due to two distinct materials bonding together at the interface. As a result, debonding may happen under high thermal loadings and cracks are likely to initiate at interfaces. Additional problems include the presence of residual thermal stresses because of the difference in coefficients of thermal expansion of different materials. In FGMs, these problems may be eliminated or reduced by gradually varying the volume fraction of each phase rather than abruptly changing them across an interface. Furthermore, because FGM structures are

tailored for specific applications, advantages of their individual constituents are usually combined and their limitations are reduced. For example, in metal/ceramic FGM, the toughness of a metal can be combined with the high thermal and corrosion resistance of ceramic, without any compromise in the toughness of the metal side or the refractoriness of the ceramic side.

FGMs show great promise in applications where operating environments are challenging, including spacecraft heat shields, heat exchanger tubes, turbine blade, engine components, biological implant, wear resistant bulk material and coating, graded bandgap semiconductor and high power electrical contacts or even magnets.

One of the main applications of FGMs is as thermal barrier coatings (TBCs) at high temperatures. FGM TBCs have been proved to have the abilities to optimize temperature field, reduce thermal stress and enhance thermal resistance. A SiC/C FGM thermal barrier coating for a combustion chamber has been developed for a Japanese space shuttle (Tada, 1995). Repeated hot gas flow tests indicated that the FGM thermal barrier coating has high resistance to delamination and cracking at high temrperatures. ZrO_2/Ni FGM was used as TBC for a rocket engine(Y Kuroda, 1991) . No delamination was observed after 550 seconds of combustion. ZrO_2 stabilized with Y_2O_3 FGM was used as TBC for turbine blades (G. W. Goward 1994). It showed outstanding erosion and thermal shock resistance.

Cutting tools are often subjected to a wide range of loads that can not be handled by a homogenous material. They usually require extreme hardness at the surface of the cutting edges and a stronger and tougher base. Functionally graded WC/Co cutting tools is designed with a decreasing Co volume fraction from the surface to the interior, which leads to the hardness at the cutting tool's surface to be higher than its interior (Tobioka, 1989). This gradient in hardness

yields significantly higher damage and wear resistance than a traditional cutting tool with a homogeneous composition.

Functionally graded hydroxyapatite (HAp) coating on porous Ti-6Al-4V as orthopedic implant has been proved to bond with bones faster and has higher adhesive strength than traditional biomaterials (Oonishi, 1990). Dental implant composed of titanium plus HAp has been shown to have both good biocompatibility and mechanical toughness (Fumio Watari, 1995).

The fabrication of FGMs can be categorized into bulk, layer, preform and melt processing (Y. Miyamoto, 1999). The major distinction is the gradient is introduced into which object. Processing techniques can include single or multiple constructive or mass transport mechanisms, or a combination of them, in solid, liquid, or gaseous aggregation states. Bulk processing employs those methods that initially create a bulk matrix that has graded porosity, composition, or phase configuration. This is achieved largely by stacking of powder, fibers, or even sheets by means of normal gravity, centrifugal forces, pressure induced flow, spray or slurry deposition. The stacks are then consolidated either by pore elimination which results in their shrinkage, or infiltration, generally without any concomitant shrinkage. Layer processing includes spray deposition, cladding, chemical vapor deposition (CVD), electrodeposition, physical vapor deposition (PVD) such as electron beam PVD and sputtering,. Materials that do not contain gradients initially can be graded using preform processing. One preform methods is based on the traditional transport mechanisms which can create gradients in materials in solid state or liquid phase diffusion or gaseous flow. Another method is to apply external thermal or electrical fields. For example, thermal gradients can be applied to sintered porous materials to different local densities and electrical fields can produce a graded porosity when a porous preform is electrolytically dissolved. Compositions of FGMs can also be mixed under molten

state and then settled under gravity or centrifugal forces. However, the use of melt processing is very limited because of the challenge in controlling the formation of extended compositional gradients in the molten state.

1.2 THERMOELASTIC ANALYSIS OF FUNCTIONALLY GRADED MATERIALS

One of the main applications of FGMs is thermal barrier coating in high temperature environment. Extensive researches have been done to analyze the thermoelastic response of FGMs, with various methods. These methods can be divided into three primary classes: analytical, semi-analytical and numerical approaches.

Closed-form solutions are obtained for a simply supported FGM plate under normal and shear tractions (Zhong, 2008). The problem is formulated on the assumption that the elastic modulus depends on the z-coordinate along the thickness direction. Corresponding physical properties are expanded into Fourier series. The influence of different functionally graded models and plate configurations on the stress and displacement fields is studied. However, these solutions are only valid for some specific cases such as exponential or linear material model.

A semi-analytical solution is presented via a hybrid approach combining the state space method and the technique of differential quadrature (Ji Ying, 2009). The temperature field in the plate is determined according to the steady-state 3D thermal conduction. The approximate laminate model is employed to reduce the inhomogeneous plate into a homogeneous laminate that delivers a state equation with constant coefficients. Effects of gradient indices, volume fraction of ceramics and boundary conditions on the thermo-mechanical behavior of functionally graded plates are discussed.

Reddy (Reddy, 2000) developed a finite element model based on the third-order shear deformation plate theory for the analysis of simply supported through-thickness functionally graded plates under thermal-mechanical loading. The transition between the two materials is represented by means of a power series and material properties are approximated by the simple rule of mixtures. Numerical results were presented to show the effects of the power-law index and plate shape aspect ratio on volume fractions, plate deflections and stresses. It is concluded that the gradients in material properties play an important role in determining the response of FGM plates. Praveen and Reddy (G.N. Praveen, 1998) performed a geometrically nonlinear transient analysis of FGMs under thermal and mechanical loading. Nonlinear bending response of FGMs subjected to uniform pressure and thermal loading is studied by Na and Kim using a three dimensional finite element method (Kyungsu Na, 2006).

Other finite element formulations are also used in FGM studies. Chen used an eight node higher order elements in order to achieve better accuracy for thermal analysis (Chen Kang 2013). Node-based strain smoothing technique is used to improve calculation efficiency (H. Nguyen-Xuan, 2012). The recently developed mesh-free method is widely used to solve engineering problems (Li, 2000) (Belytschko, 1996) (L. F. Qian, 2004). A mesh-free kp-Ritz method is developed based on the first order shear deformation plate theory and the von Karman strain (X. Zhao, 2009). A mesh-free radial point interpolation method is used for static and dynamic analyses of FGM plate (K Y Dai, 2004). The effects of the constituent fraction exponent on static deflection as well as natural frequency are also investigated in detail using different FGM models.

1.3 FAILURE OF FUNCTIONALLY GRADED MATERIALS

When stress exceeds a critical value, failure may occur in FGMs. Due to ceramics' inherent brittle nature, defects or cracks may be introduced during the fabrication process and under the in-service loading conditions. Thus, it is important to investigate the fracture and damage properties of FGMs in the design, optimization and applications of FGMs.

Analytical methods can only be applied to a few cases with simple geometrical and loading conditions, because of FGM's complex material property variations. In general cases, numerical methods are required to solve fracture mechanics problems. There are many efforts on the computation of crack opening displacement, J-integral, fracture toughness (Chuanzeng Zhang 2004) (M. Nemat-Alla, 2000) (Ch. Zhang 2011). Nazari (Mohammad Bagher Nazari, 2011) calculated stress intensity factor in functionally graded plates under thermal shock. The results indicate stress intensity factor reaches its peak value a short while after the thermal shock. Many others focus on the simulation of crack paths and propagations (M. Steigemann 2010) (I.V. Ivanov, 2013; R.C. Batra, 2005).

Comparing to theoretical and numerical analyses, experimental investigations are relatively rare in FGM failure studies (Hill · R D Carpenter 2002; Jorge Abantobueno, 2006). (Alpay Oral, 2008) performed experiments on quasi-static crack initiation under mixed mode loading to evaluate the applicability of the maximum tangential stress criterion in predicting crack kinking in FGMs. Thermal fracture behavior of metal/ceramic FGMs was studied by (Akira Kawasaki, 2002). First orthogonal crack formed on the top surface during cooling, then transverse crack formed in the graded layer during heating, and transverse cracks grew subsequently and their coalescence eventually caused the ceramic coating to spall.

1.4 MOTIVATION

In many practical circumstances, temperature distributions in advanced machine components change drastically in two or three directions. For example, the temperature on the outer surface of an aircraft may range from 2066K from the nose to 1033K along the fuselage and from outer surface high temperature to room temperature inside the aircraft (Morris A. Steinberg, 1986). Conventional FGMs are likely to fail under these extreme conditions since all outer surfaces of the body have the same composition distributions. If the FGM has multi-dimensional gradient material properties, more effective high-temperature resistant material can be obtained. In other words, it is necessary to add one or more materials that have more strength, to the places that have maximum values of thermal stresses or the places where yielding is most likely to occur. Based on such facts we propose to study a multi-dimensional FGM whose material properties have two-dimensional variations.

Material properties may vary greatly at different temperatures. It is suggested by Noda (Noda, 1991) that temperature effects must be taken into account in order to perform more accurate analysis, so we choose to include temperature dependent material properties in our study to achieve more realistic results.

Most of the existing researches on FGMs use simple rule of mixtures to determine material properties. However, this method may not be accurate as it ignores the microscopic particle interactions. A self-consistent mean-field micromechanics Wakashima-Tsukamoto (WT) model is used in this analysis to estimate physical properties of the FGM, which has been proved to produce more accurate results (S. Kapuria, 2008) (J.R. Cho, 2001).

In this study, a multi-dimensional FGM plate comprised of ZrO_2, Ti-6Al-4V and Al_2O_3 with temperature-dependent material properties estimated by the modified WT model is analyzed

using finite element method. Temperature distributions, thermal stresses and failure criteria of the plate under steady state, heating and sudden cooling conditions are analyzed. Simply supported and clamped boundary conditions are investigated. We also analyzed other design parameters such as shape of the plate and volume fraction laws. As a result, we obtained the optimal volume fraction function and improved its high temperature thermoelastic performances.

2.0 MODELING OF MULTI-DIMENSIONAL FUNCTIONALLY GRADED MATERIALS

This chapter describes the construction of the multi-dimensional FGM plate model. The material properties are given as a function of temperature. Wakashima-Tsukamoto model is selected to calculate material properties at different spatial positions and modified to account for material compositions change.

2.1 ONE-DIMENSIONAL FUNCTIONALLY GRADED MATERIAL

One-dimensional (1D) functionally graded materials are the most commonly seen FGMs. They are widely used as thermal barrier coatings (TBCs) at high temperatures. Functionally graded TBCs are usually made with a mixture of ceramic at the top surface where the working temperature is high and metal at the bottom. The compositions of these one-dimensional FGMs are varied continuously through the thickness. For a FGM plate, assume the volume fractions of ceramic V_c and metal V_m are given by power law relations:

$$V_c = \left(\frac{\mathrm{z}}{t} \right)^n \tag{1}$$

$$V_m = 1 - V_c \tag{2}$$

Subscripts m and c denote the ceramic and metal constituent respectively, z is the coordinate along the thickness direction and t is the plate thickness, n is the power law index and n≥0. It is assumed that material compositions vary continuously from pure ceramic on the top surface to metal on the bottom. This power law relation describes how the plate is graded through the thickness. Figure 1 illustrates the ceramic volume fraction V_c with respect to different power law index values.

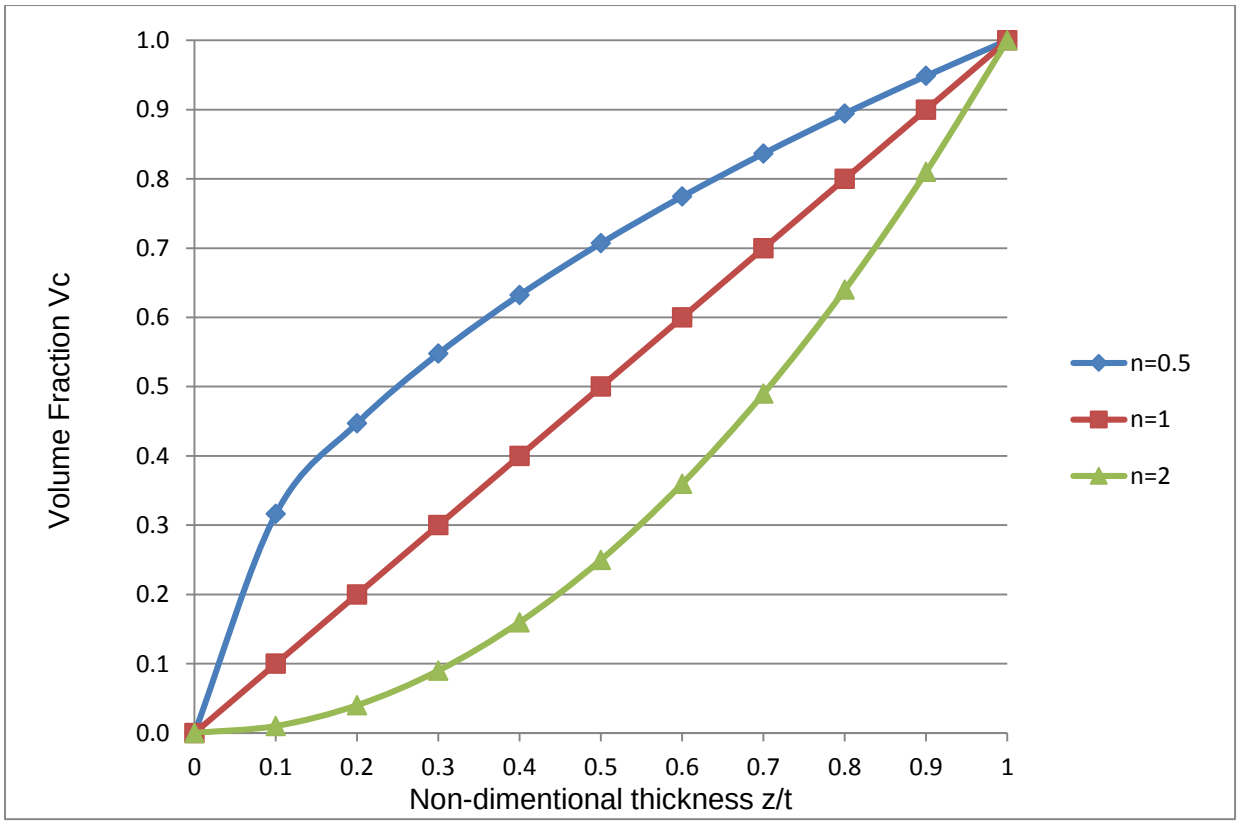

Figure 1. Variation of the ceramic volume fraction through the plate thickness

If n=0, the plate is made of pure ceramic and if n→ ∞, the plate is fully metal. Because z/t<1, when n<1, the plate is ceramic rich, when n>1, the plate is metal rich and when n=1, the

material composition changes linearly through the thickness. Assume thermal conductivity of the plate k follows the simple rule of mixture:

$$k(z) = V_c k_c + (1 - V_c) k_m \tag{3}$$

Where k_c and k_m are thermal conductivities of the ceramic and metal. If the top ceramic surface is held at a higher temperature T_c and bottom metal surface is held at a lower temperature T_m, the temperature variation of the plate depends only on its thickness coordinate and it satisfies the steady state heat conduction equation and boundary conditions:

$$-\frac{d}{dz}\left(k(z)\frac{dT}{dz}\right) = 0 \tag{4}$$

$$T|_{z=0} = T_m \tag{5}$$

$$T|_{z=t} = T_c \tag{6}$$

The solution of Eq. is given by the following expansion form:

$$T(z) = T_m + (T_c - T_m)\left(\frac{z}{t}\right) \times \frac{\sum_{i=0}^{\infty}\left(-\left(\frac{z}{t}\right)^n \left((k_c - k_m)/k_m\right)\right)^i / (ni+1)}{\sum_{i=0}^{\infty}\left(-\left((k_c - k_m)/k_m\right)\right)^i / (ni+1)} \tag{7}$$

Figure 2 is an exemplary plot of temperature distribution through the thickness for T_m = 30 and T_c = 300 ℃, k_c = 2.09 and k_m = 204 W/(m•K). It is obvious that the temperature in a FGM plate is significantly lower than that of a pure ceramic or metal plate. Thus can prove one of the advantages of FGM is optimizing temperature field.

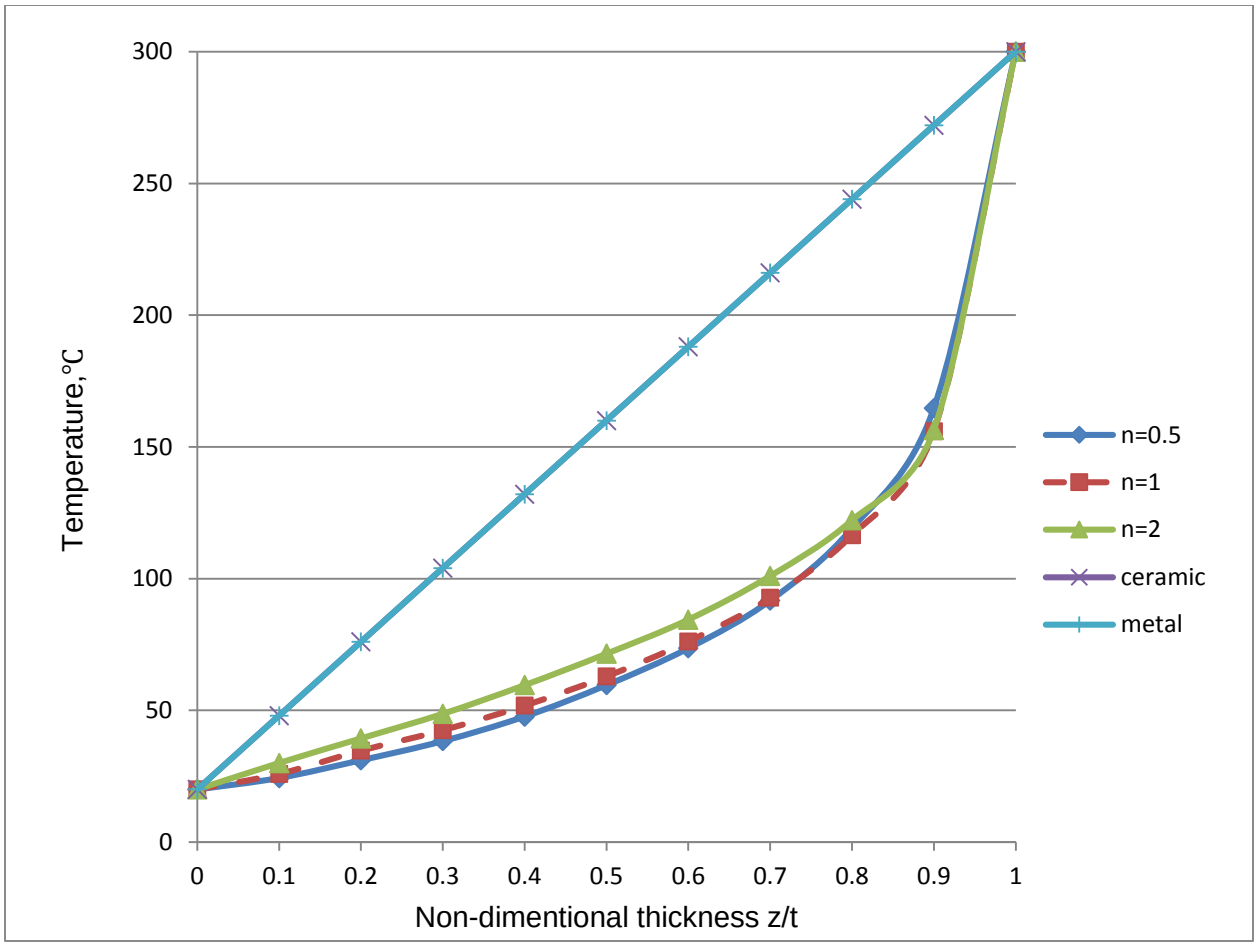

Figure 2. Temperature distribution through the plate thickness

The Reissner-Mindlin model which is based on first-order shear deformation theory gives the displacement field:

$$u = u_0 + z\theta_x \tag{8}$$

$$v = v_0 + z\theta_y \tag{9}$$

$$w = w \tag{10}$$

Where u_0 , v_0 and w are displacements of the middle plane of the plate in x, y and z direction, θ_x ,θ_y are rotations in yz and xz plane respectively. The linear strain can be expressed as the following equations:

$$\begin{Bmatrix} \varepsilon_x \\ \varepsilon_y \\ \gamma_{xy} \end{Bmatrix} = \begin{Bmatrix} u_{0,x} \\ v_{0,y} \\ u_{0,y+}v_{0,x} \end{Bmatrix} + z\begin{Bmatrix} \theta_{x,x} \\ \theta_{y,y} \\ \theta_{x,y} + \theta_{y,x} \end{Bmatrix} = \boldsymbol{\varepsilon_0} + z\boldsymbol{\kappa} \tag{11}$$

$$\begin{Bmatrix} w_{,x} + \theta_x \\ w_{,y} + \theta_y \end{Bmatrix} = \boldsymbol{\gamma} \tag{12}$$

Assuming z is the material gradient direction, coefficient of thermal expansion $\alpha(z)$ is a function of z coordinate. The thermal strain of the plate is given by:

$$\boldsymbol{\varepsilon^{th}} = \alpha(z) + \Delta T(z)[110]^T \tag{13}$$

According to Hook's law, the in-plane normal and shear stresses are given by:

$$\boldsymbol{\sigma} = \boldsymbol{E}(\boldsymbol{\varepsilon_0} + z\boldsymbol{\kappa} - \boldsymbol{\varepsilon^{th}}) \tag{14}$$

$$\boldsymbol{\tau} = \boldsymbol{G\gamma} \tag{15}$$

Where the Young's modulus E and shear modulus G are given by:

$$\boldsymbol{E} = \frac{E(z)}{1-\nu(z)^2}\begin{bmatrix} 1 & \nu(z) & 0 \\ \nu(z) & 1 & 0 \\ 0 & 0 & \dfrac{1-\nu(z)}{2} \end{bmatrix} \tag{16}$$

$$\boldsymbol{G} = \frac{\mu E(z)}{2(1+\nu(z))}\begin{bmatrix} 1 & 0 \\ 0 & 1 \end{bmatrix} \tag{17}$$

μ is the shear correction factor and $\nu(z)$ is Poisson's ratio as a function of z coordinate. With FGM's complex material properties, such thermoelastic problems are usually analyzed numerically.

2.2 VOLUME FRACTIONS OF TWO-DIMENSIONAL FUNCTIONALLY GRADED MATERIALS

For a 3D square plate with length *l* and thickness *t* as shown in Figure 3, simply supported boundary condition is:

For x= 0 and x=l:

$$U_y = 0, \quad \frac{\partial U_y^2}{\partial x^2} = 0 \tag{18}$$

For y= 0 and y=l:

$$U_y = 0, \quad \frac{\partial U_y^2}{\partial y^2} = 0 \tag{19}$$

Where U_z is the z direction displacement. For a 3D plate,

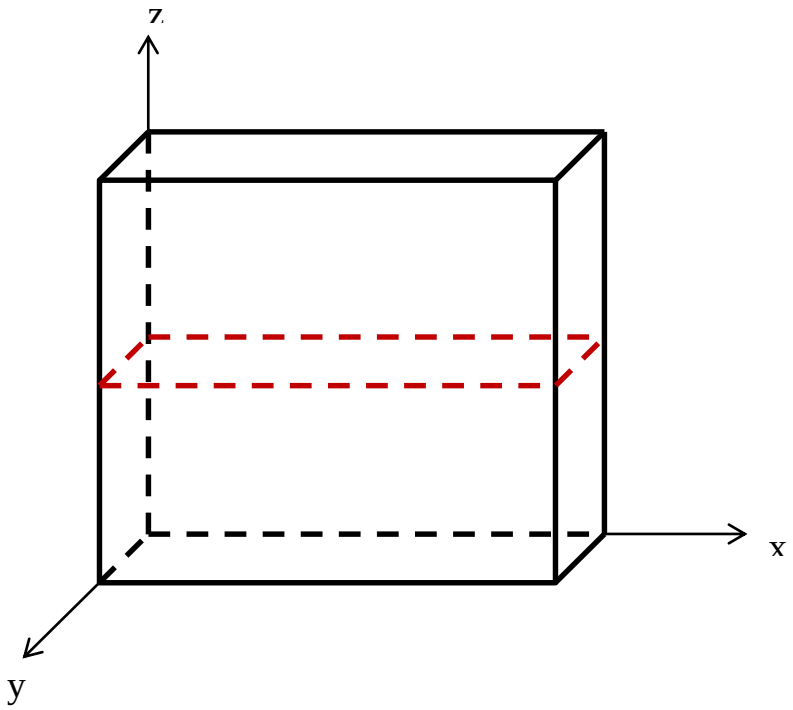

Figure 3. 3D geometry of a FGM plate

Assuming the FGM plate is graded in x and y directions. That is, the compositions of the FGM plate vary in both x and y directions, the volume fractions of each constituent V_i are given by the following power law. Subscripts 1, 2 and 3 denote ZrO_2, Al_2O_3 and Ti-6Al-4V respectively.

$$V_1 = \left(\frac{x}{l}\right)^m \left(\frac{y}{t}\right)^n \tag{20}$$

$$V_2 = [1-\left(\frac{x}{l}\right)^m]\left(\frac{y}{t}\right)^n \tag{21}$$

$$V_3 = 1-\left(\frac{y}{t}\right)^n \tag{22}$$

$$V_1 + V_2 + V_3 = 1 \tag{23}$$

From the above formulas, the volume fractions of the three basic constituent materials on each boundary surface are:

V_1=0, V_2=0, V_3=1 at x=0, y=0;

V_1=0, V_2=0, V_3=1 at x=l, y=0;

V_1=1, V_2=0, V_3=0 at x=l, y=t;

V_1=0, V_2=1, V_3=1 at x=0, y=t;

Volume fraction of Ti-6Al-4V increases with n. With a fixed n value, when m increases, volume fraction of Al_2O_3 increases and volume fraction of ZrO_2 decreases. The coordinate system and volume fraction distribution for the FGM plate is shown in Figure 4. For example, let m=n=0.3, then the material is ZrO2 rich. The volume fractions of each material are shown in Figure 5-Figure 7.

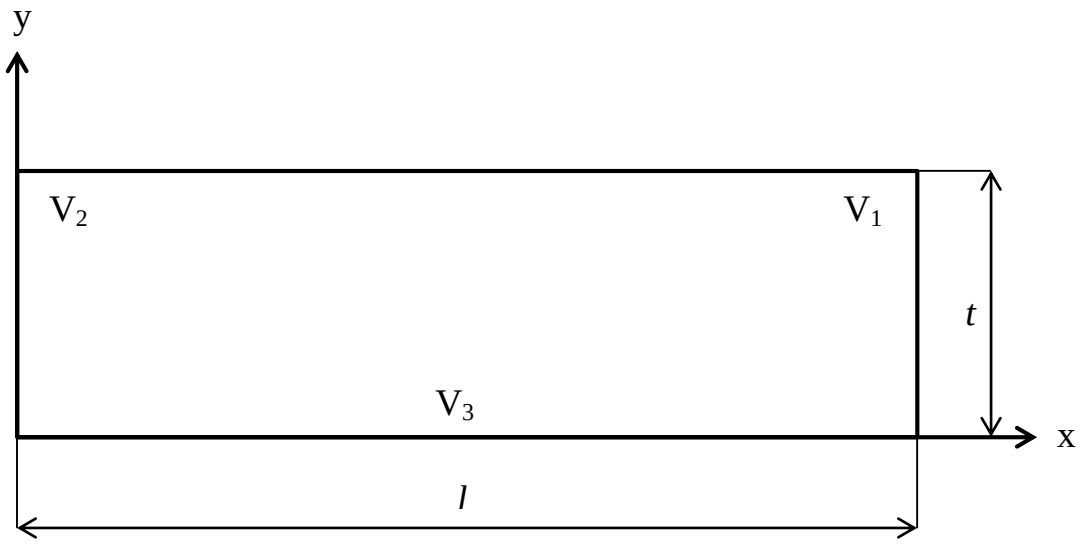

Figure 4. Plate cross section and volume fraction distribution for FGM plate

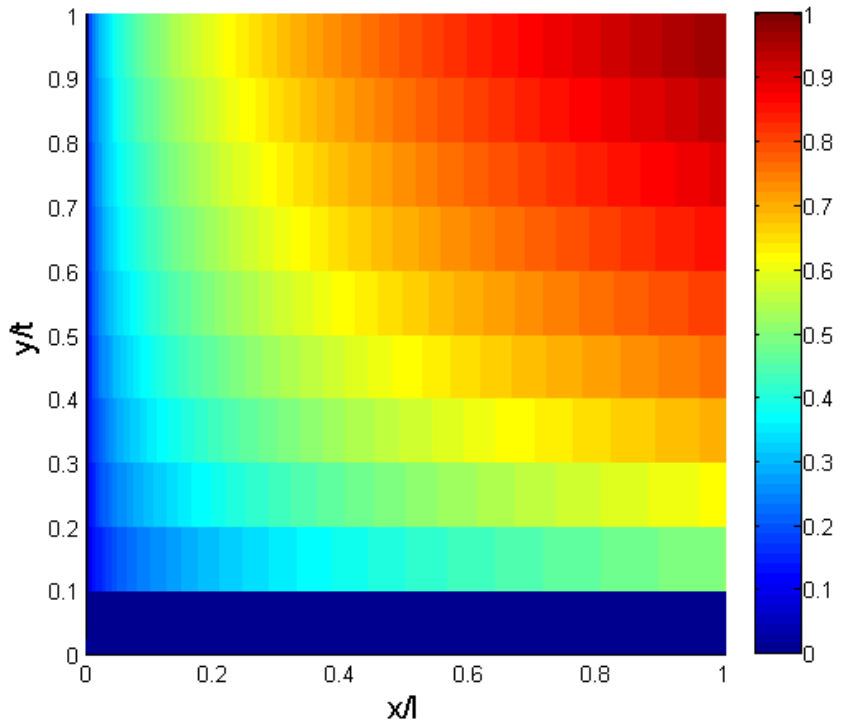

Figure 5. Volume fraction of ZrO_2

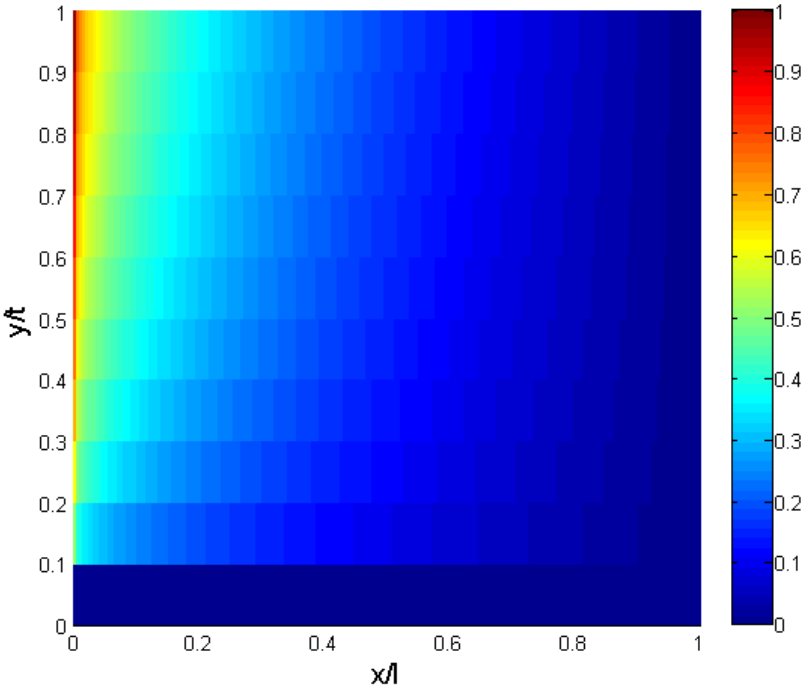

Figure 6. Volume fraction of Al_2O_3

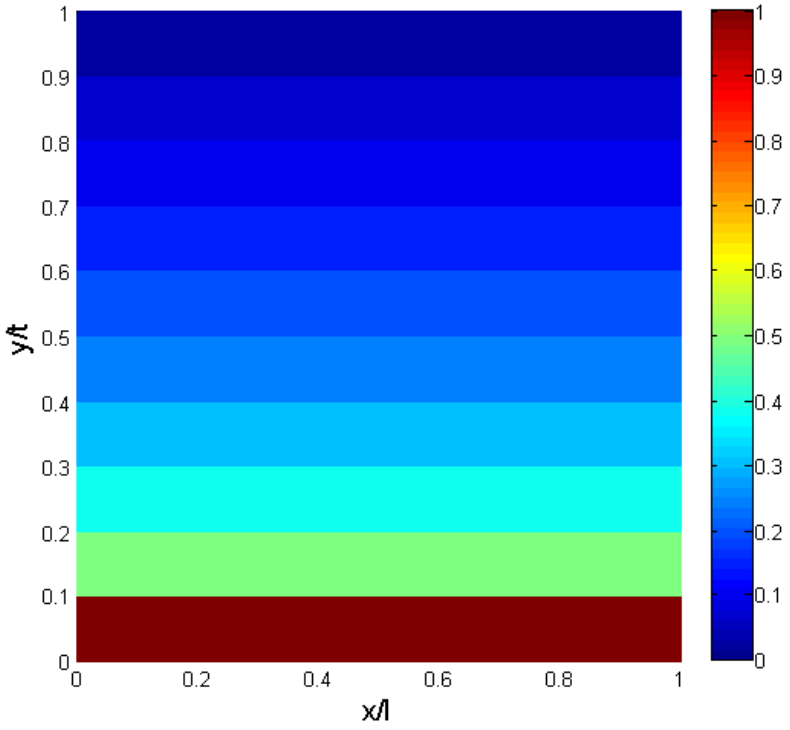

Figure 7. Volume fraction of Ti-6Al-4V

2.3 TEMPERATURE DEPENDENT MATERIAL PROPERTIES

The constituents of the FGM plate are assumed to be ZrO_2 as material 1, Al_2O_3 as material 2 and Ti-6Al-4V as material 3. ZrO_2 and Al_2O_3 ceramics have low thermal conductivities, which give them high thermal resistance. Titanium alloy Ti-6Al-4V is a light material with high strength. Their temperature-dependent material properties are descried as functions of temperature (Cubberly, 1989) (Munro, 1997) (S.K. Chan, 1991) (Touloukian, 1973). The elastic modulus E, Poisson's ratio ν, thermal conductivity k, specific heat C, coefficient of thermal expansion (CTE) α, density ρ, yield stressσ_y and ultimate stress σ_u for metal, tensile and compressive strength σ_{ut} and σ_{uc} for ceramics are given as follows:

ZrO_2:

$$
\begin{cases}
\mathrm{E} = 274.1 - 2.7 \times 10^{-2} T & \text{[GPa]} \\
\nu = 0.3 + 3.2 \times 10^{-5} T & \\
\mathrm{k} = 2.072 - 3.656 \times 10^{-4} T + 4.347 \times 10^{-7} T^2 & \text{[W/(m•K)]} \\
\mathrm{C} = 274 + 7.95 \times 10^{-1} T - 6.19 \times 10^{-4} T^2 + 1.71 \times 10^{-7} T^3 & \text{[J/(kg•K)]} \\
\alpha = 7.091 \times 10^{-6} - 2.532 \times 10^{-9} T + 2.262 \times 10^{-12} T^2 & \text{[1/K]} \\
\rho = 5600/\{1 + \alpha(\mathrm{T} - 300)\}^3 & \text{[kg/m}^3\text{]} \\
\sigma_{UT} = 148.1 + 1.184 \times 10^{-3} T - 31.4 \times 10^{-6} T^2 & \text{[MPa]} \\
\sigma_{UC} = 2373 - 0.9854 T & \text{[MPa]}
\end{cases}
\tag{24}
$$

Al_2O_3:

$$\mathrm{E} = 417 - 0.0525(\mathrm{T} + 273) \quad [\mathrm{GPa}]$$

$$\nu = \frac{417-0.0525(\mathrm{T}+273)}{2\times(169-0.0229(T+273))} - 1$$

$$\mathrm{k} = 5.85 + \frac{15360\exp(-0.002(\mathrm{T}+273))}{\mathrm{T}+789} \quad [\mathrm{W/(m{\bullet}K)}]$$

$$\mathrm{C} = 1117 + 0.14(\mathrm{T} + 273) - 411\exp(-0.006(\mathrm{T} + 273)) \quad [\mathrm{J/(kg{\bullet}K)}]$$

$$\alpha = 7.419 \times 10^{-6} + 6.43 \times 10^{-10}(\mathrm{T} + 273) - 3.211 \times 10^{-6}\exp((-2.59 \times 10^{-3})(\mathrm{T} + 273)) \quad [1/\mathrm{K}]$$

$$\rho = 3985.3 - 7.158 \times 10^{-2}(T + 273) - 3.035 \times 10^{-5}(T + 273)^2 + 7.232 \times 10^{-9}(T + 273)^3 \quad [\mathrm{kg/m^3}]$$

$$\sigma_{UT} = 259.3 - 1.379 \times 10^{-2}T^2 \quad \mathrm{T} \leqslant 1300\mathrm{K} \quad [\mathrm{MPa}]$$

$$\sigma_{UT} = -2062 + 3.79T - 1.546 \times 10^{-3}T^2 \quad 1300\mathrm{K} \leqslant \mathrm{T} \leqslant 1600\mathrm{K} \quad [\mathrm{MPa}]$$

$$\sigma_{UT} = 181 - 8.55 \times 10^{-2}T^2 \quad \mathrm{T} > 1600\mathrm{K} \quad [\mathrm{MPa}]$$

$$\sigma_{UC} = 4763\exp(-1.529 \times 10^{-3}T) \quad [\mathrm{MPa}]$$

(25)

Ti-6Al-4V:

$$
\begin{cases}
\mathrm{E} = 122.7 - 0.0565\mathrm{T} & & [\mathrm{GPa}] \\
\nu = 0.289 + 3.2 \times 10^{-5} T & & \\
\mathrm{k} = 1.1 + 0.017\mathrm{T} & & [\mathrm{W/(m{\bullet}K)}] \\
\mathrm{C} = 350 + 8.78 \times 10^{-1} T - 9.74 \times 10^{-4} T^2 + 4.43 \times 10^{-7} T^3 & & [\mathrm{J/(kg{\bullet}K)}] \\
\alpha = 7.43 \times 10^{-6} + 5.56 \times 10^{-9} T - 2.69 \times 10^{-12} T^2 & 300\mathrm{K} \leqslant \mathrm{T} \leqslant 1100\mathrm{K} & [1/\mathrm{K}] \\
\alpha = 10.291 \times 10^{-6} & 1100\mathrm{K} \leqslant \mathrm{T} & [1/\mathrm{K}] \\
\rho = 4420/\{1 + \alpha(\mathrm{T} - 300)\}^3 & & [\mathrm{kg/m^3}] \\
\sigma_Y = 1252 - 0.8486T & \mathrm{T} \leqslant 1400\mathrm{K} & [\mathrm{MPa}] \\
\sigma_Y = 316 - 0.18T & \mathrm{T} > 1400\mathrm{K} & [\mathrm{MPa}]
\end{cases}
\tag{26}
$$

These material properties as functions of temperature are plotted in Figure 8-Figure 14. It can be seen that elastic modulus and density decrease slightly with the increase of temperature, Poisson's ratio, specific heat and coefficient of thermal expansion generally increase as temperature elevates. Material strength, especially compressive strength of ceramics ZrO_2 and Al_2O_3, drops as high as 80% at higher temperatures. If temperature effect is not considered in a design, failure will not be predicted in time and this could compromise the entire design. Thus it is very important to include temperature-dependent material properties in high temperature thermoelastic studies to ensure the accuracy of results.

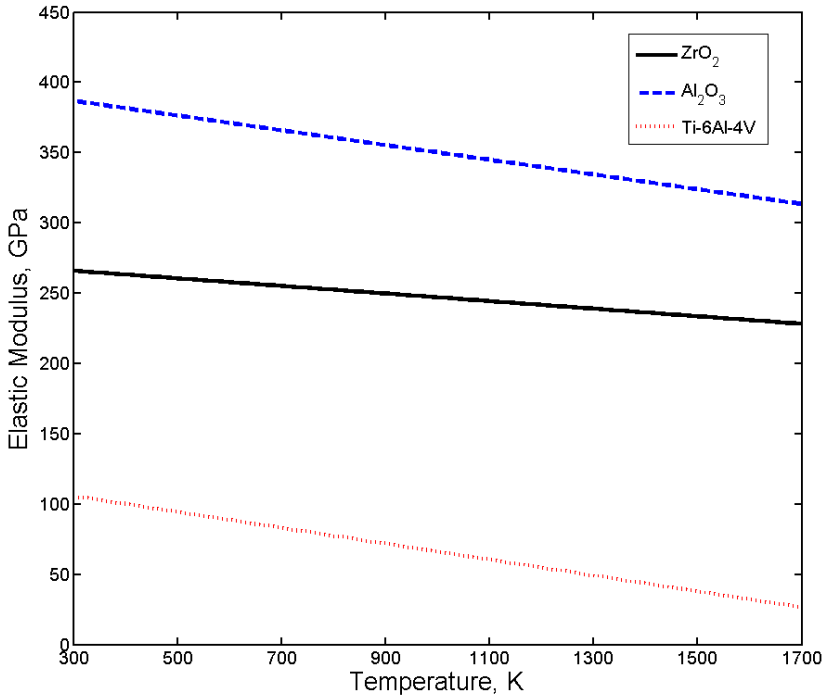

Figure 8. Elastic modulus as a function of temperature

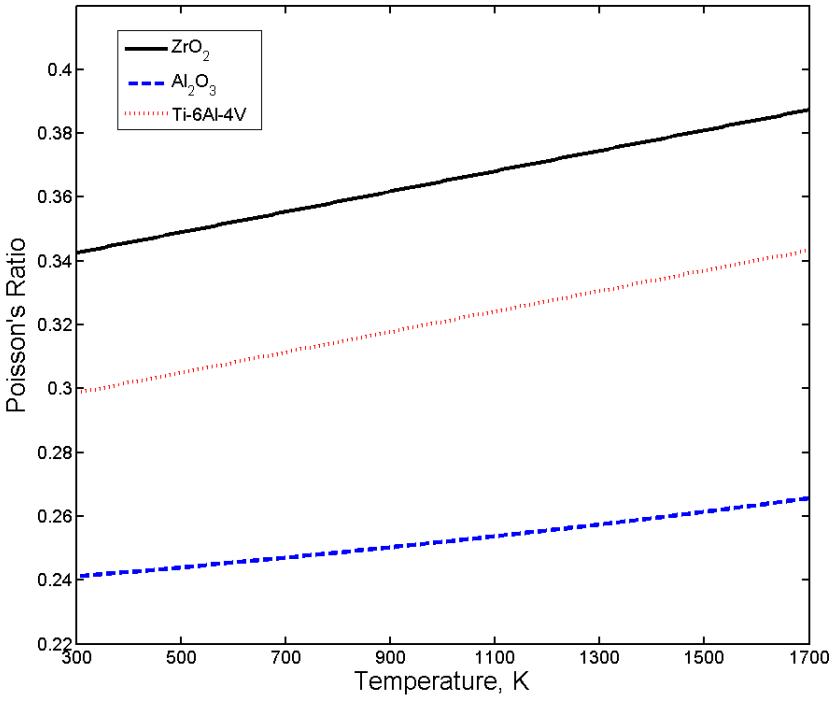

Figure 9. Poisson's ratio as a function of temperature

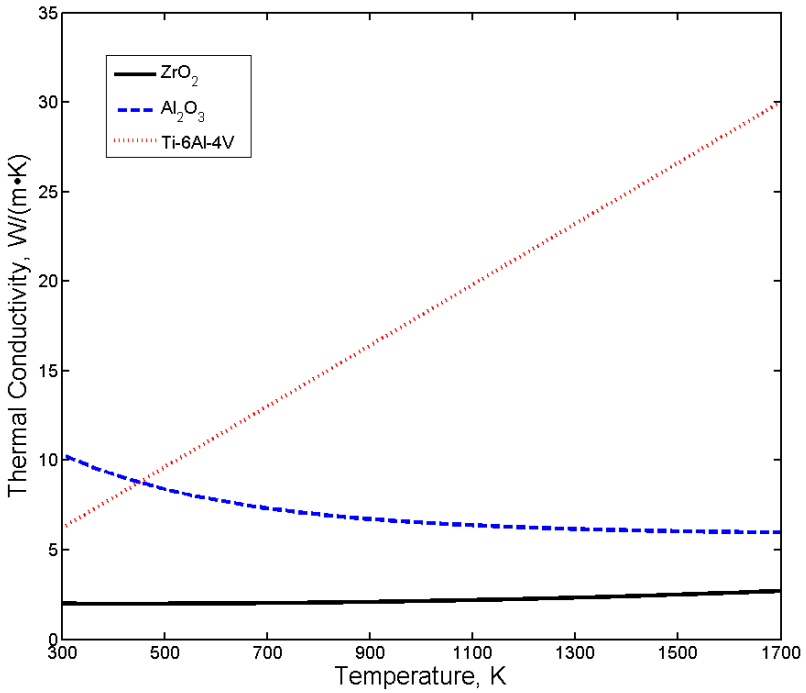

Figure 10. Thermal conductivity as a function of temperature

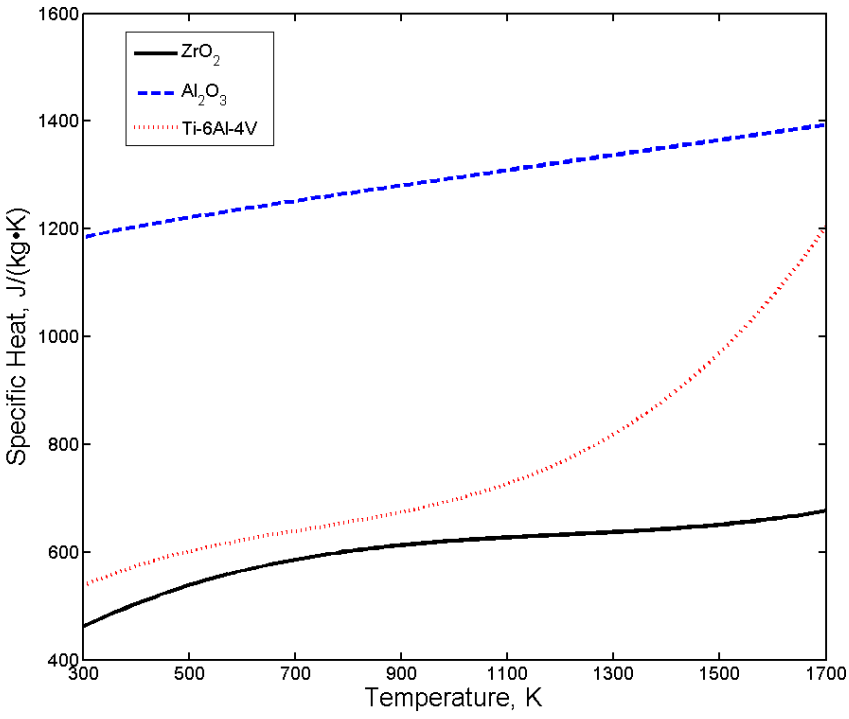

Figure 11. Specific heat as a function of temperature

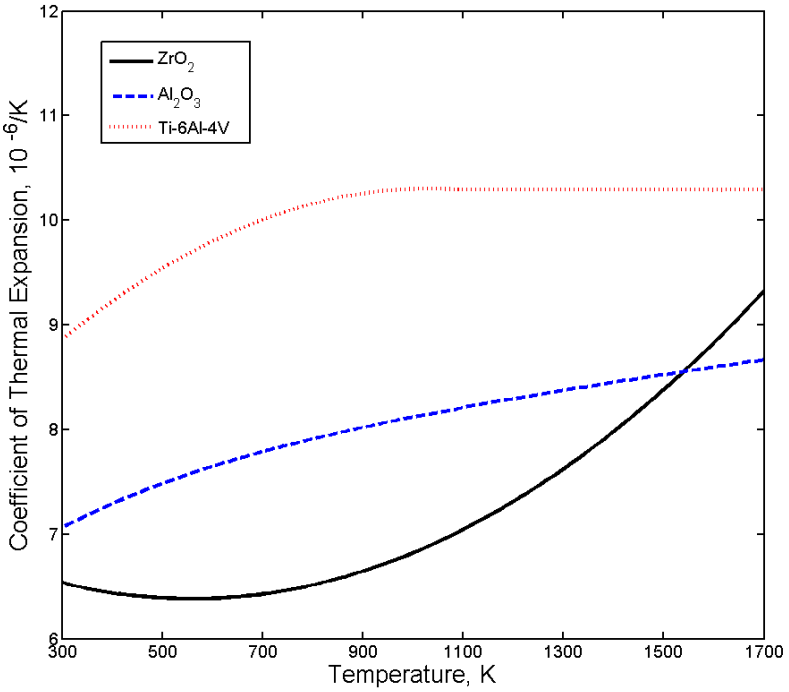

Figure 12. Coefficient of thermal expansion as a function of temperature

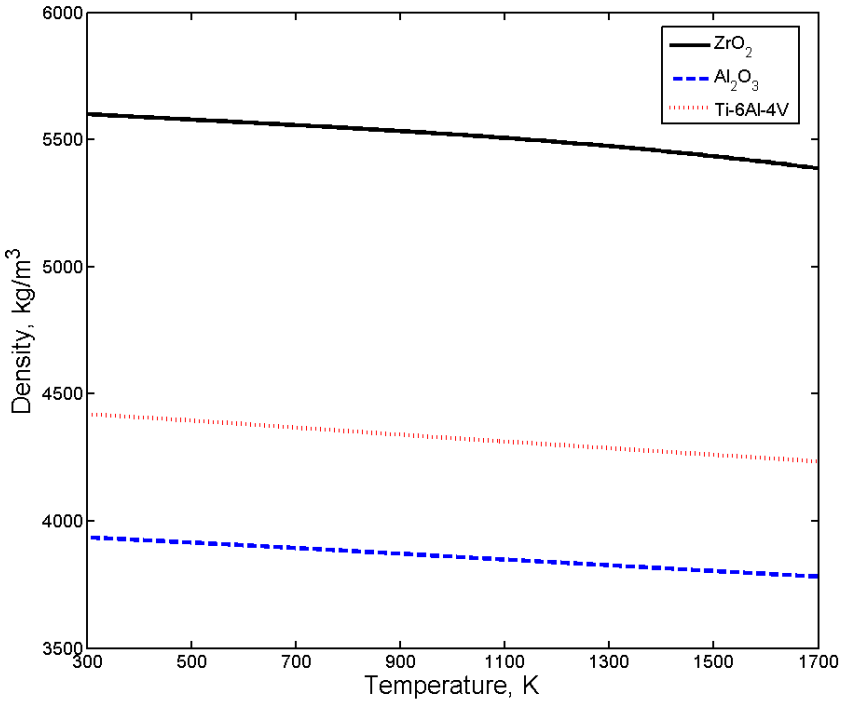

Figure 13. Density as a function of temperature

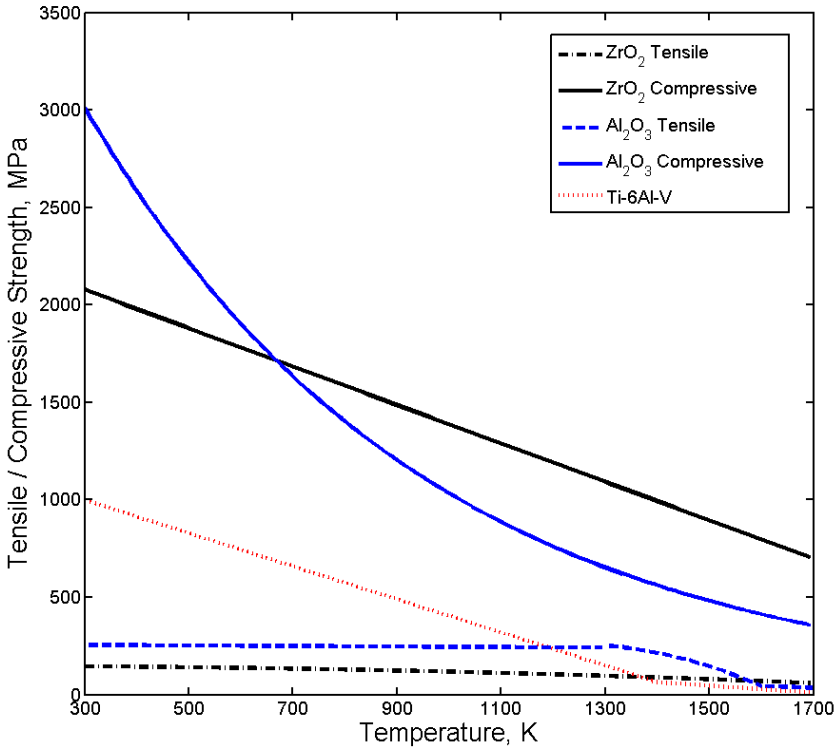

Figure 14. Yield stress, tensile and compressive strength as a function of temperature

2.4 ESTIMATION OF MATERIAL PROPERTIES

Realistic characterizations of the thermomechanical behaviors of FGMs require appropriate predictions of thermophysical property data. Since a tailored spatial variation in microstructure is intentionally introduced in a FGM, a variety of different microstructures can exist within a graded region. Thermophysical properties, which are dependent both on individual phase properties and on microstructural details, such as volume fraction, size, shape, orientation and spatial distribution of the phases and phase connectivity, similarly can vary strongly with position. Because of the vast number of measurements required, experimental data are limited,

often including information only for the individual phases. Clearly, the ability to provide reasonable estimates of material properties based on complex microstructure is a challenging but important part of the modeling process.

2.4.1 Simple rule of mixtures

The most common approach for estimating the material properties of FGMs is to apply rule of mixtures. The simplest is the classical linear rule of mixtures (R.O.M.) (Voight estimate) for two constituent materials (Voight, 1889):

$$P = V_1 P_1 + V_2 P_2 \tag{27}$$

Where P is a typical property. The Voight estimate is simply a volume based arithmetic mean. It assumes no interactions between phases. Because of its simplicity, it is often used for FGMs, since a single relationship can be used for all volume fractions and microstructures. However, also because of its simplicity, their validity is limited.

2.4.2 Hashin and Shtrikman bounds

Hashin and Shtrikman (HS) proposed an approach that utilizes variational principles of thermomechanics to predict upper and lower bounds on material properties (Shtrikman, 1963). Bulk modulus K and shear modulus G can be obtained by applying variatinal methods to linear elasticity theory:

$$K_L = K_1 + \frac{V_2}{\frac{1}{K_2 - K_1} + \frac{3V_1}{3K_1 + 4G_1}} \tag{28}$$

$$K_U = K_2 + \frac{V_1}{\frac{1}{K_1 - K_2} + \frac{3V_2}{3K_2 + 4G_2}} \tag{29}$$

$$G_L = G_1 + \frac{V_2}{\frac{1}{G_2 - G_1} + \frac{6(K_1 + 2G_1)V_1}{5G_1(3K_1 + 4G_1)}} \tag{30}$$

$$G_U = G_2 + \frac{V_1}{\frac{1}{G_1 - G_2} + \frac{6(K_2 + 2G_2)V_1}{5G_2(3K_2 + 4G_2)}} \tag{31}$$

The subscripts U and L denote upper and lower bound respectively.

A similar approach was applied to electromagnetic theory to calculate magnetic permeability (Shtrikman, 1962). The upper and lower bounds on thermal conductivity k can also be obtained by direct analogy to magnetic permeability:

$$k_L = k_1 + \frac{V_2}{\frac{1}{k_2 - k_1} + \frac{V_1}{3K_1}} \tag{32}$$

$$k_U = k_2 + \frac{V_1}{\frac{1}{k_1 - k_2} + \frac{V_2}{3K_2}} \tag{33}$$

It can be observed that the upper and lower bounds are produced just by switching the two materials. The true value of the material property should fall between the HS bounds.

2.4.3 Wakashima-Tsukamoto model:

A more recent effort is the Wakashima-Tsukamoto (WT) model (Kenji Wakashima, 1991). It employed a “mean-field” approach characterized by a random dispersion of misfitting ellipsoidal inhomogeneities, including an interaction effect to account for the typically large number of

ellipsoids that interact. The interaction is accounted for as an approximation using the "average stress in matrix" concept. Relations were derived for the effective bulk K and shear moduli G, coefficient of thermal expansion α, specific heat C and thermal conductivity k.

$$K = K_1 + \frac{aV_s K_1 \left(K_s - K_1\right)}{V_1 K_s + aV_s K_1} \tag{34}$$

$$G = G_1 + \frac{bV_s G_1 \left(G_s - G_1\right)}{V_1 G_s + bV_s G_1} \tag{35}$$

$$a = \frac{K_s \left(3K_1 + 4G_1\right)}{K_1 \left(3K_s + 4G_1\right)} \tag{36}$$

$$b = \frac{G_s \left(1 + \dfrac{9K_1 + 8G_1}{6K_1 + 12G_1}\right)}{G_s + G_1 \left(\dfrac{9K_1 + 8G_1}{6K_1 + 12G_1}\right)} \tag{37}$$

$$\alpha = \alpha_1 + \frac{\left(\dfrac{1}{K} - \dfrac{1}{K_1}\right)\left(\alpha_s - \alpha_1\right)}{\dfrac{1}{K_s} - \dfrac{1}{K_1}} \tag{38}$$

$$C = C_1 V_1 + C_s V_s \tag{39}$$

$$k = k_1 + \frac{k_1 V_s \left(k_s - k_1\right)}{k_1 + \dfrac{1}{3} V_1 \left(k_s - k_1\right)} \tag{40}$$

In the WT model, the subscript 1 denotes the matrix. The assumption of which material is matrix and which one is the inclusion produces two distinct results that are similar to the HS bounds.

2.4.4 Modified Wakashima-Tsukamoto model

For a FGM, the volume fraction of each constituent is constantly changing as the FGM is graded from one material to another. This kind of deliberate variation can produce separate regions where a certain material may act as either matrix or inclusions, even something intermediate. If the assumption of matrix and inclusions is reversed, the WT model predicts a slightly different result. The existing WT model may adequately describe one region while reversing the assumptions, it may represent another region, but the connecting region is left not well-defined. However, the true values of material properties of all regions should fall between the bounds predicted by the two assumptions. The question is how to accurately estimate them. It is suggested by (T. Hirano, 1990) to use some weighted average of the bounds to provide a smooth transition between the bonding curves. In this study, the approach we propose is to take a volume based average of the two bounds.

For example, for a FGM that consists of two materials whose bulk moduli are K_1=222Gpa, K_2=96Gpa. Assume volume fraction of material 1 depends linearly on its coordinate in the thickness direction z.

$$V_1 = 1 - y/t \tag{41}$$

$$V_2 = y/t \tag{42}$$

If we assume material 1 is the matrix and material 2 is the reinforcement, according to the WT model, the bulk modulus can be predicted by Equation (34):

$$K_{WT1} = K_1 + \frac{a_1 V_2 K_1 (K_2 - K_1)}{V_1 K_2 + a_1 V_2 K_1} \tag{43}$$

If we reverse the assumption and material 2 is the matrix, then

$$K_{WT2} = K_2 + \frac{a_2 V_1 K_2 \left(K_1 - K_2\right)}{V_2 K_1 + a_2 V_1 K_2} \tag{44}$$

It's worth pointing out that in this case, the two bounding results predicted by the WT model under different assumptions coincide with HS upper and lower bounds. At intermediate volume fractions, the effective bulk modulus can be estimated by taking a volume based average of the two bounds:

$$K = K_{WT1} V_1 + K_{WT2} V_2 \tag{45}$$

The comparison is shown in Figure 15:

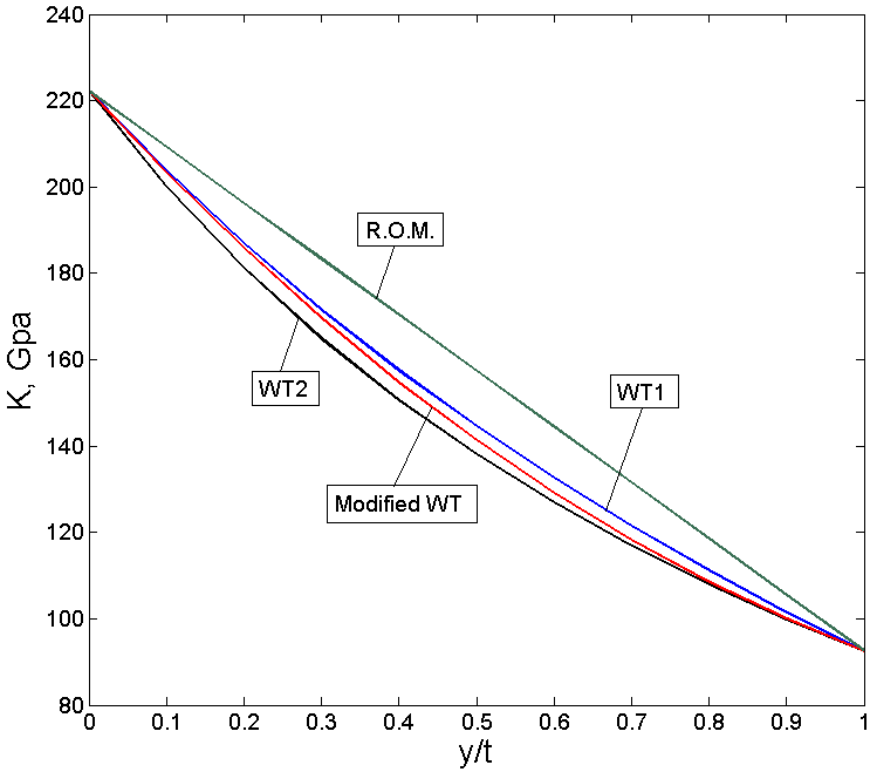

Figure 15. Comparison of bulk modulus for different material models

It can be seen that this averaging approach we proposed gives a smooth transition between the two bounds and provides a legitimate estimation. Also we can see that simple R.O.M. tends to overestimate material properties.

The WT model is given for two constituents binary systems. In order to use it in our multi-dimensional FGM model, it must be expended for three constituents. By assuming V_s is a mixture of V_2 and V_3, we can use the laws above to obtain overall material properties.

$$V_s = V_2 + V_3 \tag{46}$$

If we assume material 1 is the matrix, material 2 and 3 are both reinforcement particles. We can assume there is a new kind of mixture inclusions that accounts for material 2 and 3. Because they are both inclusions that interact with the same matrix, volume based average of the two materials might well represent the material properties of their mixture.

The bulk modulus of the mixture is estimated as:

$$K_s = K_2 V_2 + K_3 V_3 \tag{47}$$

Then using the WT model, the bulk modulus of the FGM is obtained under the assumption that material 1 is the matrix:

$$K_{WT1} = K_1 + \frac{aV_s K_1 \left(K_s - K_1\right)}{V_1 K_s + aV_s K_1} \tag{48}$$

Similarly, we can obtain K_{WT2} and K_{WT3} by assuming material 2 or 3 is the matrix. Then using the modified WT model, we can obtain the overall bulk modulus:

$$K = K_{WT1} V_1 + K_{WT2} V_2 + K_{WT3} V_3 \tag{49}$$

Shear modulus G, thermal conductivity k and other formerly defined material properties can also be obtained similarly. Thus the modified WT model can be applied to three constituents FGMs.

Using the modified WT model to predict material properties, when m=n=1, Figure 16 - Figure 23 describe the variations of material properties through the FGM plate at 300K.

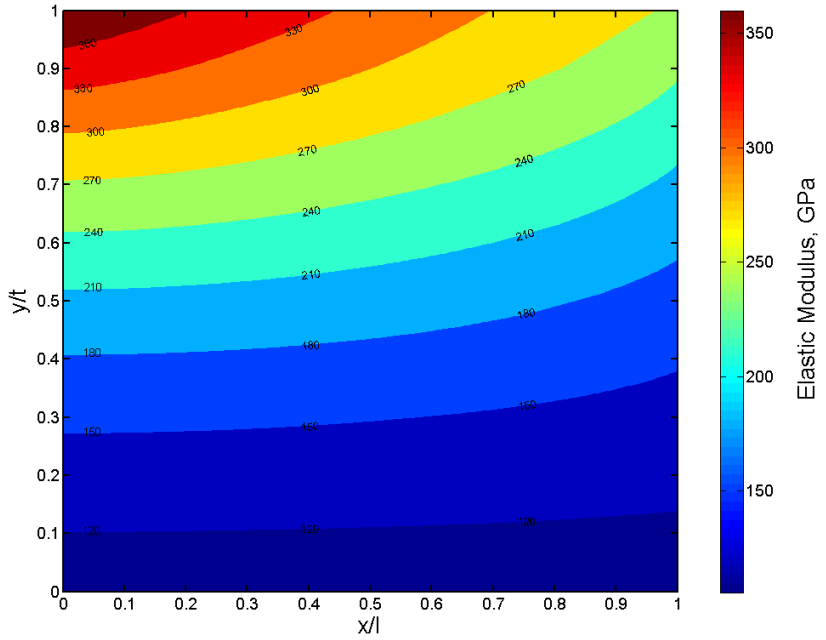

Figure 16. Variation of the elastic modulus through the plate, [GPa]

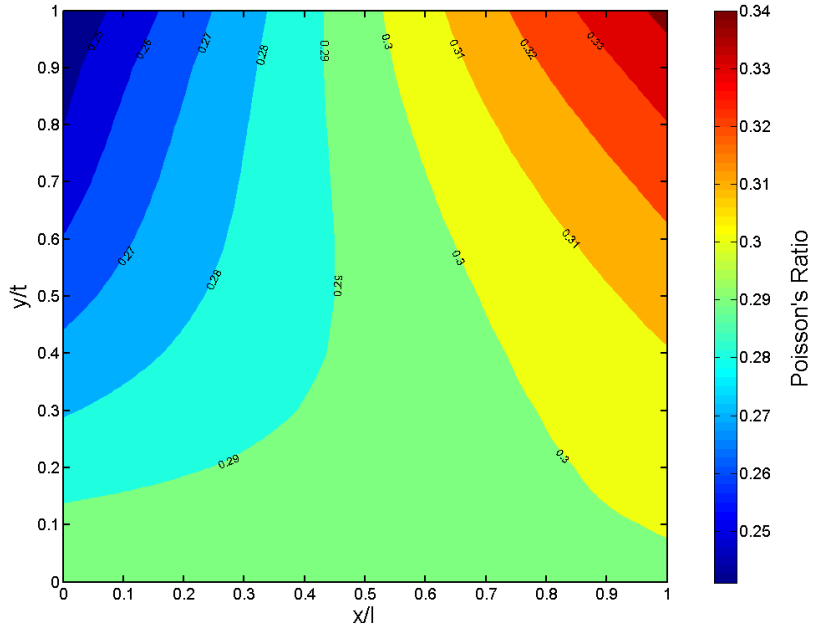

Figure 17. Variation of the Poison's ratio through the plate

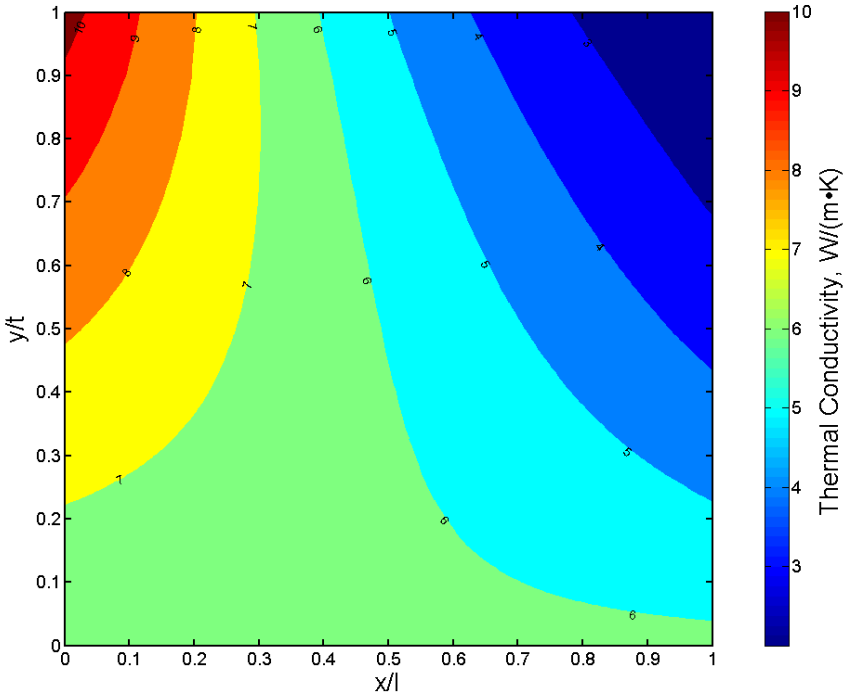

Figure 18. Variation of the thermal conductivity through the plate, [W/(m•K)]

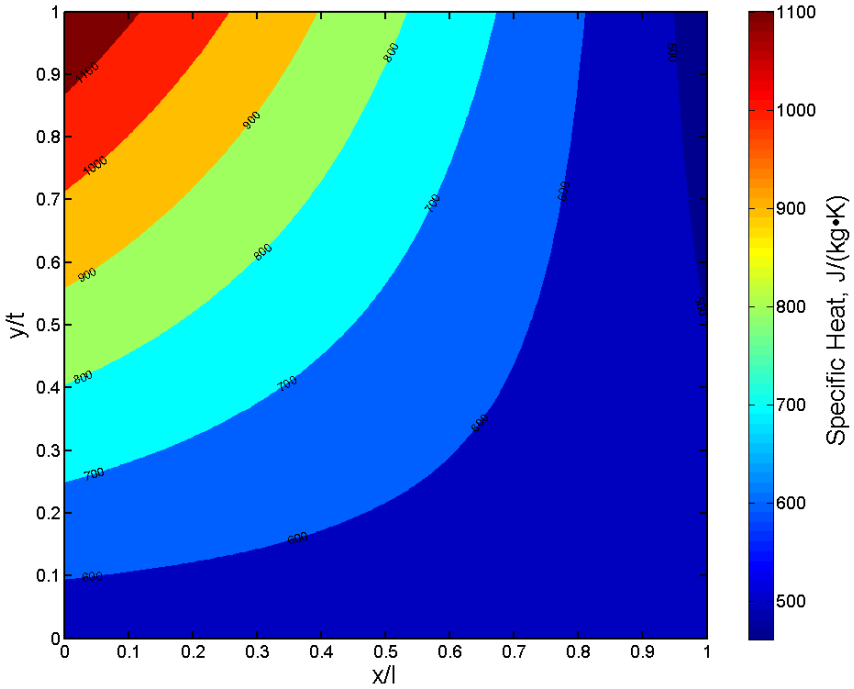

Figure 19. Variation of the specific heat through the plate, [J/(kg•K)]

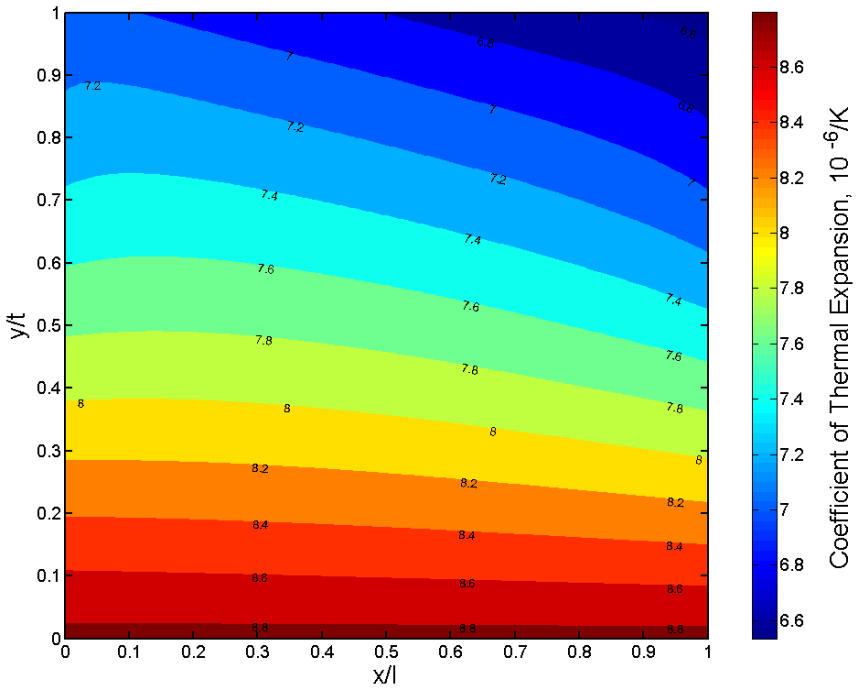

Figure 20. Variation of the coefficient of thermal expansion through the plate, [1/K]

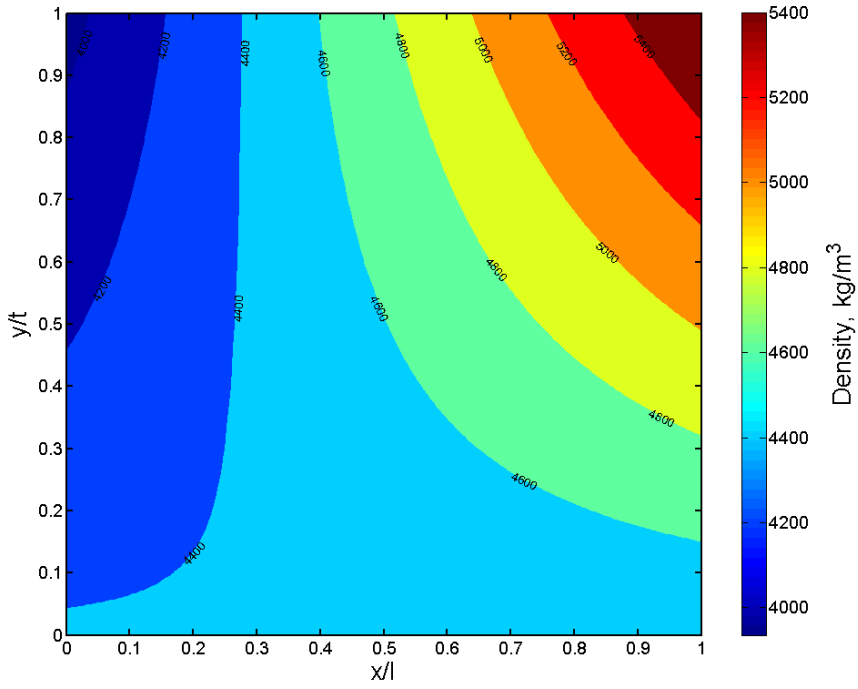

Figure 21. Variation of the density through the plate, [kg/m^3]

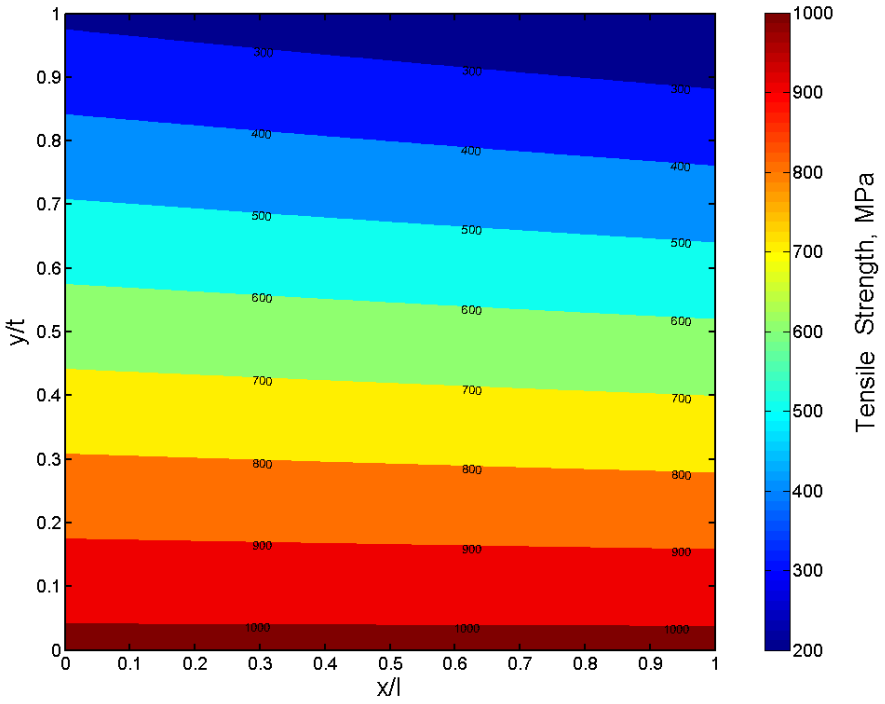

Figure 22. Variation of tensile strength through the plate, [MPa]

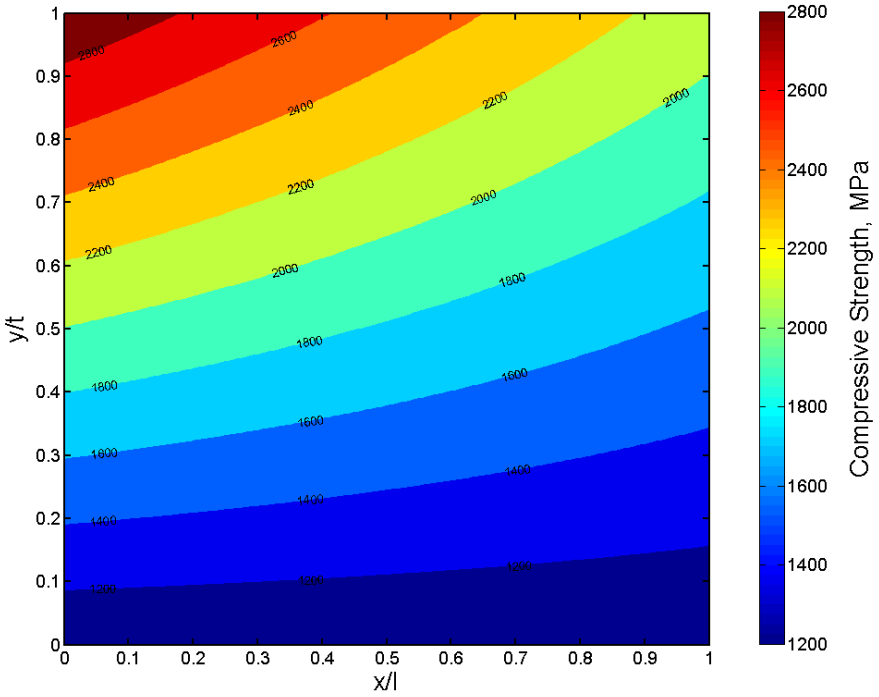

Figure 23. Variation of compressive strength through the plate, [MPa]

2.5 MODEL VERIFICATION

There are no existing literature data on 2D FGM using WT model with temperature dependent material properties to the author's knowledge. Therefore we verified the results using an 1D FGM model comprised of ZrO_2 and Al from (H. Nguyen-Xuana, 2012).

The volume fraction laws for this 1D FGM are the same with Equation(1) and (2). Material properties are shown in Table 1.

Table 1. Material properties for Al and ZrO_2

	E(GPa)	ν	k (W/(m•K))	α(/K)	ρ(kg/m^3)
Al	70	0.3	204	23×10^{-6}	2707
ZrO_2	151	0.3	2.09	10×10^{-6}	3000

FGM material properties are estimated using simple rule of mixtures as defined in Eq(3). The model geometry is a plate with length l and thickness t. Top ceramic surface temperature and bottom metal surface temperature are held at $T_m = 30$ ℃ and $T_c = 300$ ℃. In the literature, thermal stresses and plate center displacement are calculated using numerical technique. The tool we used is commercial explicit finite element package ANSYS Mechanical APDL 14.5, with user-defined material properties input program. Non-dimensional center displacement and non-dimensional axial stress are calculated using:

$$\overline{w_c} = 100 w_c t E_c / 12(1-\nu^2) p l^4 \tag{50}$$

$$\overline{\sigma_x} = \sigma_x t^2 / p l^2 \tag{51}$$

Our results agree very well with data from the literature, as can be seen in Figure 24 and Figure 25. Thus we can say that if the input material properties are correct, our program can adequately carry out thermoelastic analysis for FGMs. As shown in previous material property plots Figure 16 - Figure 23, we trust that we can correctly estimate 2D FGM properties, and thus obtain appropriate results.

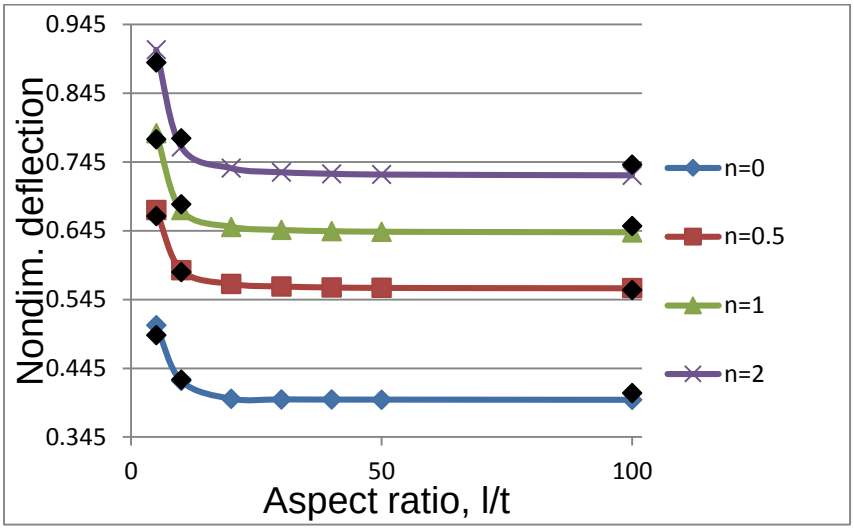

Figure 24. Non-dimensional center displacement V.S. plate aspect ratio

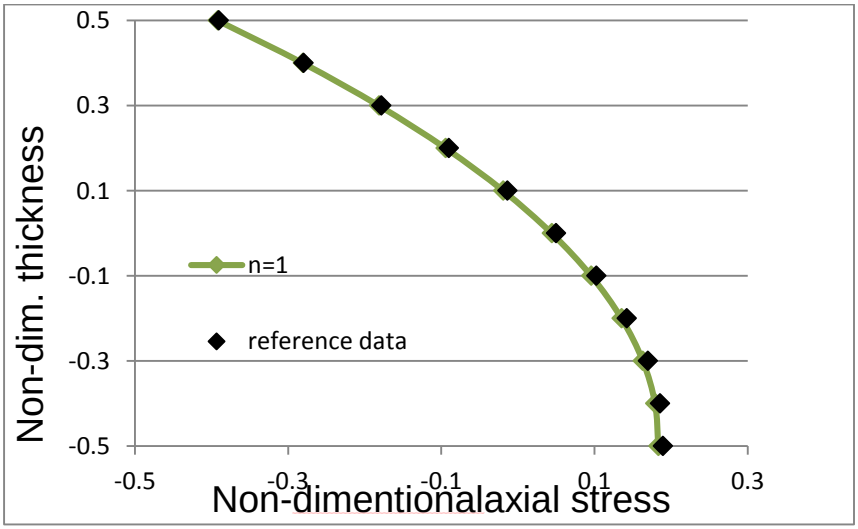

Figure 25. Non-dimensional stress at different thickness

3.0 RESULTS OF TRANSIENT THERMOELASTIC ANALYSIS

The thermoelastic finite element analysis of the FGM plate is carried out by commercial explicit finite element package ANSYS Mechanical APDL 14.5, with input program of user-defined material properties and complex post-processing failure criteria analysis. The plate dimension is given by l=300mm and t=15mm. It is modeled with 2D Eight-node quadratic thermal and structural solid element. Plane stress assumption is used. Boundary condition is applied as simply supported. At the heating stage, a heat flux of q=300kW/m^2 is applied on the top surface. The bottom surface is held at 300K. The plate reaches steady state at 300s. Then it is subjected to a sudden cooling convection to 300K with a film coefficient h=1000 W/m^2• K. Normalized principal stresses are introduced to analyzed failure criteria.

3.1 HEATING STAGE

3.1.1 Transient thermal analysis

Assume the plate has a uniform initial temperature of 300K. First, a heat flux of q=300kW/m^2 is applied to the top surface. The bottom surface is held at 300K. Other boundaries are adiabatic. Transient thermal analysis is conducted on the 2D FGM plate. The maximum temperature in the plate during the heating process is shown in Figure 26. It can be seen that immediately after heat

flux is applied, the plate's maximum temperature rises rapidly during the first 100 second. After then, the temperature increase slows down and finally the plate reaches steady state at 300 second. At steady state, the maximum temperature of the plate is 1080.42K.

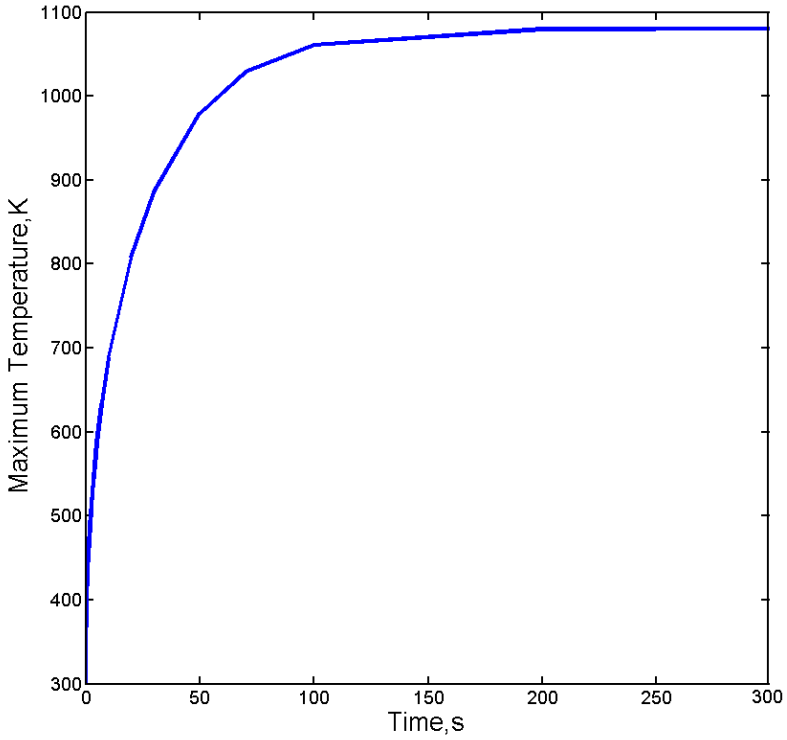

Figure 26. Maximum temperature during heating process

Figure 27 - Figure 32 shows temperature distributions of the plate at different times. It can be seen that when the heat flux is applied, temperature of the top surface begins to increase. At first, it's just the narrow top portion of the plate that is heated. Over time, by heat conduction, temperature elevation gradually travels towards the bottom of the plate. As the heat flux is applied to the top surface, temperature is always highest there, and decreases from top to bottom. It is worth pointing out that although the applied heat flux is uniform, the temperature profile is

not symmetric from left to right, because of FGM's heterogeneous nature. The left portion of the FGM plate is Al_2O_3 rich and the right is ZrO_2 rich. The maximum temperature always happens at the right corner because ZrO_2 has a lower thermal conductivity, which affects temperature distribution. During the transient process, heat is also transferred at different rate, because at different locations, material properties such as heat capacity and density are also different. The plate reaches steady state after 300s. The right corner has the maximum temperature of 1080.42K.

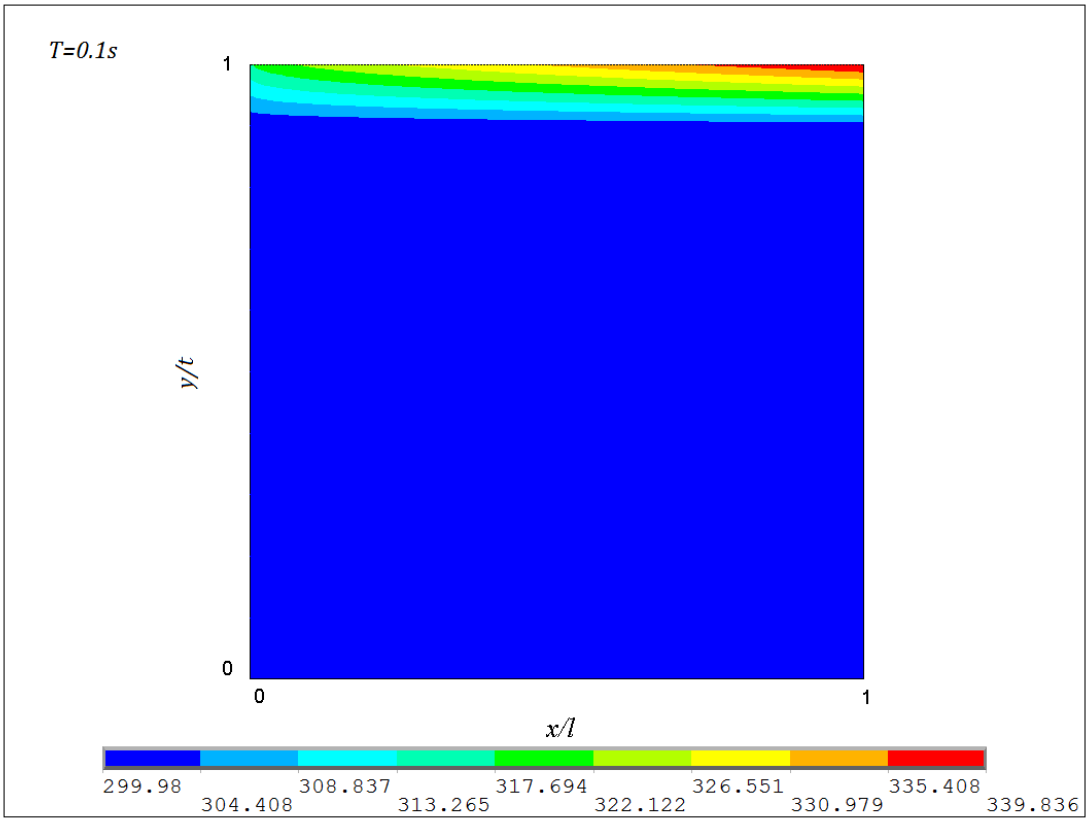

Figure 27. Plate temperature distribution at 0.1 second

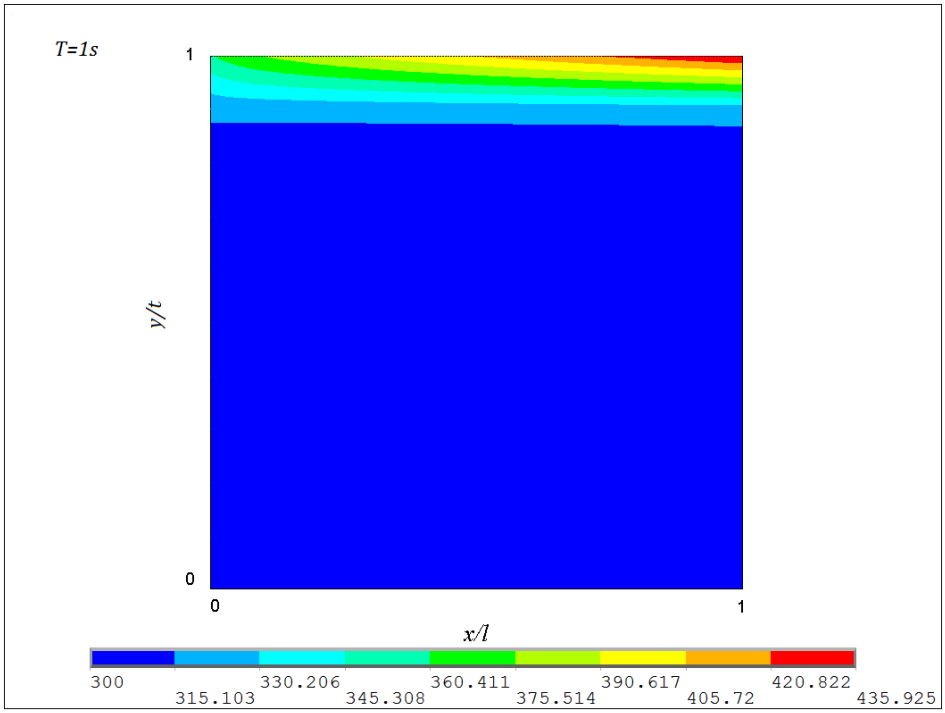

Figure 28. Plate temperature distribution at 1 second

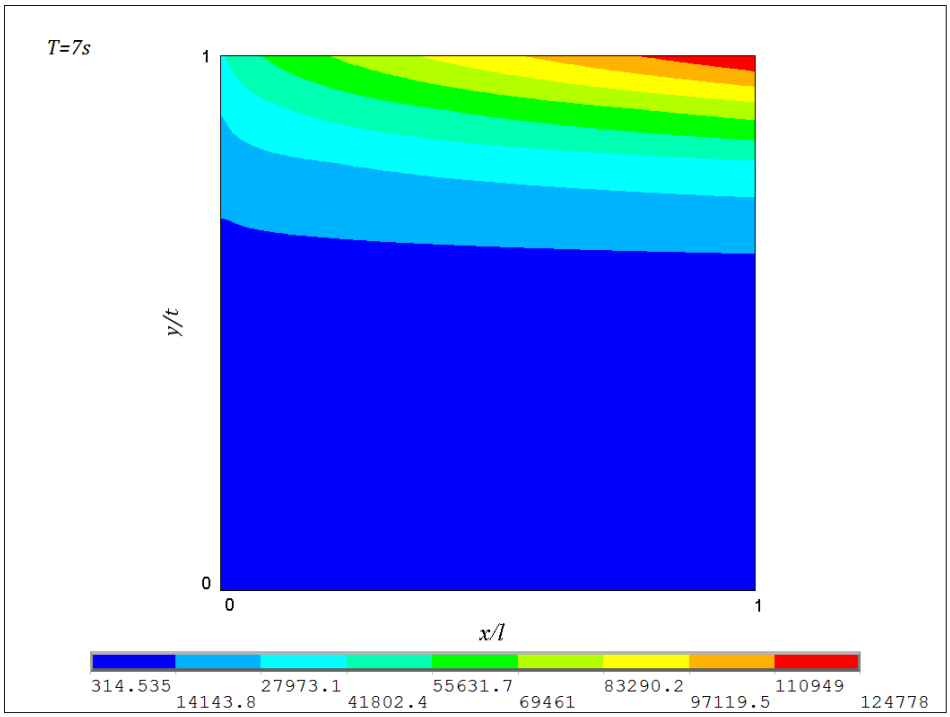

Figure 29. Plate temperature distribution at 7 seconds

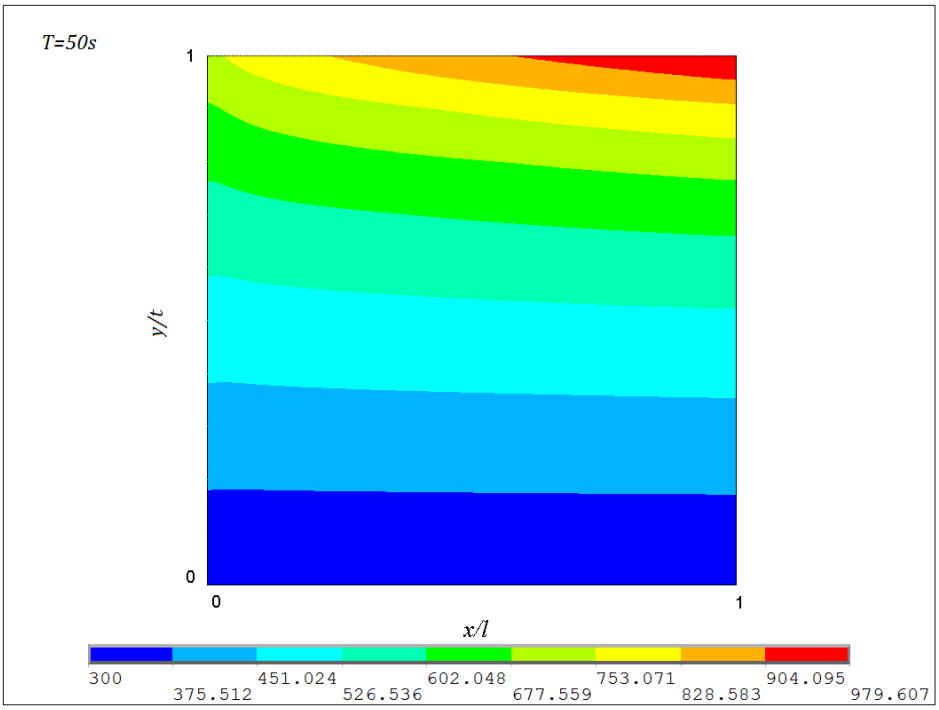

Figure 30. Plate temperature distribution at 50 seconds

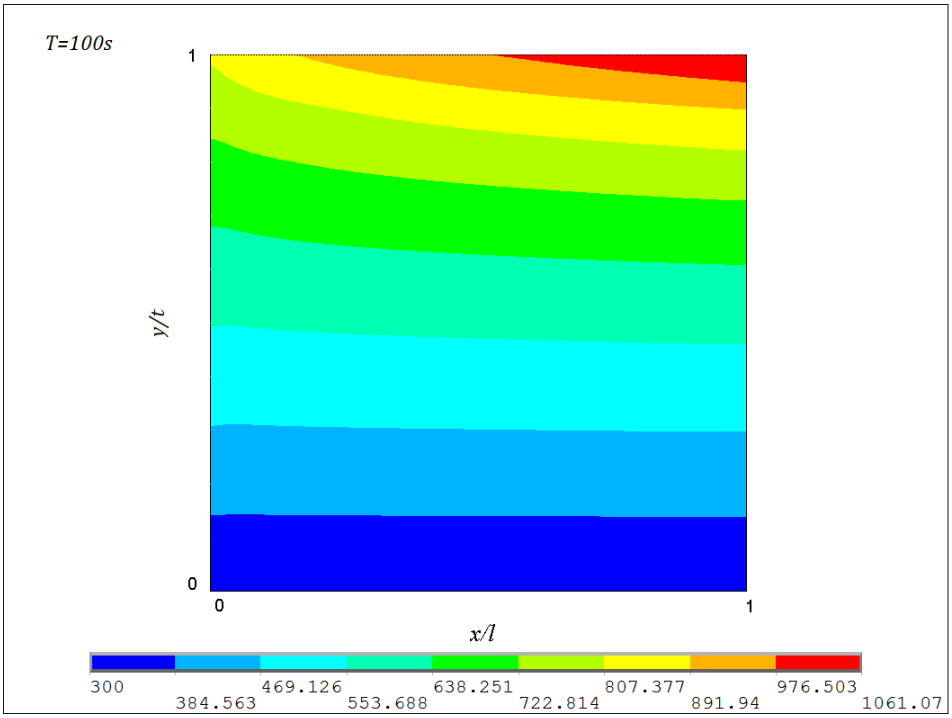

Figure 31. Plate temperature distribution at 100 seconds

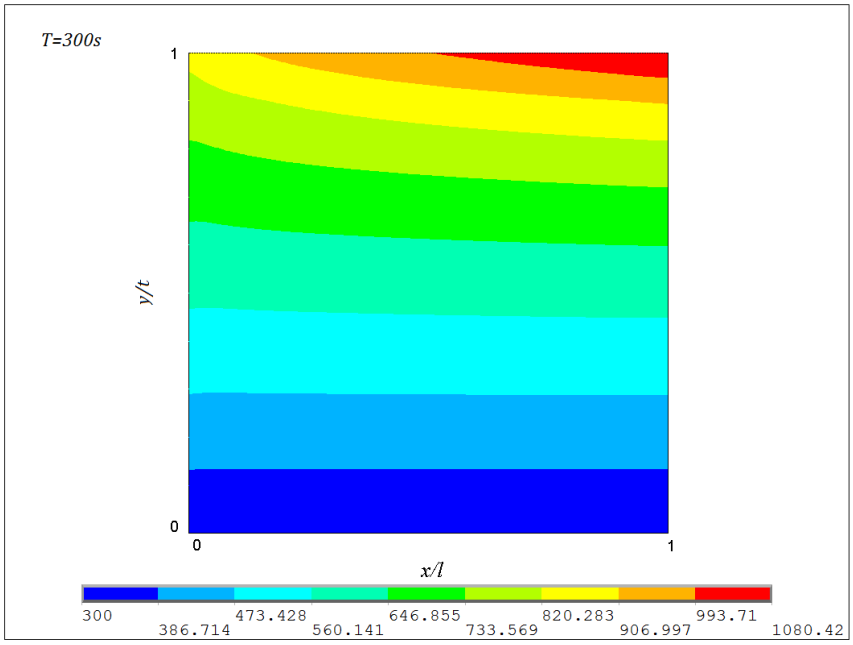

Figure 32. Plate temperature distribution at 300 seconds

At steady state, the temperature profile of the top surface is shown in Figure 33. Temperature is not distributed uniformly or linearly, because material properties vary nonlinearly.

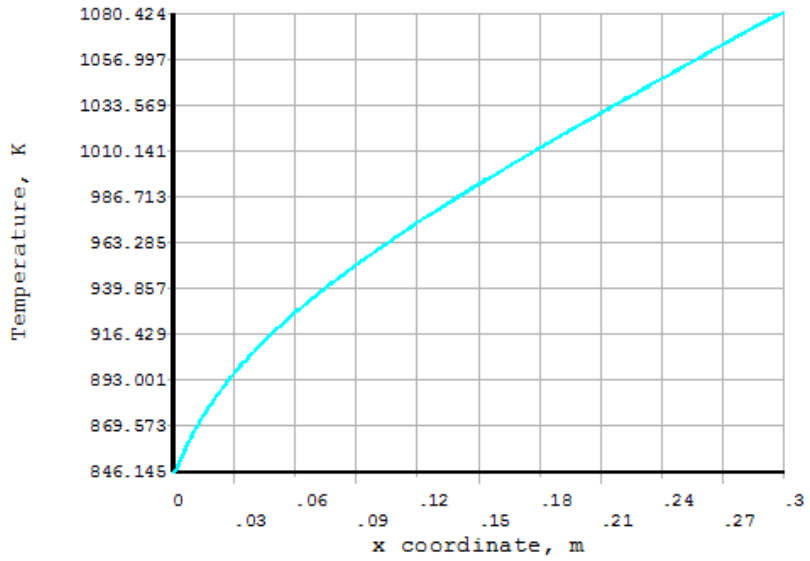

Figure 33. Top surface temperature profile at steady state

3.1.2 Transient structural analysis

As temperature distributions have been obtained from previous thermal analysis, by applying them as body force to each corresponding point on the plate, structural analysis can be performed. Preserving the plate's shape and meshing information, thermal element is changed to 2D 8 node quadratic structural solid elements under plane stress conditions.

The boundary condition is simply supported:

$$x = 0,\ y = 0: \quad U_y = 0,\ \ U_x = 0 \tag{52}$$

$$x = l,\ y = 0: \quad U_y = 0 \tag{53}$$

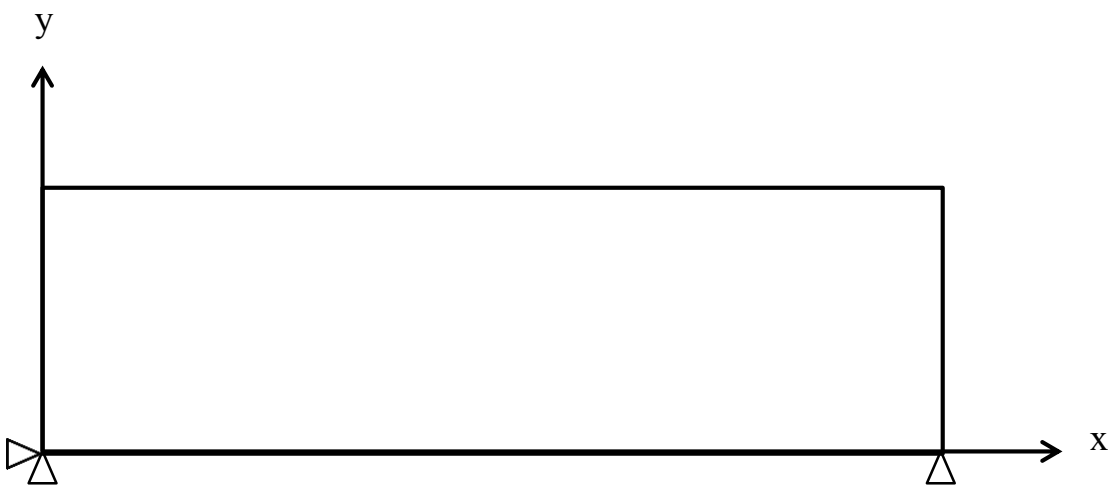

Figure 34. Boundary conditions of 2D FGM plate

The plate's maximum tensile and compressive stresses over the heating process are shown in Figure 35. '+' denotes tensile stress and '-' denotes compressive stress. It can be seen that both tensile and compressive normal stresses in x-direction are much larger than y-direction normal stresses and shear stresses. This is because metal alloy is graded in y direction and

ceramics are graded in x direction, which caused differences in overall material properties in x and y-directions. For example, as is shown in Figure 16, overall elastic modulus in x direction is higher than that in y-direction and this may lead to higher stresses in x-direction. As σ_x is more significant, next we focus mainly on the investigation of σ_x. It is also found that compressive stress is larger than tensile stress. This commonly happens in a heating process because the plate tends to expand, which induces internal compressive stress as a result of external constraints. Thermal stresses rise quickly in the first few seconds, and then decrease gradually to steady state values. Maximum tensile and compressive stresses in x-direction both happen at 7 seconds. Their values are 60MPa and -221MPa respectively. When reaching steady state, their values are 39.6MPa and -144MPa.

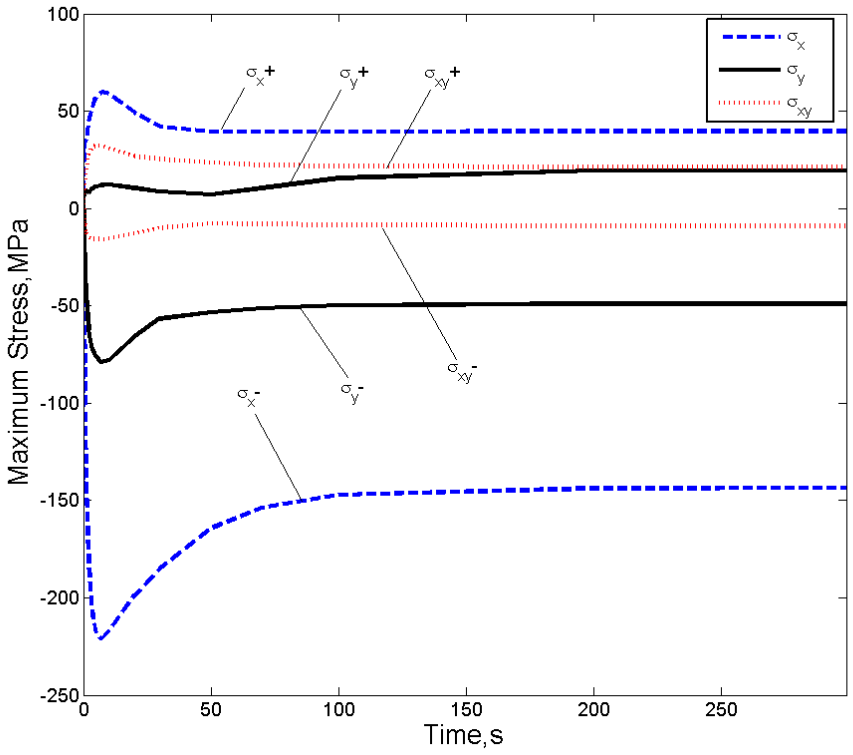

Figure 35. Maximum stresses during the heating process

The maximum first and second principal stresses are shown in Figure 36, which are denoted by σ_1 and σ_2. It can be found that their values are very similar to the tensile and compressive normal stress in x-direction. It is because normal stress in y-direction σ_y and shear stress τ_{xy} are much smaller compared to σ_x. Thus σ_x contributed mainly to the principal stresses. Maximum first and second principal stresses also happen at 7s. Their values are 60MPa and -221MPa respectively. When steady state is reached, the maximum principal stresses are 39.5MPa and -144MPa.

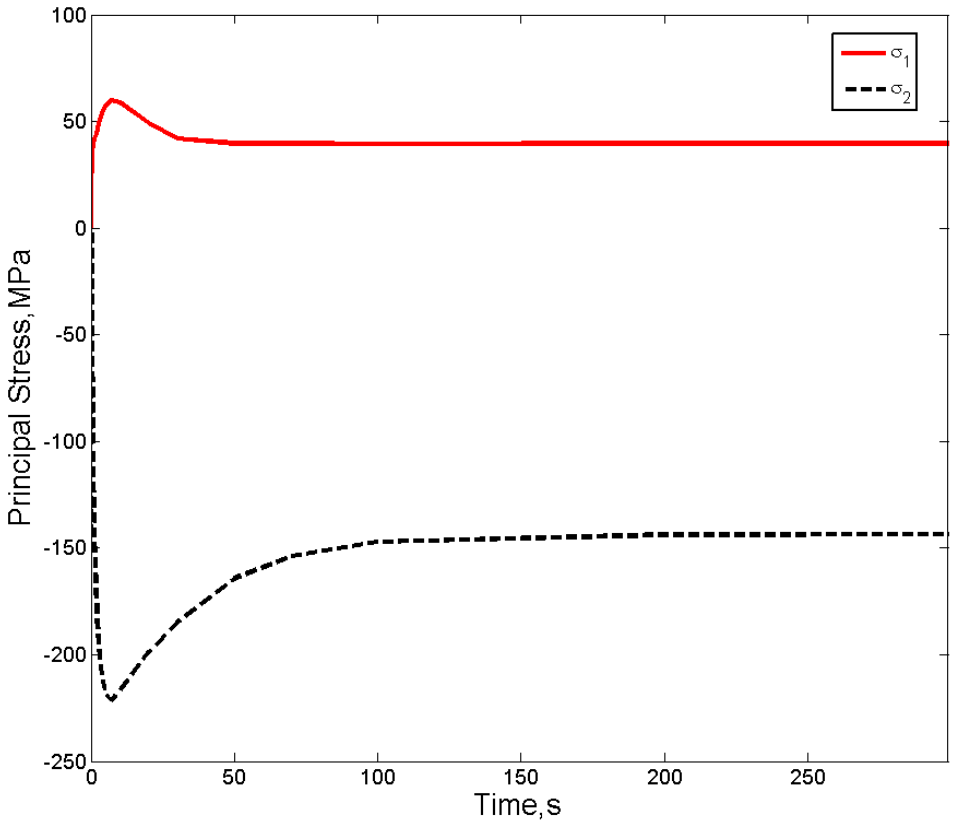

Figure 36. Maximum principal stresses during the heating process

Figure 37-Figure 42 shows x-direction thermal stress distribution of the plate at different moments. It can be seen that just 0.1 second after heating begins, compressive thermal stress emerges on the top surface. The absolute value of compressive stress decreases quickly over the narrow top region, which is followed by a tensile stress region as a reaction to sudden temperature change. During the first 7 seconds, thermal stresses grow larger and the tensile stress region also expands to the middle of the plate. After then, thermal stresses decrease gradually to a steady state value. The tensile stress region also grows first then reduces. During the entire heating process, the maximum compressive σ_x happens on the top surface near the right corner, where is ZrO_2 rich. This is mainly a result of higher temperatures in that region as shown in previous thermal analysis. Other material properties such as differences in Young's modulus, Poisson's ratio and coefficient of thermal expansion may also contribute to this result.

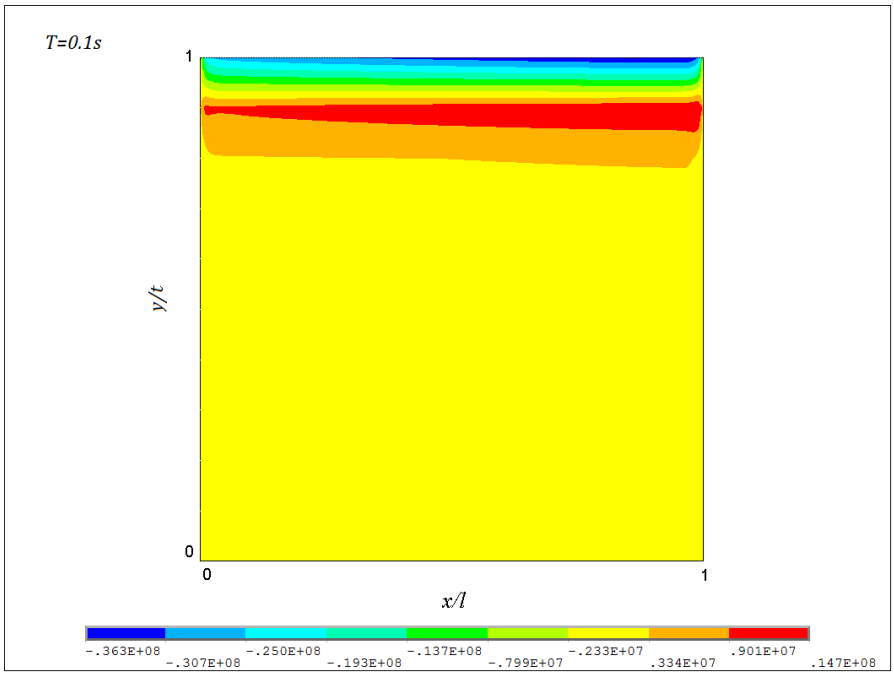

Figure 37. X-direction stress distribution at 0.1 second

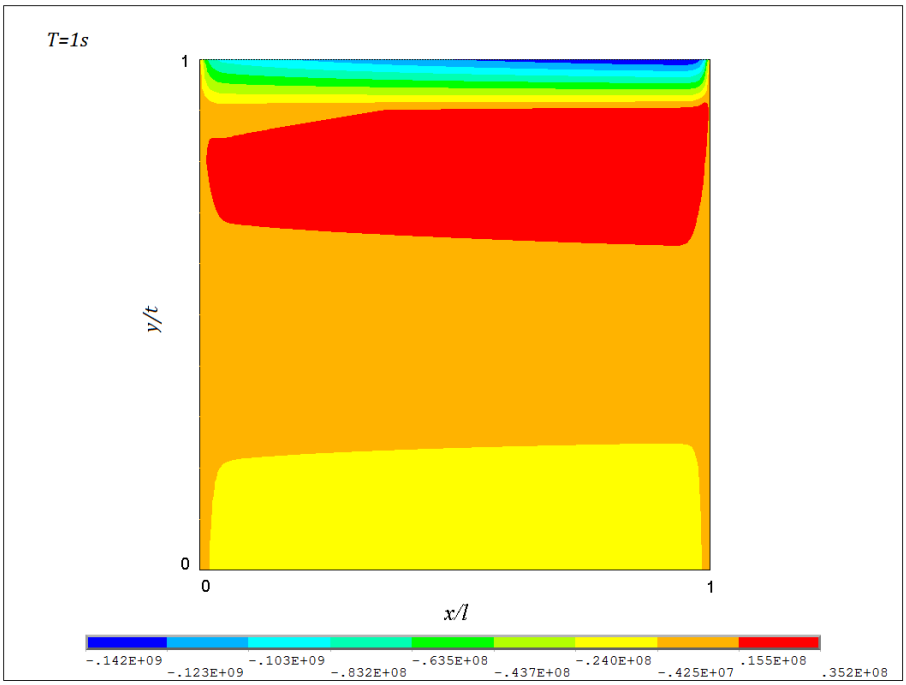

Figure 38. X-direction stress distribution at 1 second

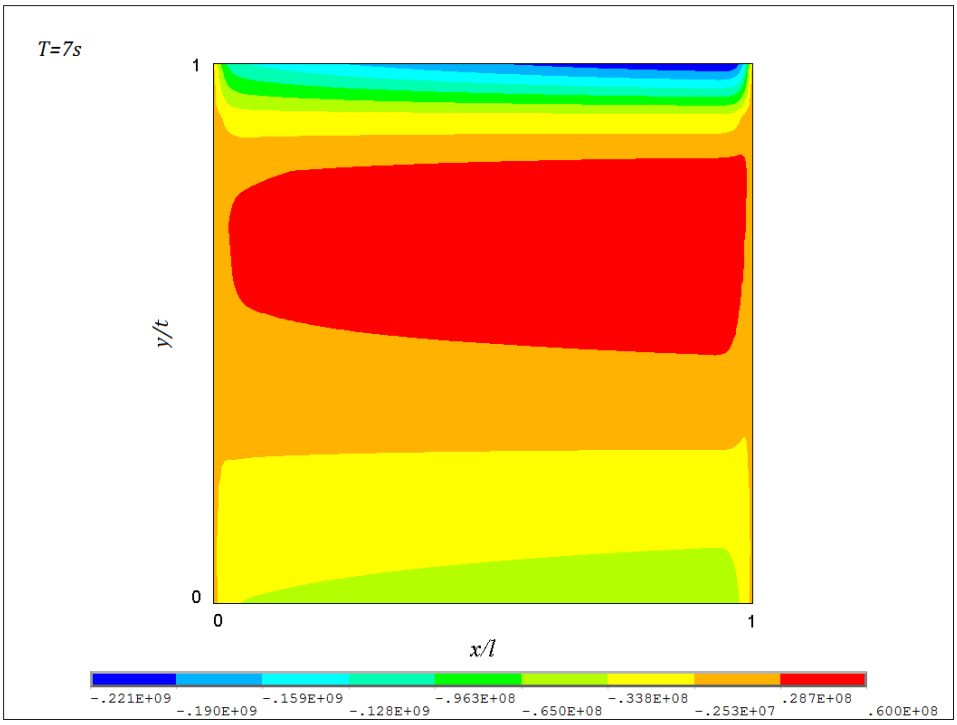

Figure 39. X-direction stress distribution at 7 seconds

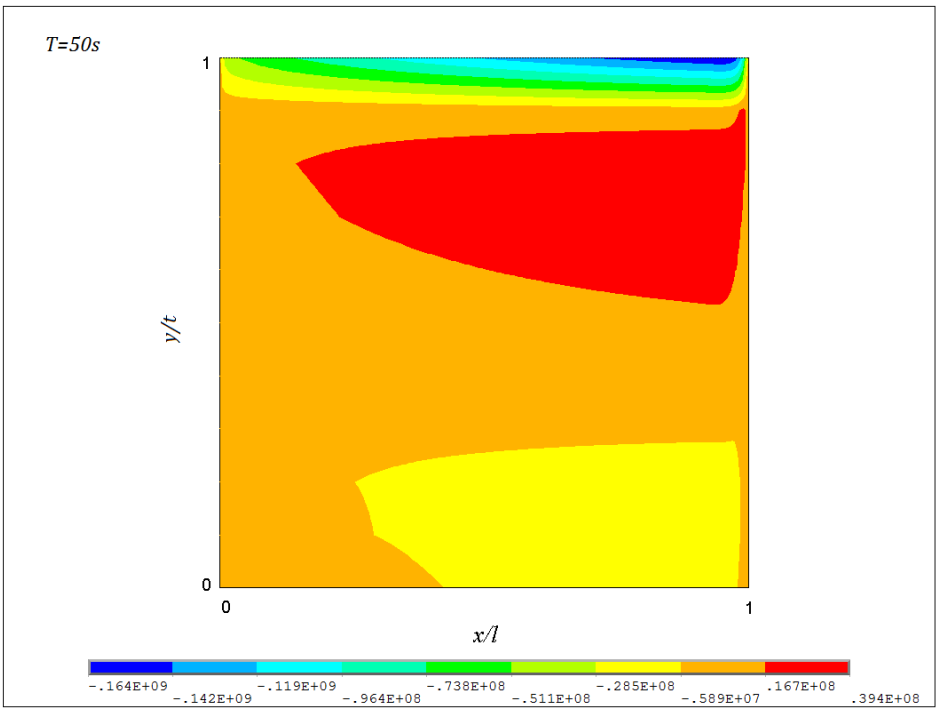

Figure 40. X-direction stress distribution at 50 seconds

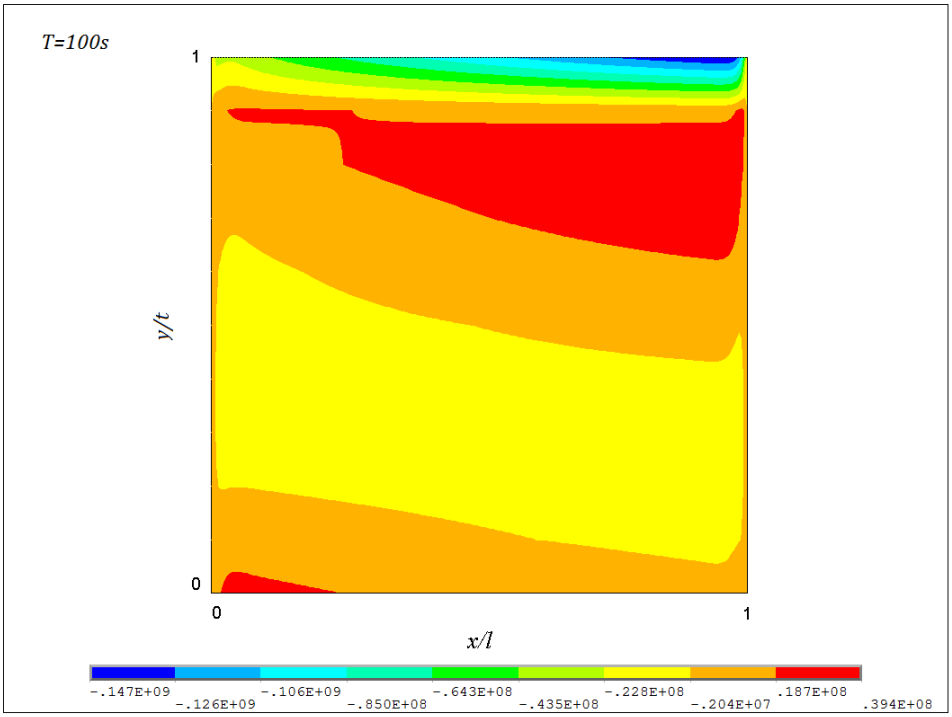

Figure 41. X-direction stress distribution at 100 seconds

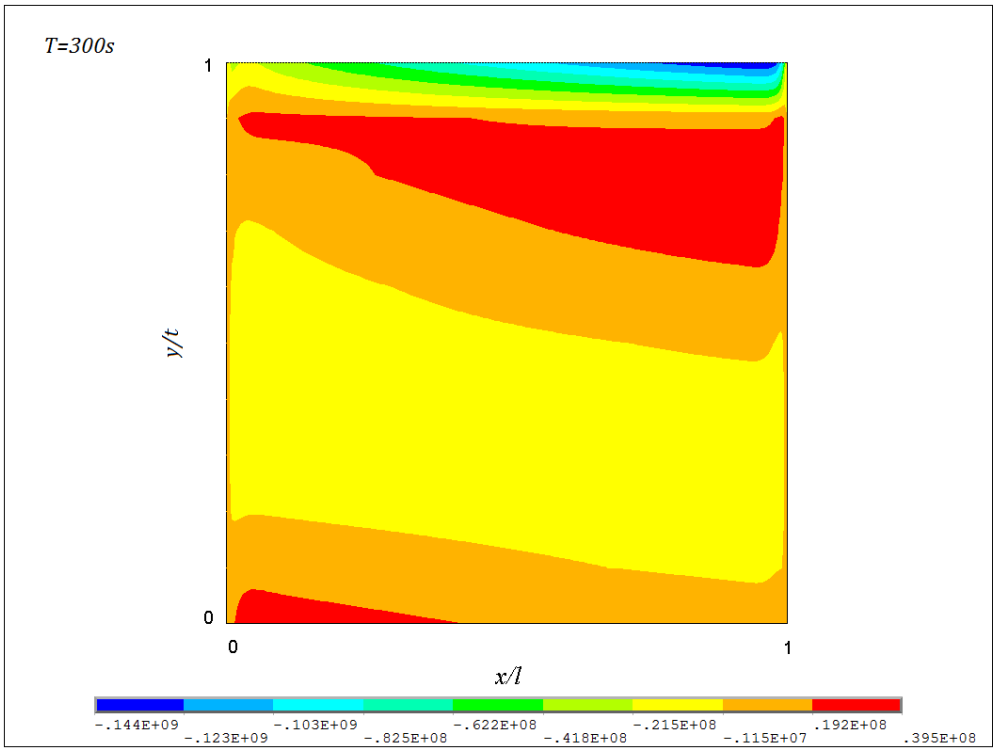

Figure 42. X-direction stress distribution at 300 seconds

3.2 SUDDEN COOLING STAGE

3.2.1 Transient thermal analysis

After the plate reaches steady state at 300 second, the top surface is subjected to a sudden cooling convection to 300K with a film coefficient h=1000 W/m^2• K.

The maximum temperature in the plate during the thermal shock process is shown in Figure 44. It can be seen that immediately after the cooling convection is applied, the plate's maximum temperature drops rapidly from the steady state temperature 1080.42K during the first 100 second of cooling. After then, the temperature slowly decreases to 300K.

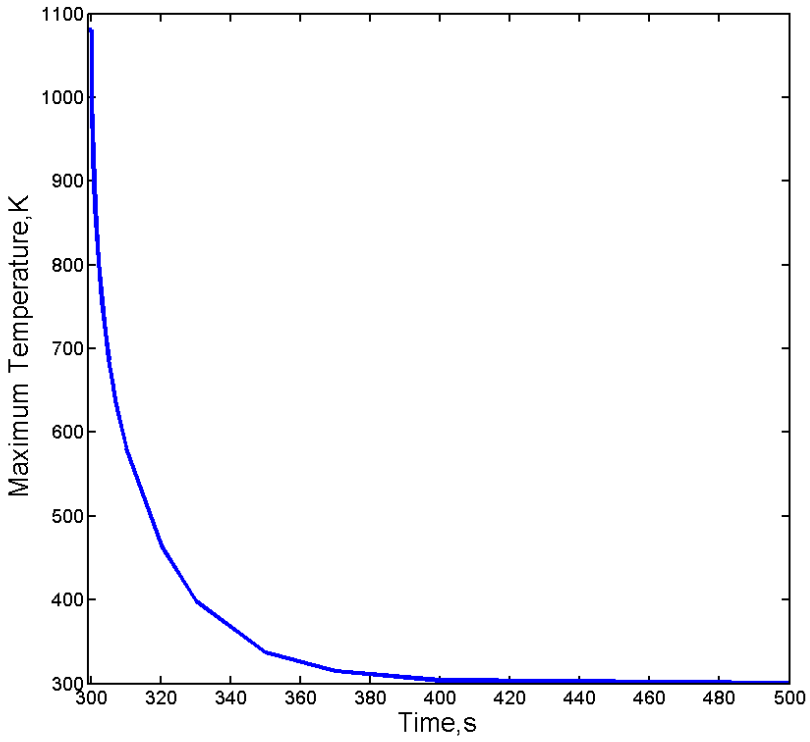

Figure 43. Maximum temperature during cooling process

Figure 44- Figure 49 show temperature distributions of the plate at different cooling times. It can be seen that after the cooling convection is applied, temperature of the top surface begins to decrease. As the plate is cooled from the top, the highest temperature region moves down towards the middle of the plate. Also, it moves from right to left, from ZrO_2 rich area towards Al_2O_3 rich area. This is because during the transient process, heat is transferred at different rate due material property differences such as thermal conductivity, heat capacity and density.

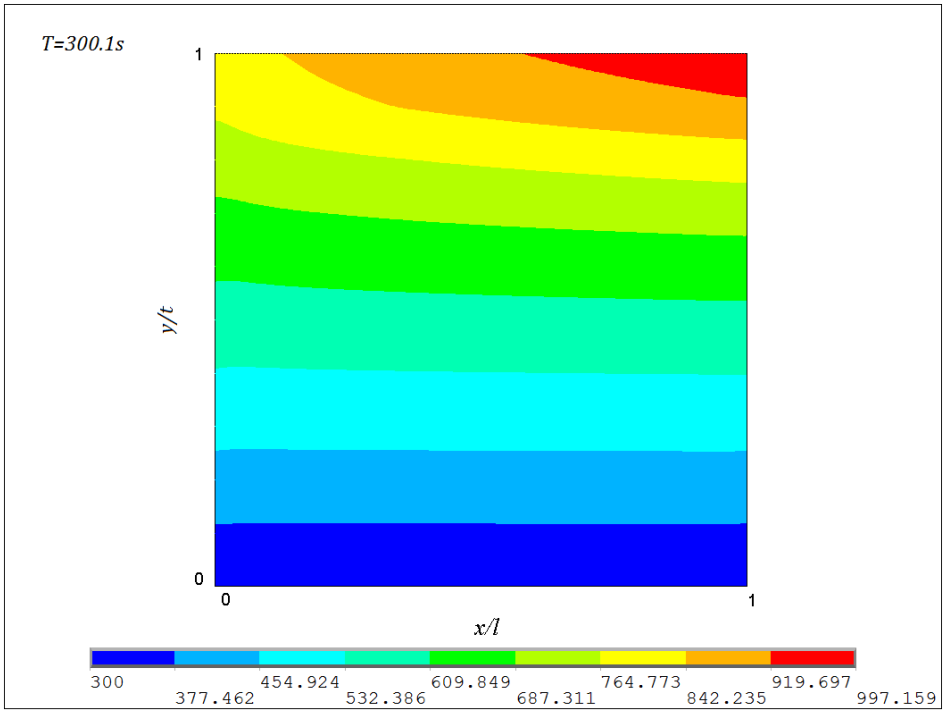

Figure 44. Temperature distributions at 300.1 seconds

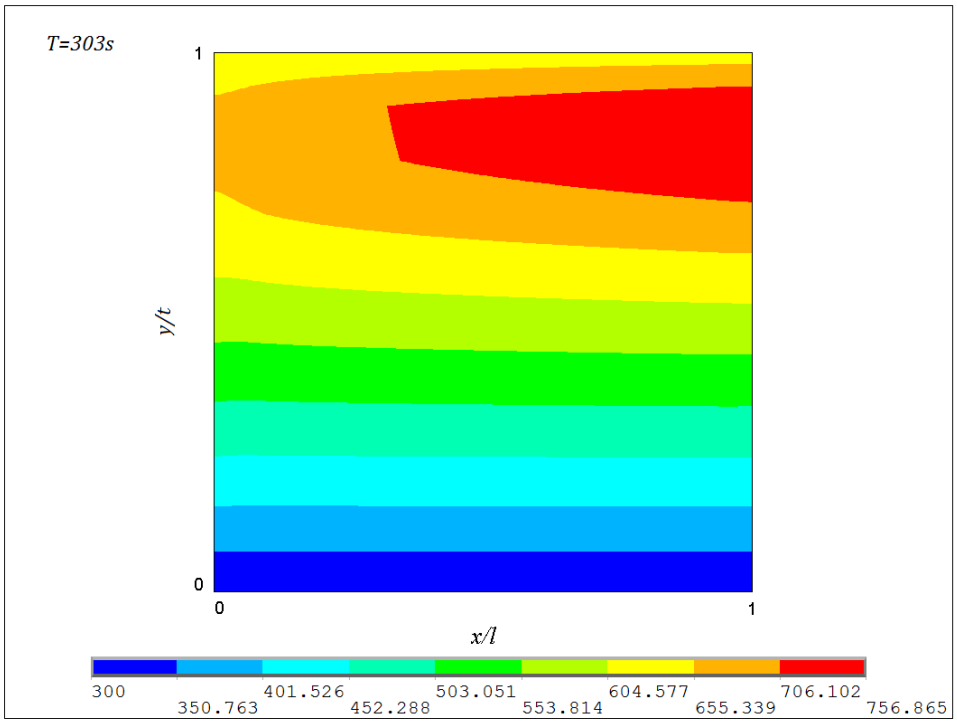

Figure 45. Temperature distributions at 303 seconds

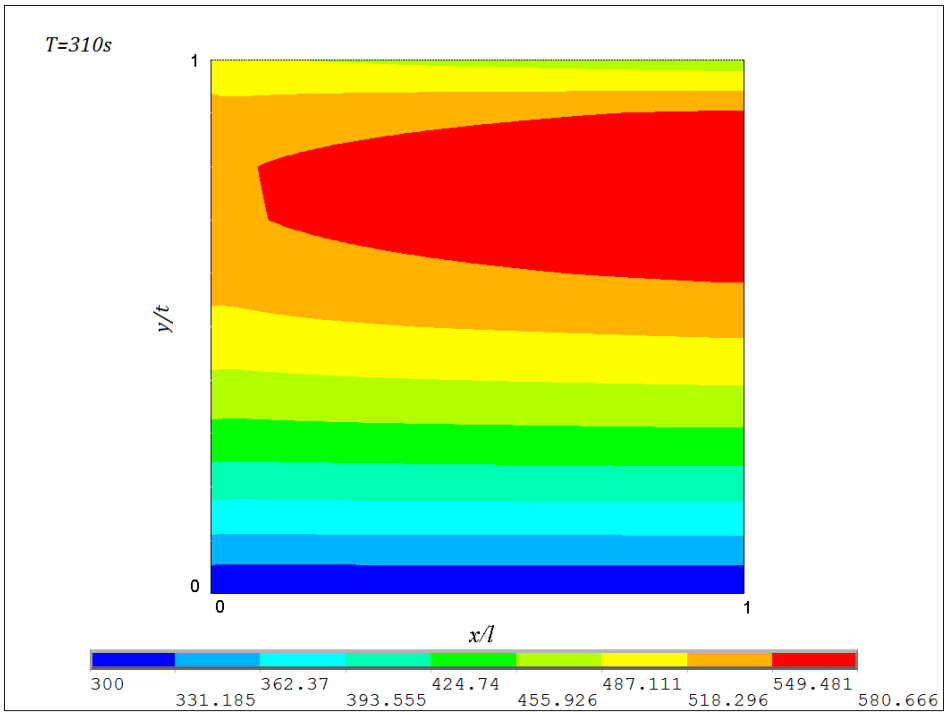

Figure 46. Temperature distributions at 310 seconds

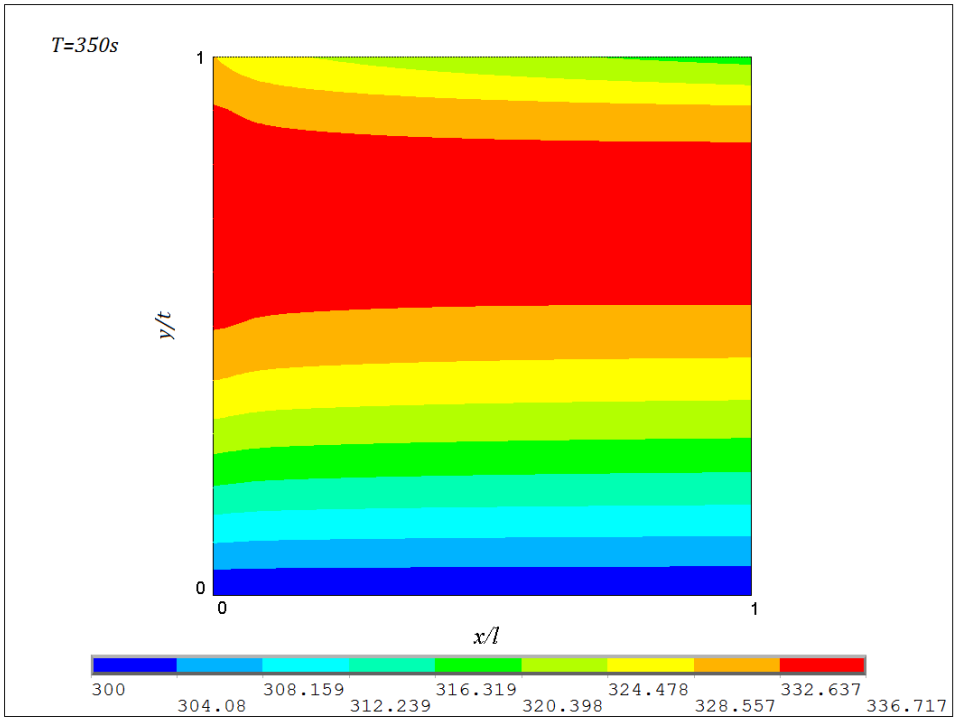

Figure 47. Temperature distributions at 350 seconds

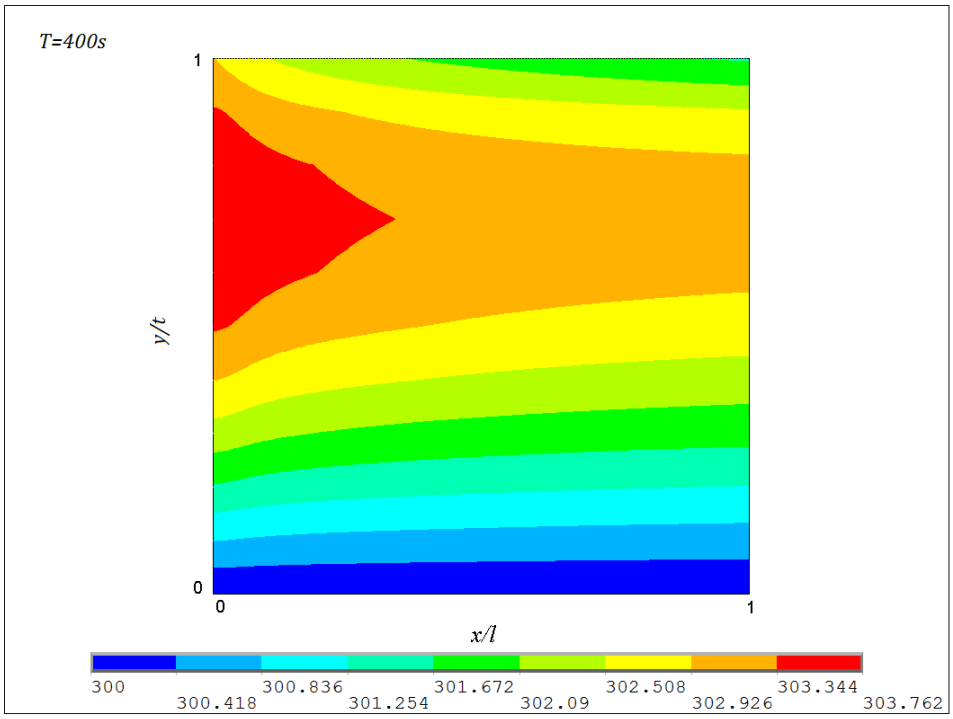

Figure 48. Temperature distributions at 400 seconds

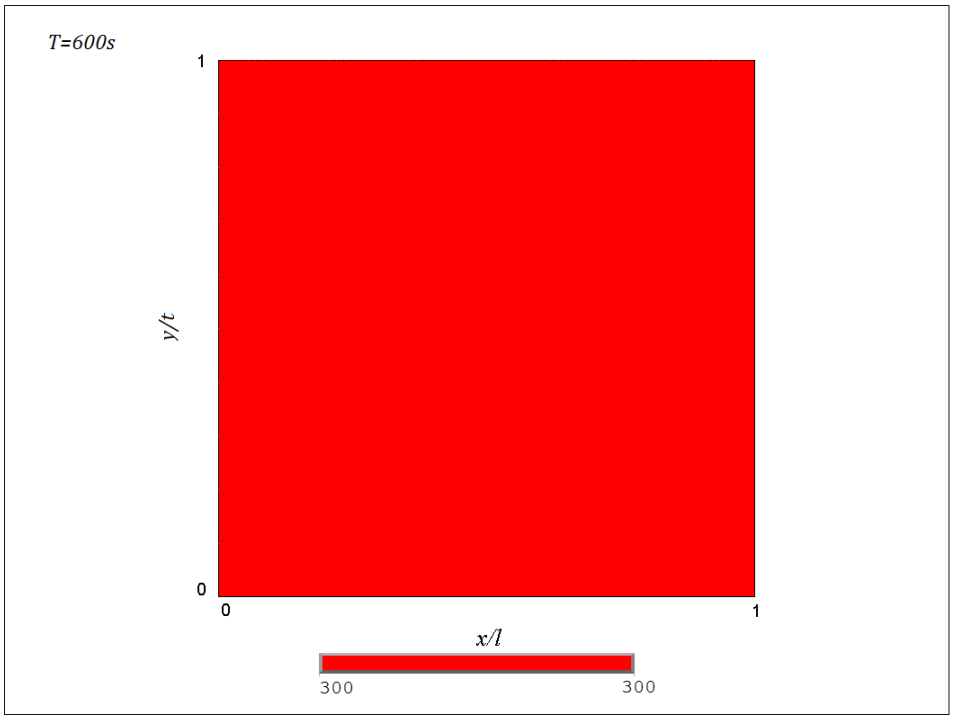

Figure 49. Temperature distributions at 600 seconds

3.2.2 Transient structural analysis

The plate's maximum tensile and compressive stresses over the sudden cooling process are shown in Figure 50. Similarly to the heating process, x-direction normal stress σ_x is significantly larger than y-direction normal stress σ_y and shear stress τ_{xy}. So we also focus on σ_x. Contrary to the heating process, it is found that tensile stress is larger than compressive stress. That is because when temperature drops, the plate tends to contract, but external constraints can cause internal tensile stress. Tensile stress rises quickly from the steady state value in the first few seconds, and then decrease gradually to almost zero. Maximum tensile stress in x-direction appears at 3 seconds after cooling, with a value of 292MPa, almost five times larger than the peak tensile stress during heating. When the cooling first begins, the absolute value of compressive stress quickly gets smaller, decreasing from 144MPa at steady state to 39.2MPa, just 0.1 second after cooling. Then the compressive stress increases slightly to a maximum 75.8MPa after 5 seconds of cooling. From then on, it slowly decreases to almost zero. During the cooling process tensile stresses are much larger than compressive stresses. Comparing to the heating process, tensile stresses are larger, while compressive stresses are smaller, because temperature drop tends to induce more tensile stress.

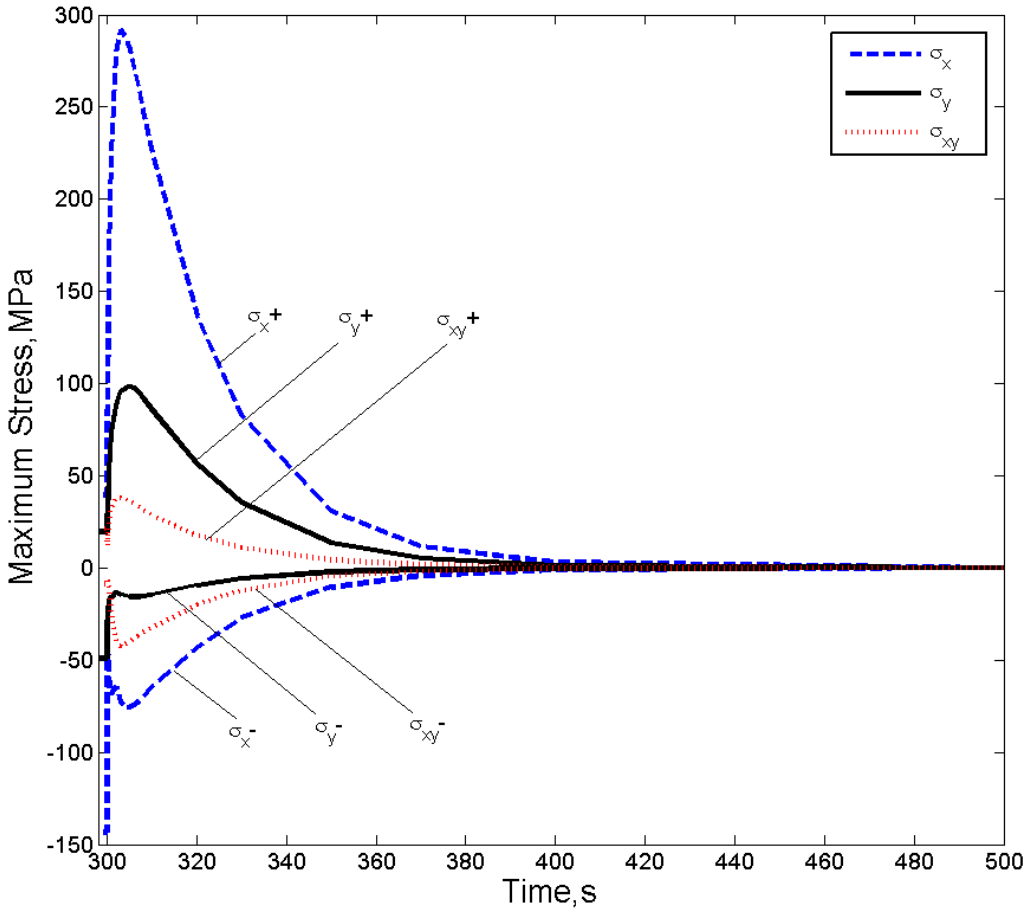

Figure 50. Maximum stresses during cooling process

The first and second principal stresses are shown in Figure 51. Their values are also very similar to the tensile and compressive normal stress in x-direction respectively, as σ_x is much larger than σ_y and τ_{xy}. Maximum first principal stress of 292MPa also appears at 3 seconds after cooling. The absolute value of second principal stress firstly decreases immediately after cooling, followed by a slight increase to a maximum at 305 seconds, then gradually drops to a negligible value.

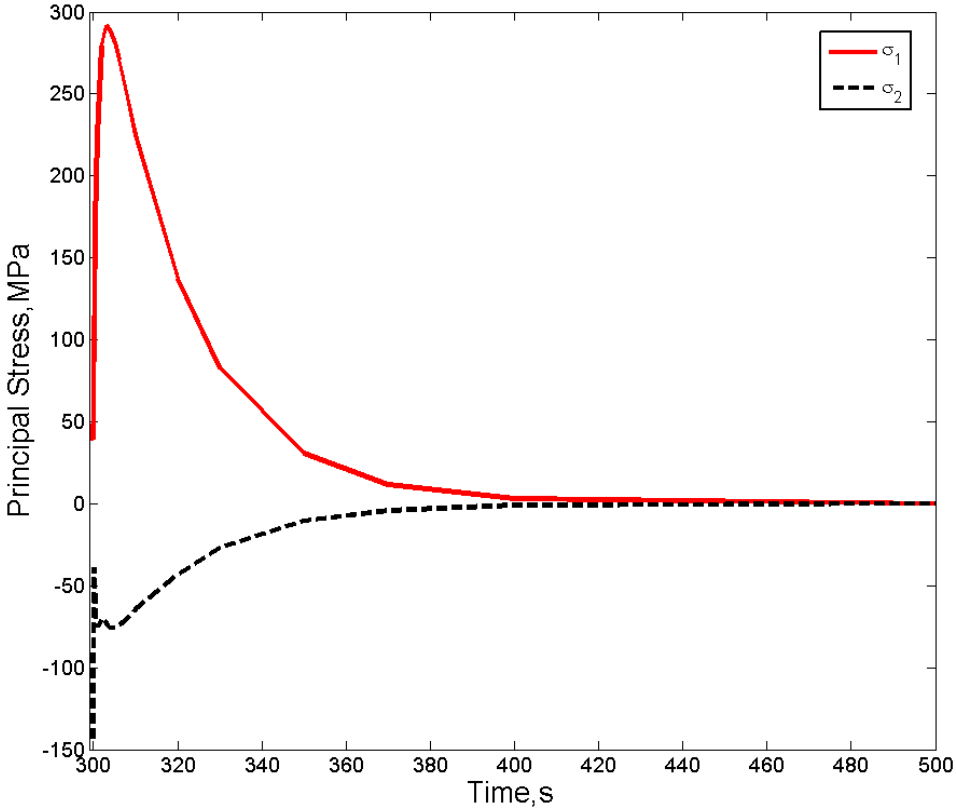

Figure 51. Maximum principal stresses during cooling process

Figure 52-Figure 57 shows x-direction thermal stress distribution of the plate at different cooling moments. It can be seen that just 0.1 second after sudden cooling begins, maximum tensile stress location moved from the middle of the plate at steady state to the left of top surface, but the upper right region is still in compression. 1 second after cooling, the stress state of the entire top surface changed from compression to tension. Tensile stress exists in a narrow top region, and the value decrease towards the bottom. A wide compressive stress region is located in the middle of the plate, followed by another tension region near the bottom. As analyzed previously, the maximum tensile stress increases at first and then slowly decreases to a negligible value, so does the absolute value of compressive stress.

The absolute value of compressive stress decreases quickly over the narrow top region, which is followed by a tensile stress region as a reaction to sudden temperature change. During the first 7 seconds, thermal stresses grow larger and the tensile stress region also expands to the middle of the plate. After then, thermal stresses decrease gradually to a steady state value. The tensile stress region also grows first then reduces. During the cooling process, the maximum tensile stress σ_x generally happens on the top surface near the right corner, where is ZrO_2 rich. At 600 seconds, the plate is completed cooled to uniform 300K. The value of residue stress is very small, only 12Pa at maximum.

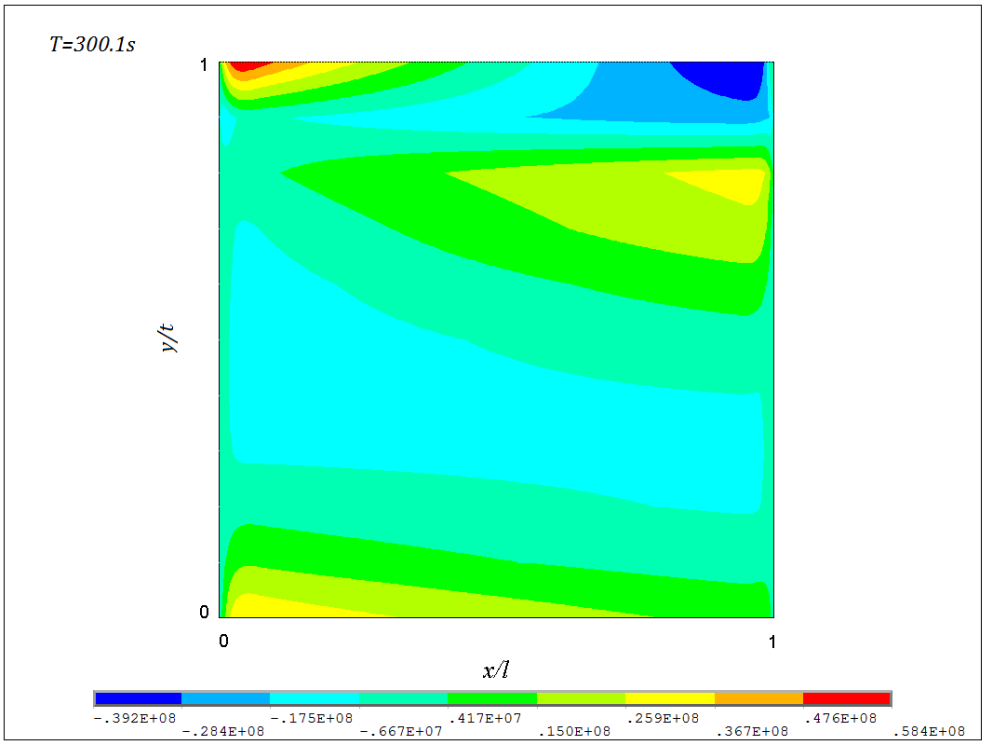

Figure 52. X-direction stress distributions at 300.1 seconds

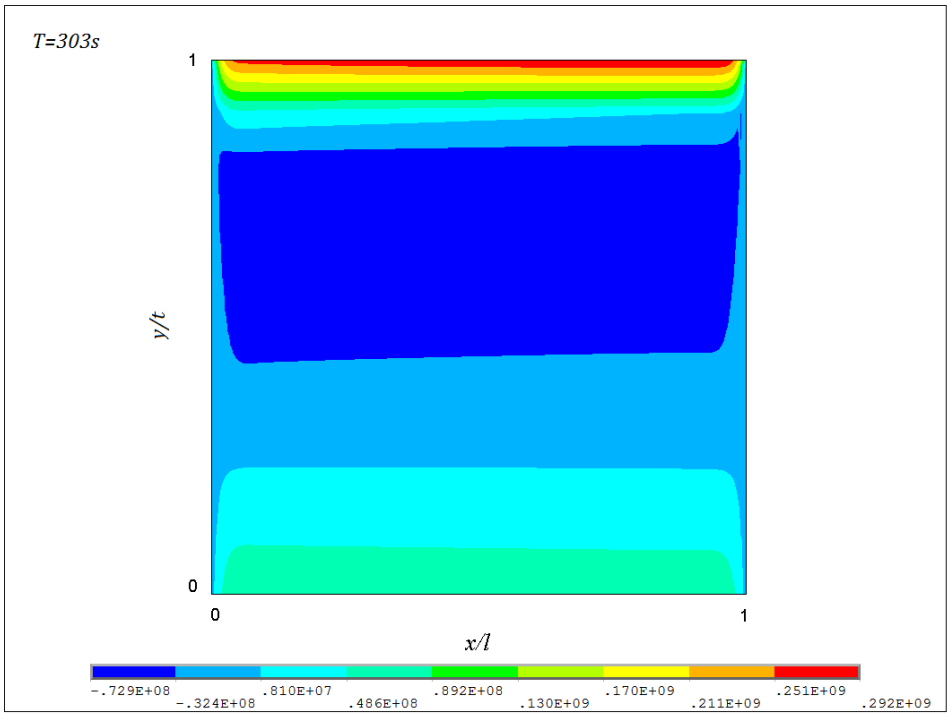

Figure 53. X-direction stress distributions at 303 seconds

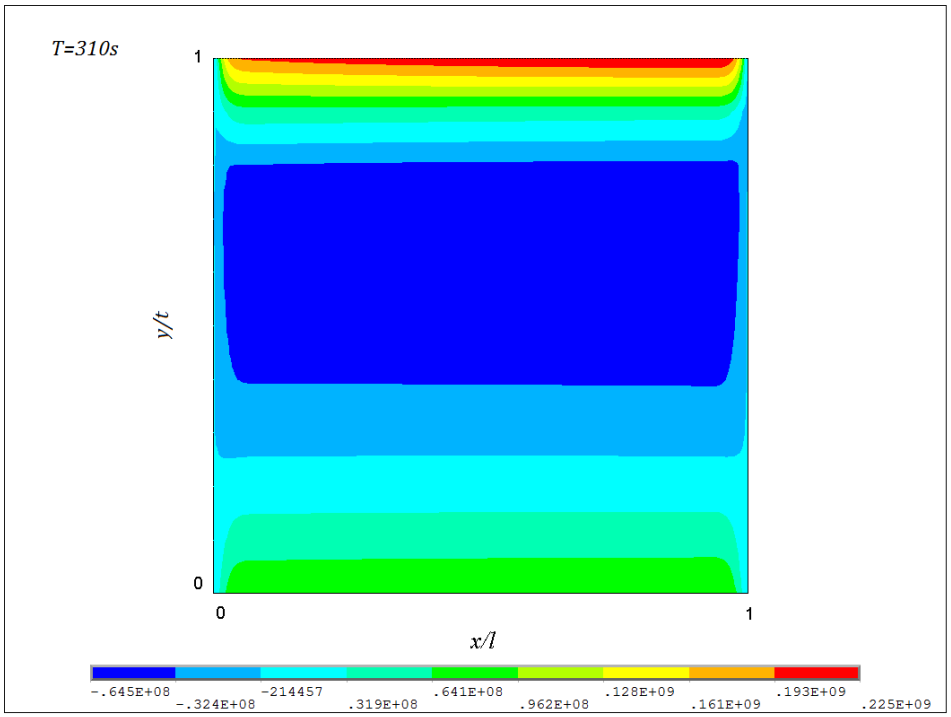

Figure 54. X-direction stress distributions at 310 seconds

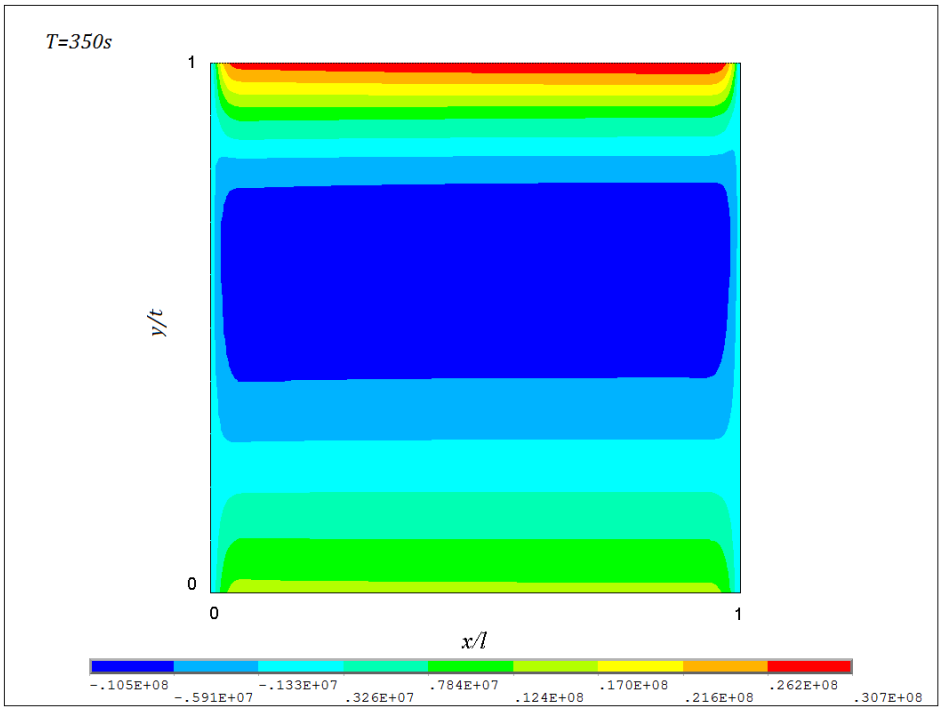

Figure 55. X-direction stress distributions at 350 seconds

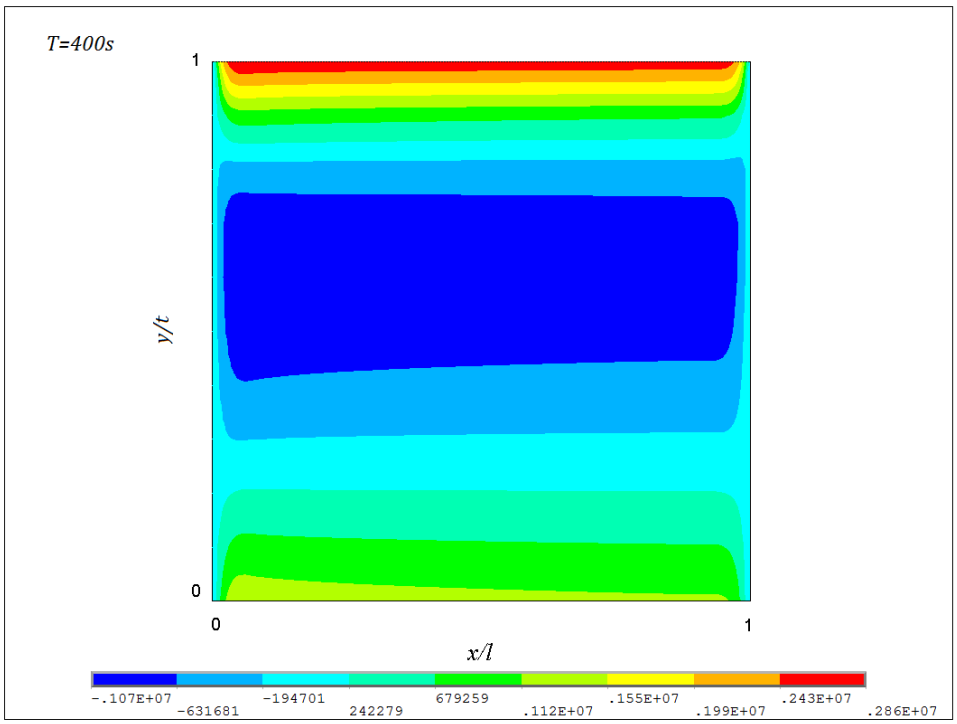

Figure 56. X-direction stress distributions at 400 seconds

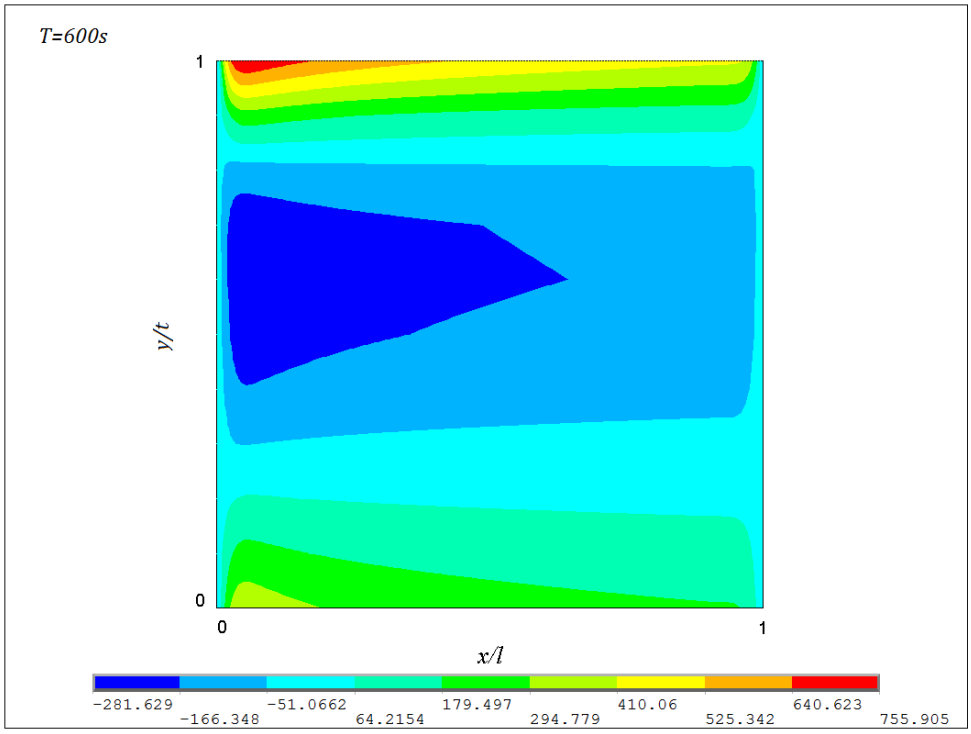

Figure 57. X-direction stress distributions at 600 seconds

3.3 FAILURE ANALYSIS

For a FGM that is used as thermal barrier coating, the ceramic rich side usually endures high temperature and thus has high thermal stress. If the stress exceeds the ceramic's tensile strength, cracks are likely to initiate, however, the metal phase may act as reinforcement. The primary toughening mechanisms of ceramic/metal FGM are crack deflection by the metal particles ahead of a propagating crack and crack front bowing by interaction between the crack front and particles. The crack deflection is considered to be a dominant toughening mechanism in ceramic rich side (Akira Kawasaki, 2002).

Because of FGM's heterogeneous structure, each position of the plate has a different value of critical stress. Failure criteria must be evaluated at all locations with respect to their individual strength. It has been known that the fracture toughness, *Kc* of ceramic/metal FGM increases with the volume fraction of the metal phase. Experimental data (Akira Kawasaki, 2002) show that Kc approximately follow rule of mixtures. Because *Kc* is linearly related to stress, rule of mixtures can also be used to estimate critical stress of a FGM. At each location, critical stress is given by a volume based average of each material. When the stress state is tension, we use the tensile strength of the ceramics and for compression, compressive strength is used:

$\sigma > 0$:

$$\sigma_Y = V_1\sigma_{ut1} + V_2\sigma_{ut2} + V_3\sigma_{Y3} \tag{54}$$

$\sigma < 0$:

$$\sigma_Y = V_1\sigma_{uc1} + V_2\sigma_{uc2} + V_3\sigma_{Y3} \tag{55}$$

As ceramics are brittle materials, we choose maximum principal stress criterion to analyze failure. A normalized stress is introduced. It is defined as the principal stress normalized by each point's own critical stress.

$$\bar{\sigma} = \frac{\sigma}{\sigma_Y} \tag{56}$$

As long as the absolute value of the normalized stress is less than 1, which means the stress does not exceed critical stress, the material will not fail.

As the top region generally has higher temperature and higher stresses, failure may initiate from there. We define two normalized principal stresses $\overline{\sigma_1}$ and $\overline{\sigma_2}$, their values are calculated by the above equations.

Figure 58 shows the normalized stresses during the entire heating-cooling cycle. It can be seen that during the first few moments of sudden cooling, the tensile normalized stress greatly rises. Thus we can conclude, during the entire process, failure is most likely to happen at the beginning of thermal shock. In this case, $\overline{\sigma_1}_{max}$ = 0.92, which indicates the material will not fail, but very close to.

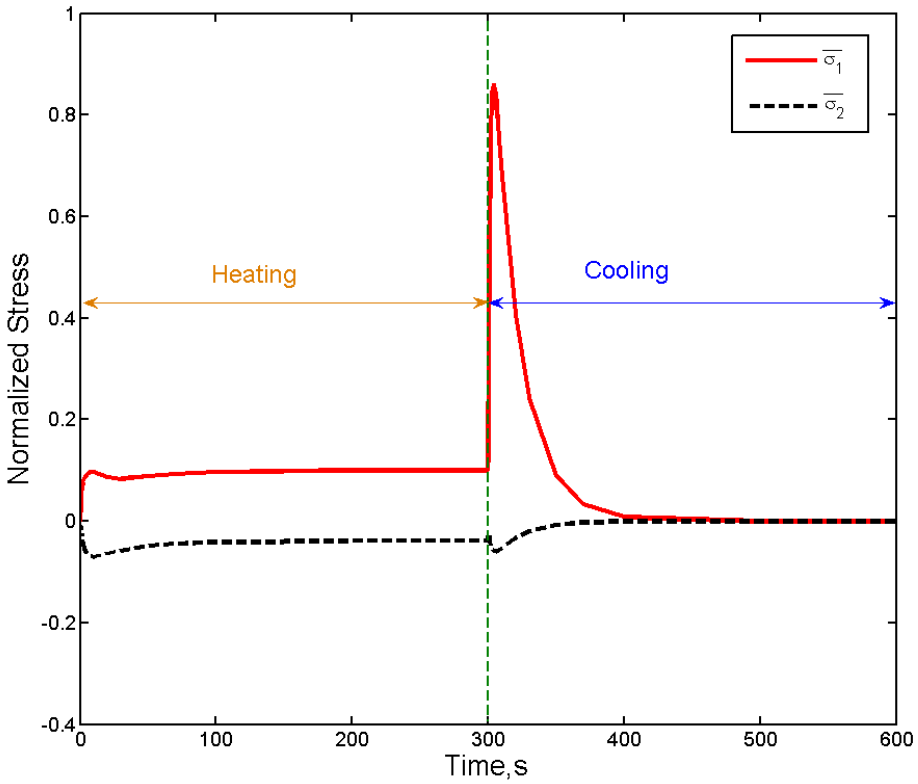

Figure 58. Normalized stress during the heating-cooling cycle

If the applied heat flux is q=400kW/m^2, the plate will be heated to higher temperatures and higher thermal stresses are induced. The normalized stresses are shown in Figure 59. It can be seen that $\overline{\sigma_1}_{max}$ = 1.14, which indicates failure will occur.

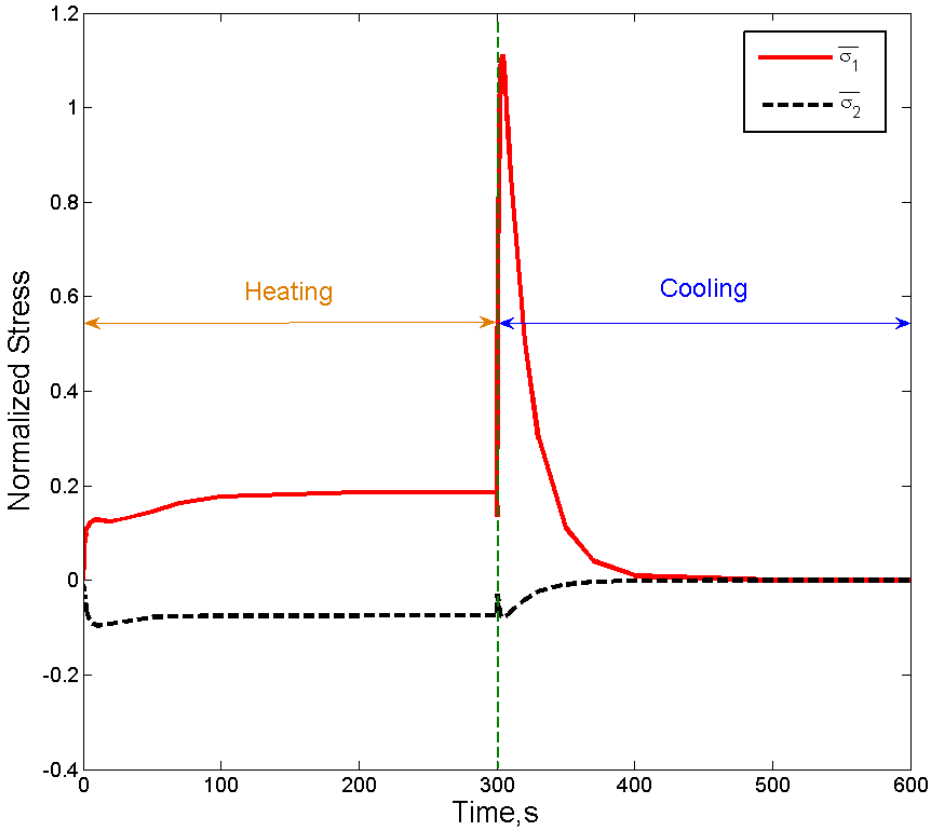

Figure 59. Normalized stress during the heating-cooling cycle with a heat flux of 400kW/m^2

4.0 EVALUATION OF DESIGN PARAMETERS AND BOUNDARY CONDITIONS

In this chapter, we studied the influences of design parameters on the thermoelastic performance of FGMs. By changing the power law indices in the volume fraction rules, we find an optimal FGM structure that is least likely to fail. We also investigated how the plate shape would affect temperature and stress distributions. Results of clamped boundary conditions are compared with simply supported boundary conditions.

4.1 INFLUENCE OF VOLUME FRACTION LAW

One of the most important advantages of FGMs is that their structures can be customized to meet special needs of a specific working environment. Assuming the volume fraction rules follow a power law defined by Eq.(1)-(3) . We can change the FGM plate's structure by just changing the power law indices m and n. Next we study their influences on the thermoelastic performance of the FGM plate. For simplicity, we study a steady state case. The plate dimensions are same as above, l=300mm, t=15mm, with simply supported boundary conditions. Assuming the top surface temperature varies linearly from 1000K to 1700K from left to right as shown in Figure 60, and the bottom surface is held at 300K. The steady state temperature distribution of the plate is shown in Figure 62.

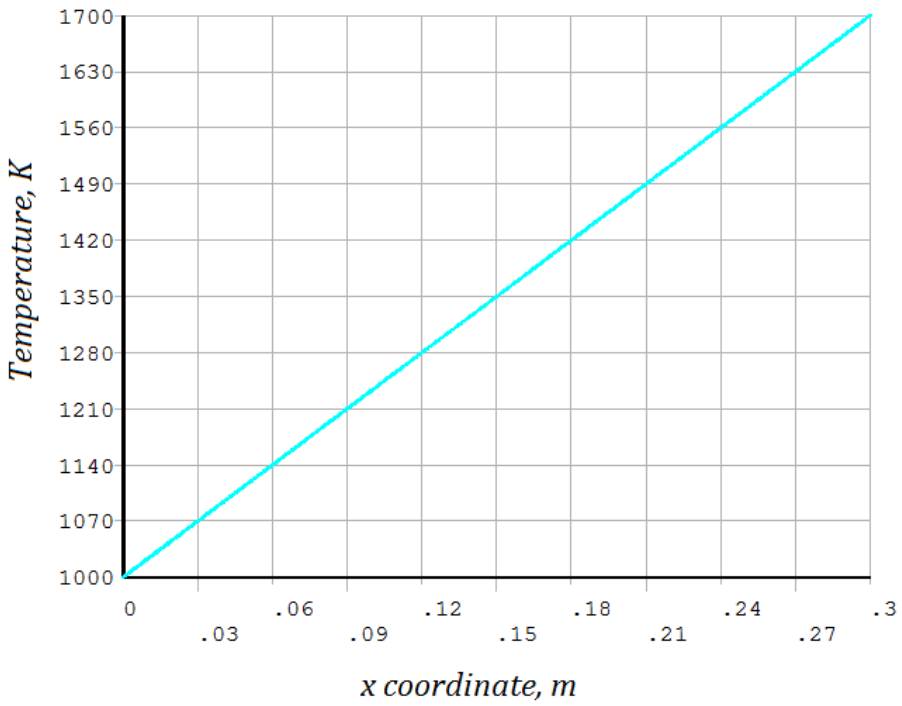

Figure 60. Top surface temperature profile

Previously we introduced normalized principal stresses as a measure of failure. The smaller it is, the better material performance will be. We also know that FGMs are more likely to fail in tension. We varied the values of power law indies m, n and studied their influences on normalized principal stress $\overline{\sigma_1}$. The results are shown in Table 2 below. It can be seen that when m=1 and n=5, $\overline{\sigma_1}$ takes the minimum value, 0.425124. Under other conditions, $\overline{\sigma_1}$ can be as high as 0.98, which indicate near failure. We can conclude that a FGM's structure has a great influence on its overall performance. Thus in order to make the best use of a FGM, we must try to optimize its structure according to the given geometry and working conditions. From the volume fraction law defined above, we can see that volume fraction of Ti-6Al-4V increases with n. With a fixed n value, when m increases, volume fraction of Al_2O_3 increases and volume fraction of ZrO_2 decreases. In this case, the volume fraction law corresponding to m=1 and n=5

yields the optimal FGM structure. n=5 means in the thickness direction the material is Ti-6Al-4V rich and m=1 means the composition of ZrO_2 and Al_2O_3 vary linearly from across the length of the plate.

Table 2. Normalized principal stresses for different values of m and n

n \ m	0.1	0.3	1	3
0.3	0.975815	0.9638	0.926492	0.858537
1	0.889828	0.888308	0.87699	0.835858
3	0.573075	0.575389	0.578881	0.571467
5	0.426962	0.42656	0.425124	0.426865
7	0.762855	0.780466	0.839876	0.7555

Next we compare some typical structures to study the influences of volume fraction laws.

Table 3. Selected cases for different values of m and n

case (a)	m=0.3, n=5
case (b)	m=1, n=5
case (c)	m=3, n=5
case (d)	m=1, n=0.3
case (e)	m=1, n=1
case (f)	m=1, n=7

Variation of volume fractions are shown in Figure 62. From (d)~(f), we can see that as n increases, volume fraction of Ti-6Al-4V increases. From (a)~(c), when n is fixed and as m increases, volume fraction of Al_2O_3 also increases.

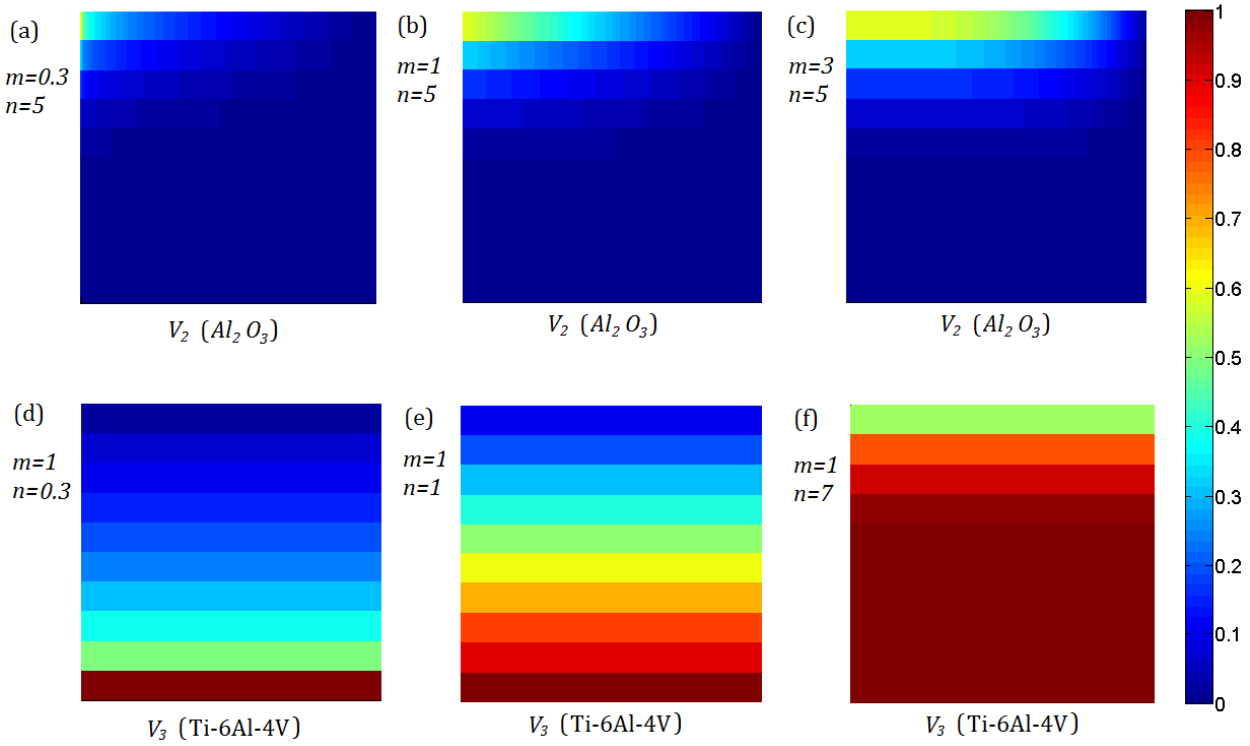

Figure 61. (a)-(c):Volume fractions of Al_2O_3, (d)-(f):Volume fractions of Ti-6Al-4V

Temperature distributions are shown in Figure 62. From (d)~(f), as volume fraction of Ti-6Al-4V increases, area of high temperature region reduces. This is because Ti-6Al-4V has a higher thermal conductivity. From (a)~(c), there is also a slight increase of high temperature region, as Al_2O_3 has a higher thermal conductivity than ZrO_2.

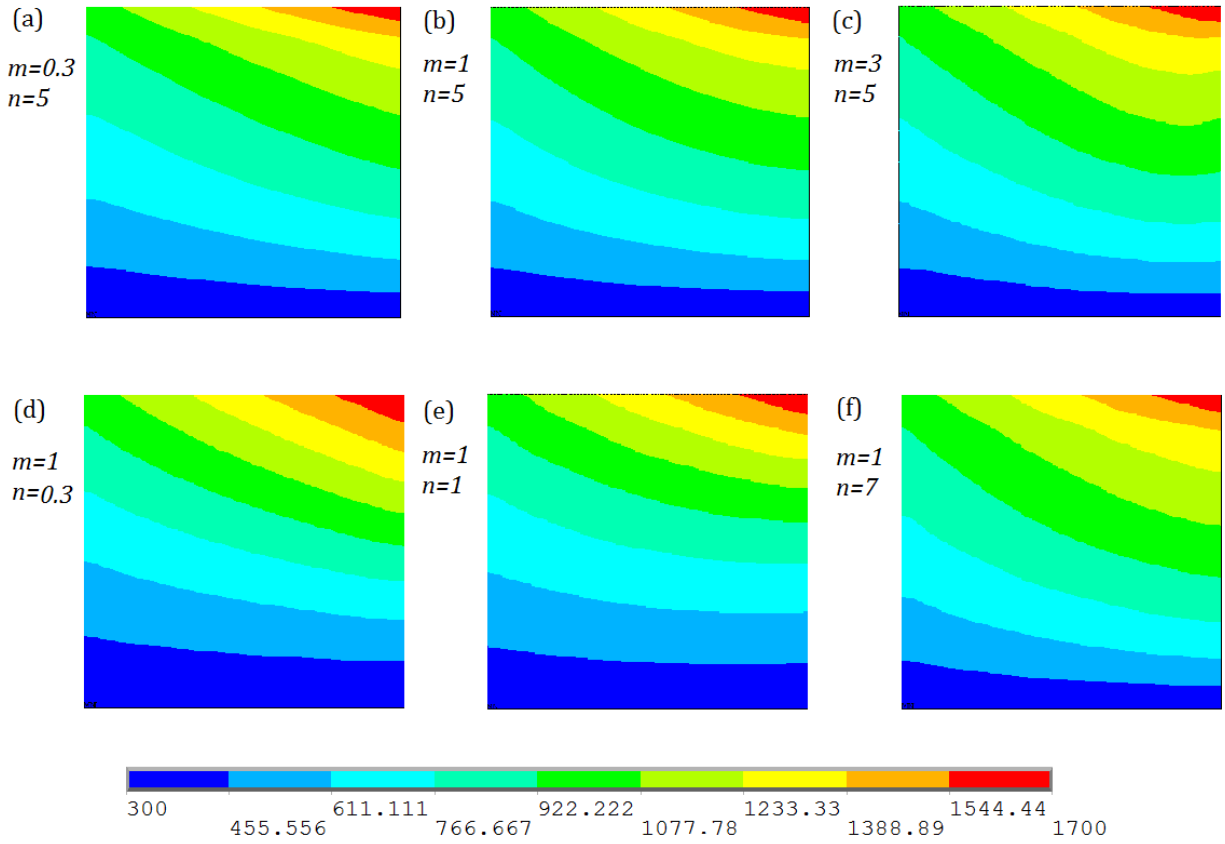

Figure 62. Temperature distributions for different m and n values

Normal stresses in x-direction are shown in Figure 63. From (d), (e), (b), (f), we can see that when n increases, high tension regions decrease and move up towards the top. That's because the composition of Ti-6Al-4V increases and as an alloy it has a better ductile performance than the ceramics ZrO_2 and Al_2O_3. Maximum tensile stress fluctuates as n increases, as each time it happens in a different location. The minimum is when n=5. Maximum compressive stress increases first then decreases with n. The minimum is -197MPa when n=7. From (a)~(c), n is fixed and as m increases, high tension region, maximum tensile and compressive stresses both decrease, indicating adding more Al_2O_3 may bring stresses down.

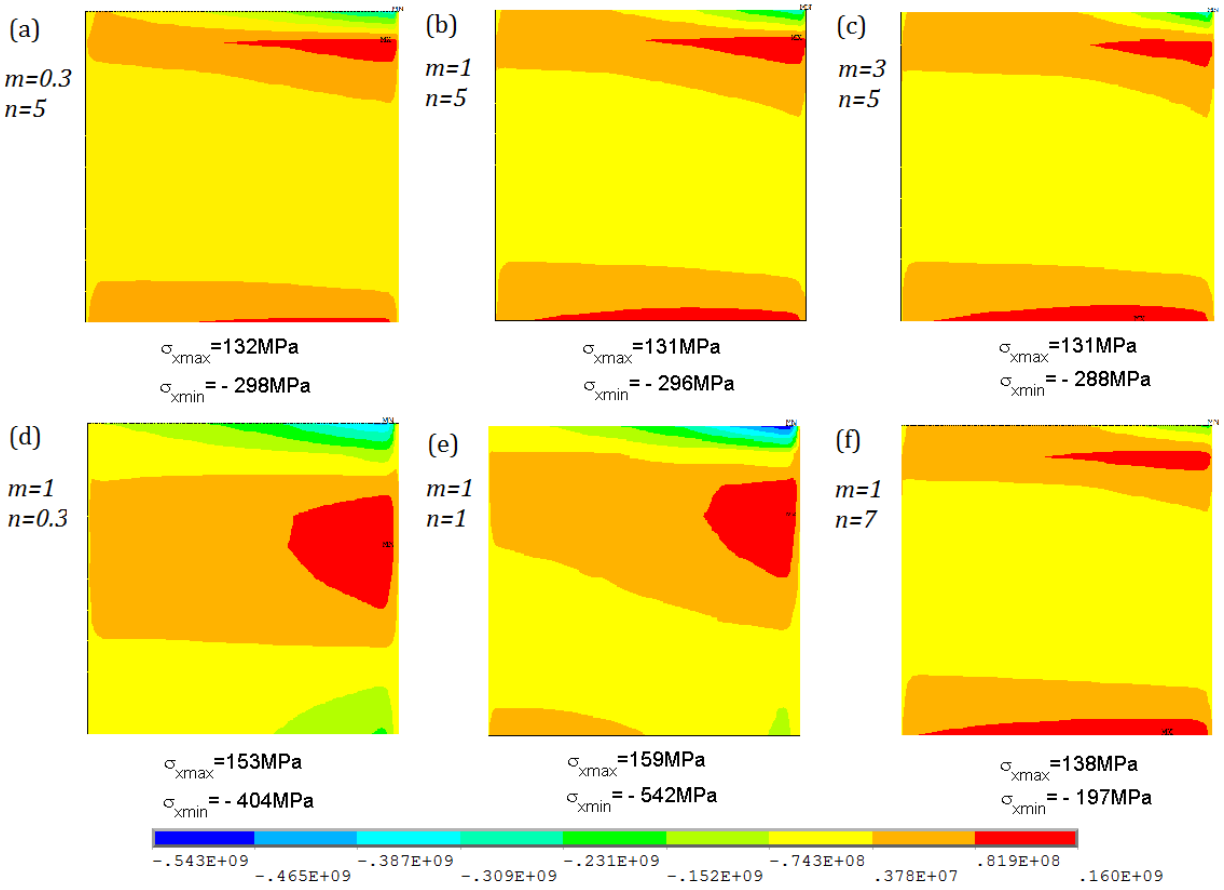

Figure 63. Stress distributions for different m and n values

As FGMs are more likely fail in tension, normalized first principal stresses are analyzed. The results are shown in Figure 64. The minimum is when m=1 and n=5. Although when m=3, the stress is lower, but the maximum normalized stress does not happen in the same location where the stress is highest, because it is normalized with critical stress. Each location has a unique critical stress and a different volume fraction rule may also lead to a different value. Similarly, although (d) has a lower stress than (e), it is more likely to fail.

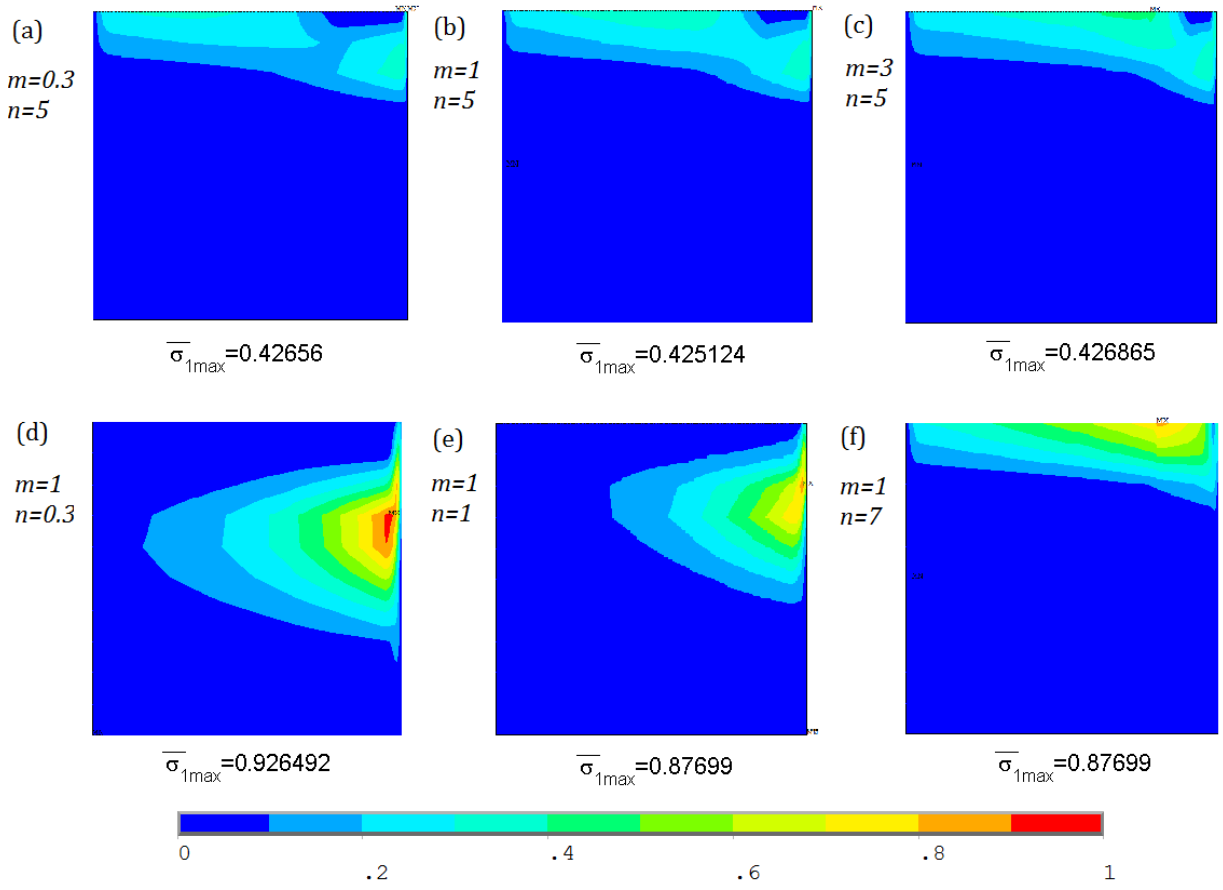

Figure 64. Normalized stress distributions for different m and n values

Because of FGM's non-homogeneous nature, we propose to use the failure criteria instead of stress as a measure of FGM's thermoelastic performance as the material may not fail at maximum stress.

4.2 COMPARISONS WITH HOMOGENEOUS MATERIAL AND 1D FUNCTTIONALLY GRADED MATERIAL

In the volume fraction law, if m=0, the volume fraction of Al_2O_3 is 0. The material will reduce to 1D FGM, comprised of ZrO_2 and Ti-6Al-4V. If m=n=0, the material would be homogeneous, comprised of ZrO_2.

Next we compare homogeneous material with 1D and 2D FGM, corresponding to cases when m=n=0, m=0, n=5 and m=1, n=5 respectively. Temperature distributions are shown in Figure 65. We can see that homogeneous material has the largest high temperature region. As Ti-6Al-4V is added in the 1D FGM, area of high temperature region reduces. By adding Al_2O_3 to form 2D FGM, the area is further reduced. Thus we can prove 2D FGM has better high temperature resistance.

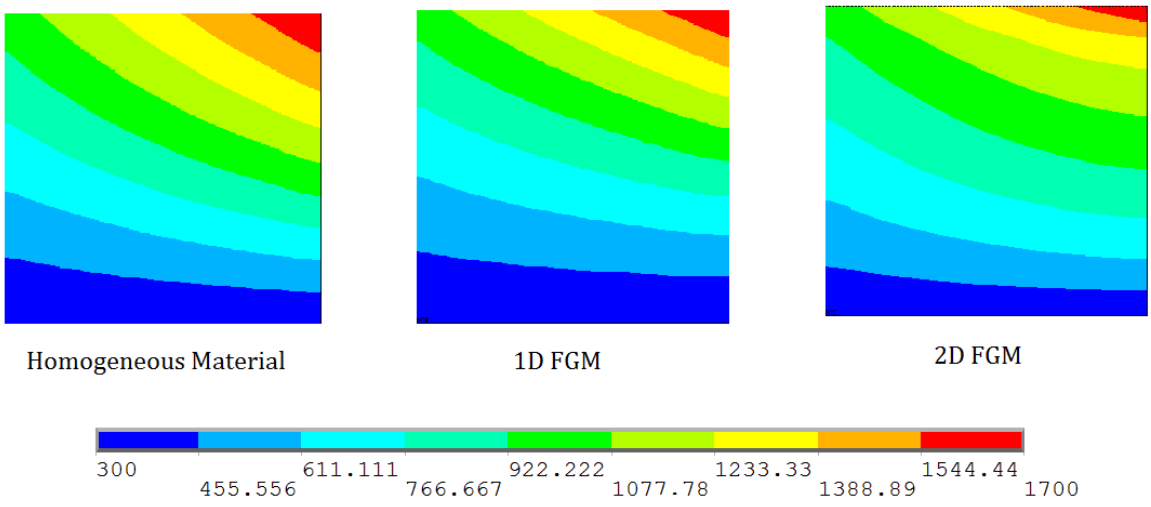

Figure 65. Temperature distributions for different materials

Normalized first principal stresses are shown in Figure 66. Homogeneous material has the highest value of 0.8449 and for 2D FGM it's only 0.4251, which means that 2D FGM is less likely to fail than 1D FGM or homogeneous material. Thus it is necessary to develop 2D FGM to achieve better thermos-elastic performance at high temperatures.

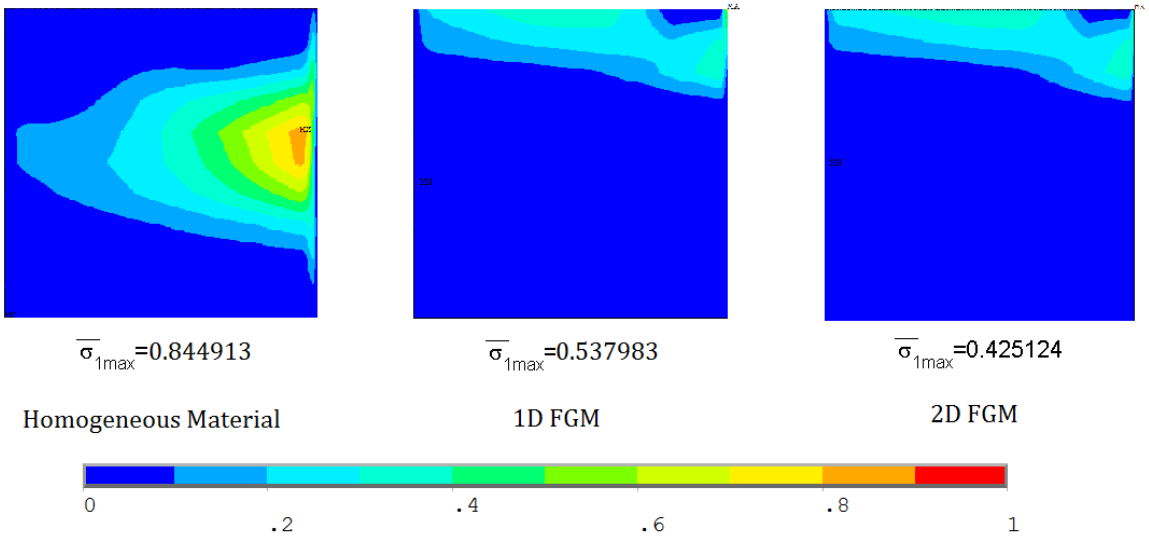

Figure 66. Normalized stress distributions for different materials

4.3 INFLUENCE OF PLATE SHAPE

With a given law of volume fractions, the geometry of the FGM plate will also affect how material properties vary through the plate. The following studies investigate how the plate shape will affect temperature and stress distributions. Let the plate thickness t=15mm and vary its length l, the length over thickness ratios are shown in Table 4 below. We have studied case (c) previously, that is when l=300mm.

Table 4. Plate length/width ratios

case	(a)	(b)	(c)	(d)
l/t	1	10	20	50

Assuming the volume fraction law follows the optimal values obtained above for l/t=20, that is when m=1 and n=5. Top surface temperature also varies linearly from 1000K to 1700K from left to right. Other boundary conditions remain the same. The plate shapes vary from a square in (a) to a narrow rectangular in (d). To make comparisons easier, the plate's x and y coordinates are normalized by its dimensions in the following plots.

Temperature distributions for each different case are shown in Figure 67. We can see that they look very similar after their shapes are normalized. There are only some minor differences in the contours.

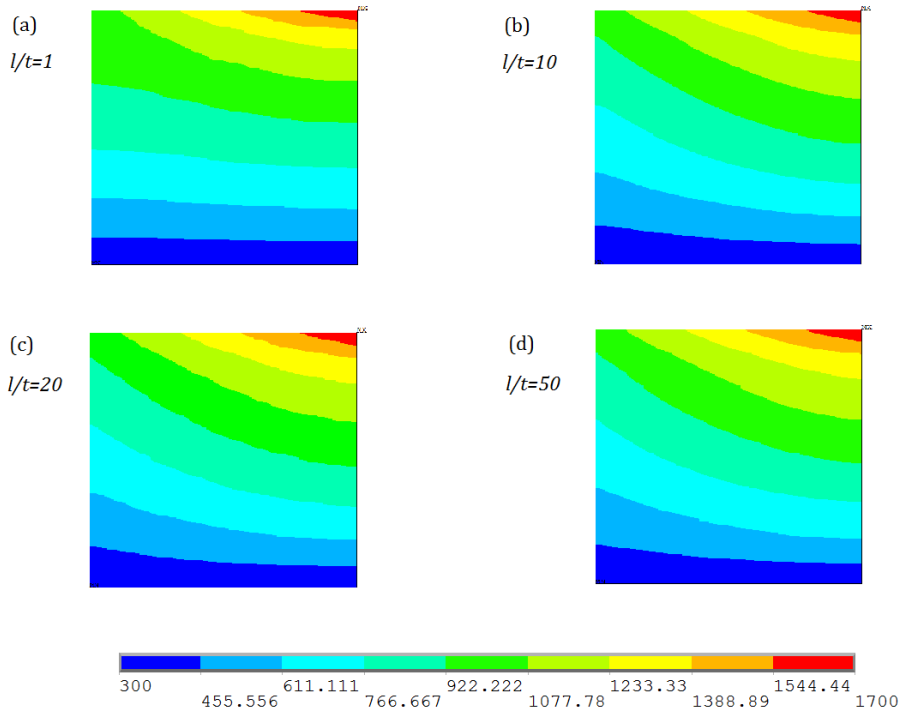

Figure 67. Temperature distributions for different l/t ratios

Normal stresses in x-direction are shown in Figure 68. It can be seen that the maximum tensile and compressive stresses increase slightly with the plate's length.

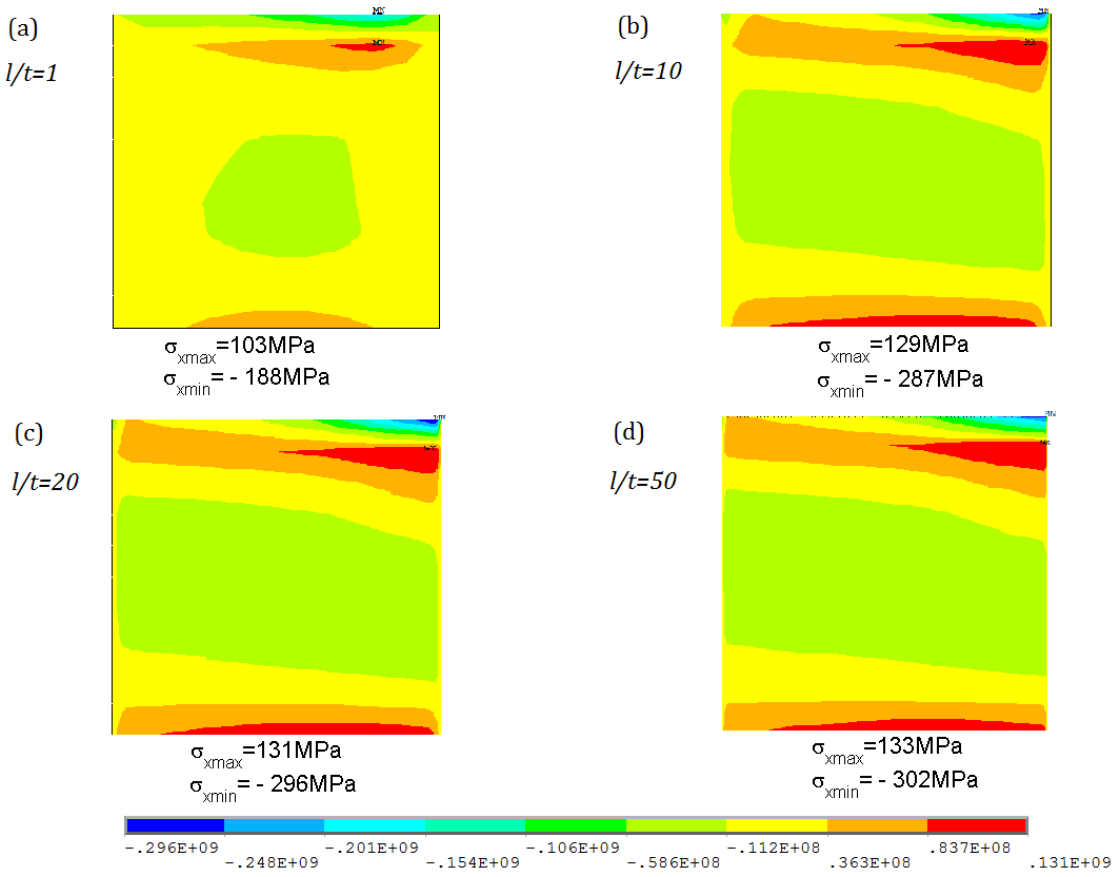

Figure 68. Stress distributions for different l/t ratios

Normalized first principal stresses are shown in Figure 69. Similarly, they only have slight differences. Thus we can conclude that with a given law of material distributions, a FGM's plate shape does not play an important role in its performance.

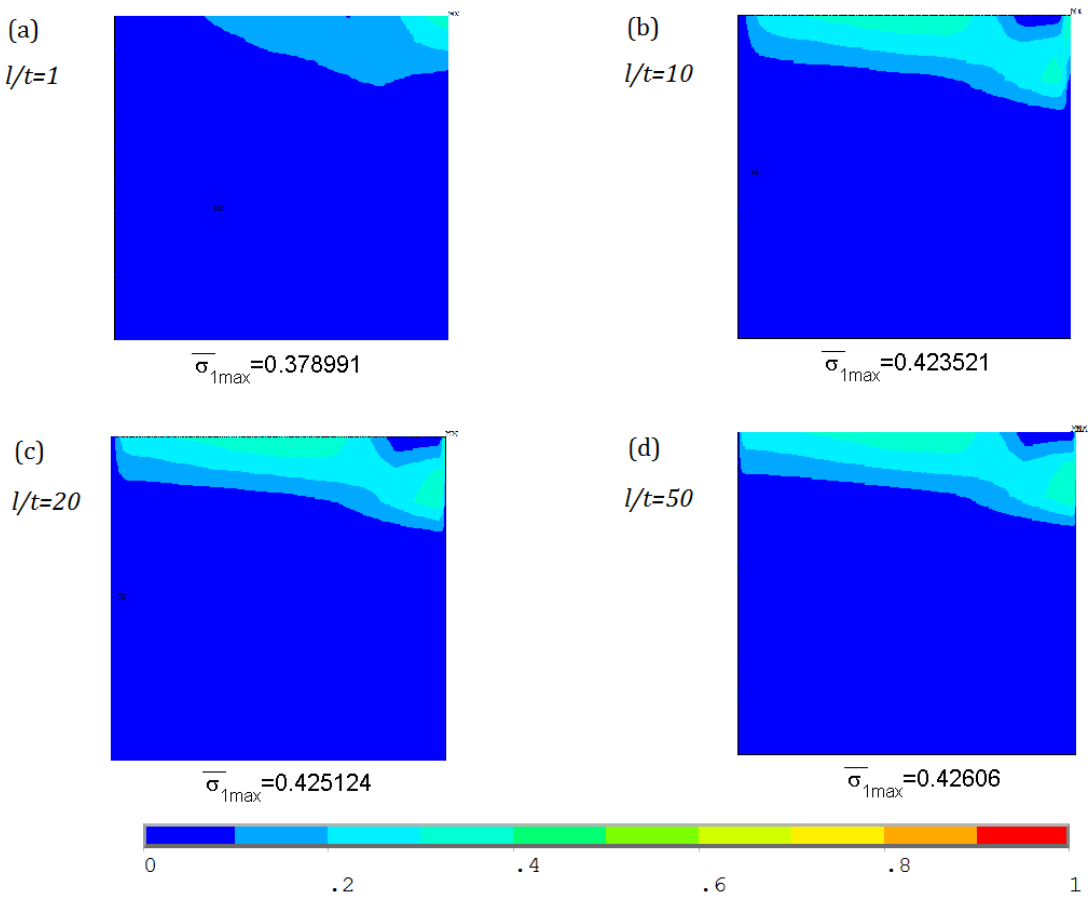

Figure 69. Normalized stress distributions for different l/t ratios

4.4 CLAMPED BOUNDARY CONDITIONS

Boundary condition is another important factor of the analysis. By switching to clamped boundary conditions as shown in Figure 70, we will compare the results with formerly obtained ones with simply boundary conditions. Assuming the plate's dimensions remain *l*=300mm and *t*=15mm and m=1, n=5 in volume fractions laws. Using the same temperature initial conditions as above, note that clamped boundary conditions will only affect structural analysis.

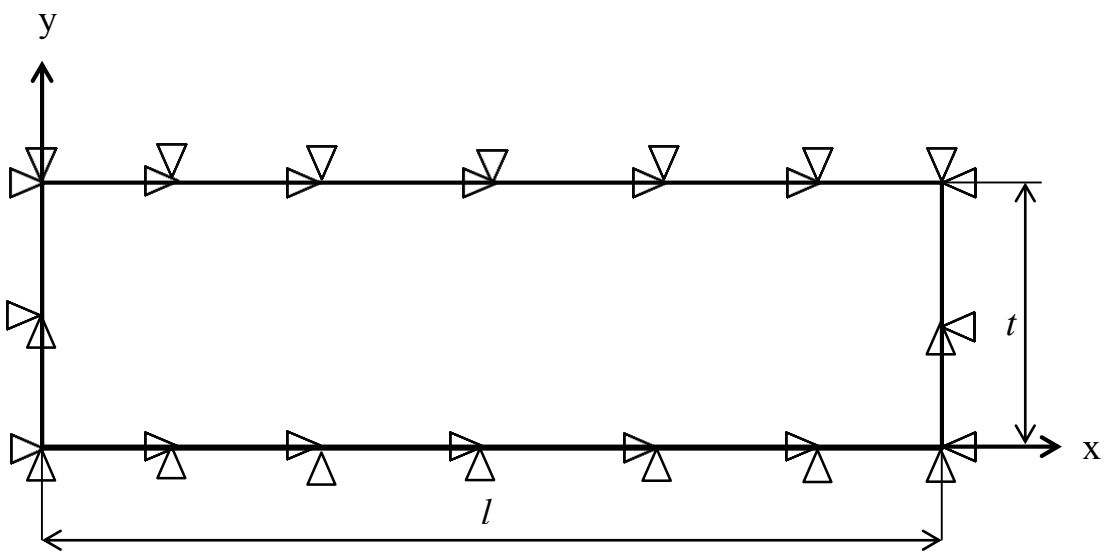

Figure 70. Clamped boundary conditions

Normal stresses in x-direction are shown in Figure 71. We can see that the entire plate is in compressive stress state. This is because more constraints tend to induce higher thermal stresses. The values shown are negative and we discuss their absolute values in the following. The maximum compressive stress value is 2900MPa, which is 10 times higher than the case with simply supported boundary conditions. As shown in the picture, the stress value decreases from surface to bottom. That is because the top regions have higher temperatures, which will cause higher thermal stresses.

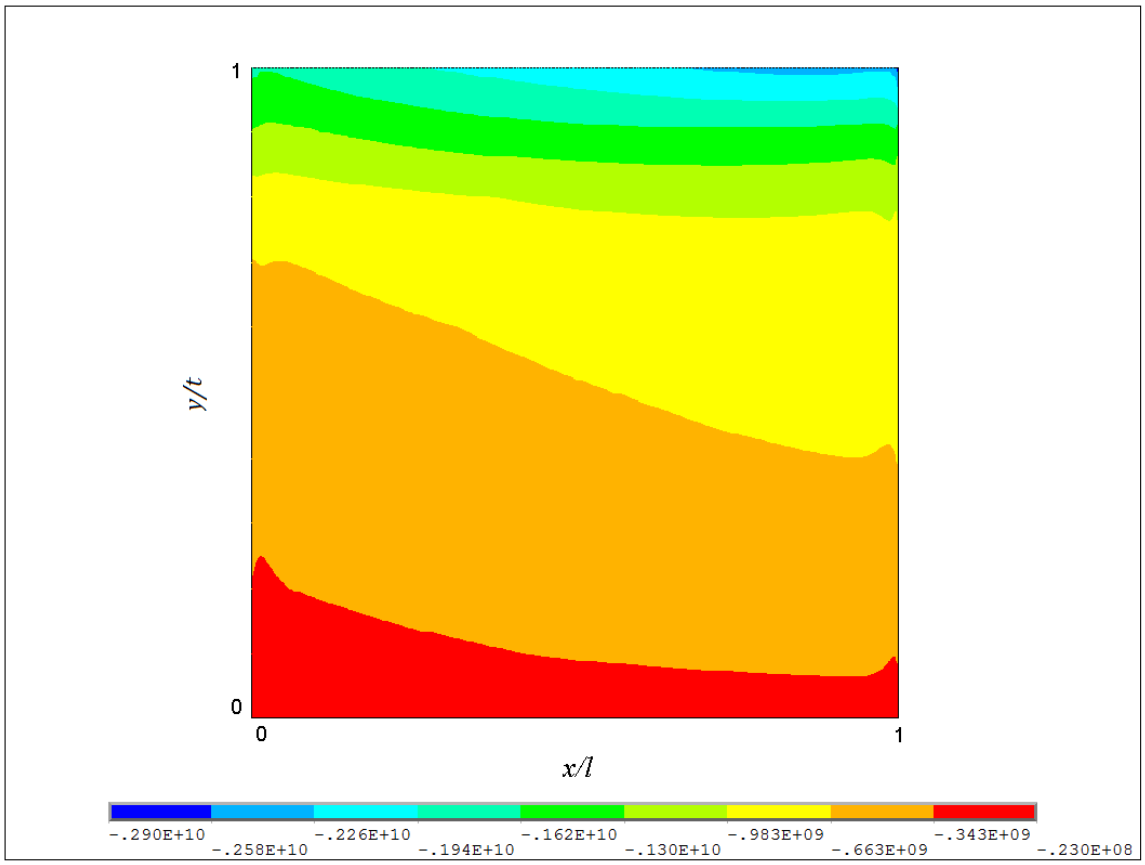

Figure 71. X-direction stress under clamped boundary conditions

It is worth noting that normal stresses in y-direction also greatly rise with clamped boundaries, as shown in Figure 72. It is because more constraints are introduced in y-direction. The Maximum value is 2830MPa. Previously it is only 108MPa.

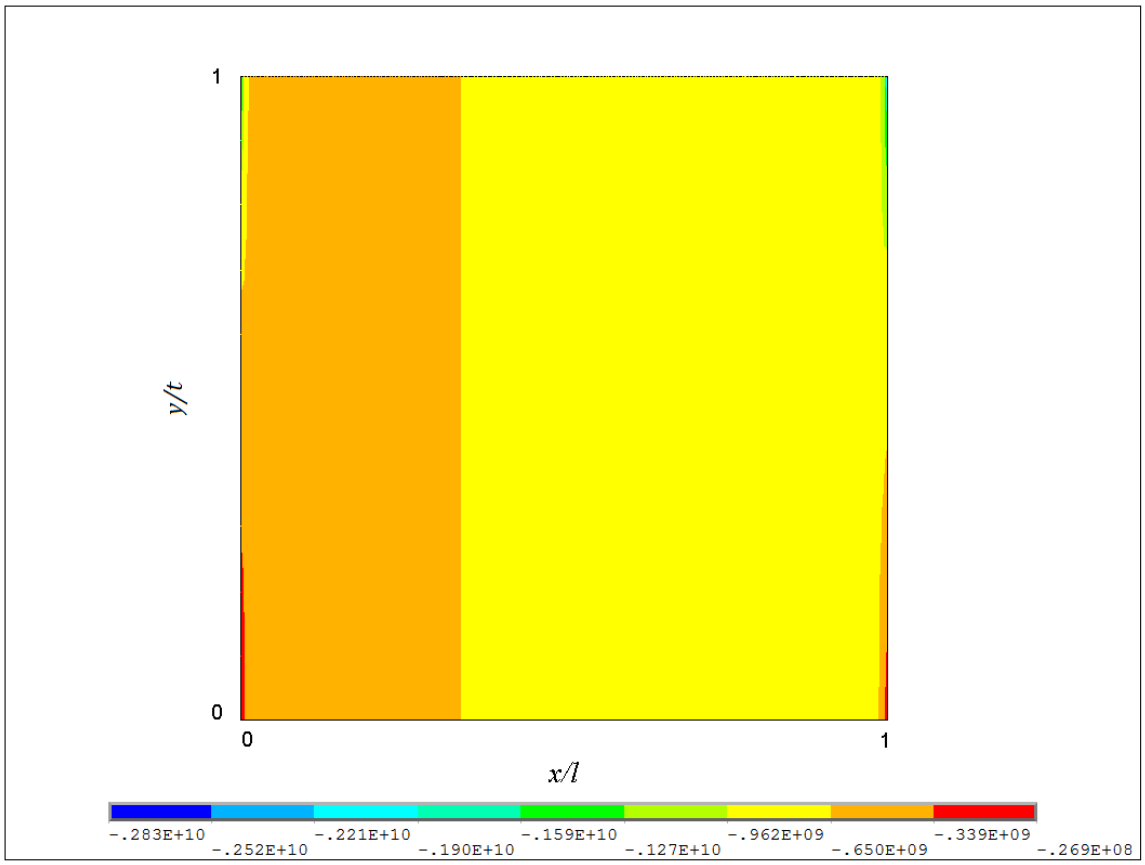

Figure 72. Y-direction stress under clamped boundary conditions

Since stresses in x and y directions are of comparable values, principal stresses do not depend mainly on σ_x as in the simply supported case anymore. Second principal stress is in compression and it is shown in Figure 73. The maximum value is 2910MPa and it happens at upper right corner where the temperature is highest and there are constraints in both x and y directions.

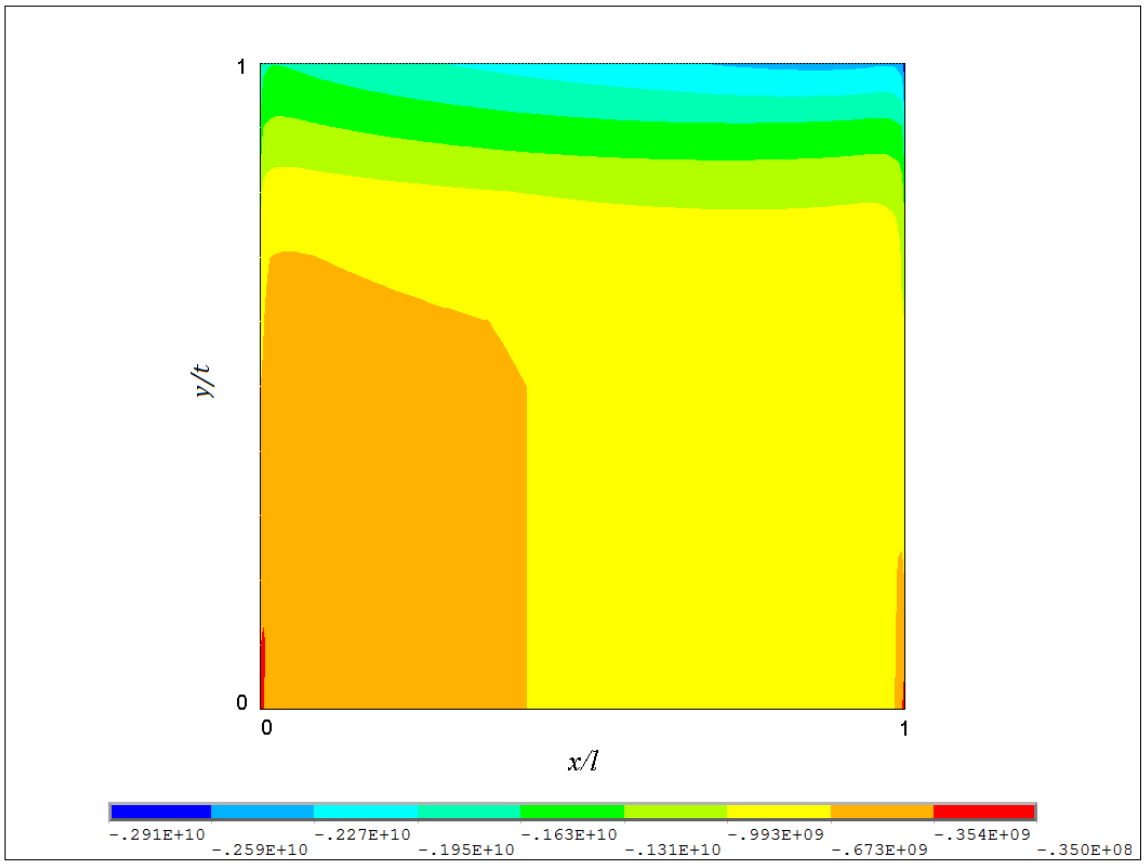

Figure 73. Second principal stress under clamped boundary conditions

Normalized second principal stresses are shown in Figure 74. The maximum value is -3.5, which indicates the material will fail in compression. The failure will occur at the upper right corner, where temperature and stress are also the highest. To avoid high thermal stresses, it is important to reduce constraints as much as possible.

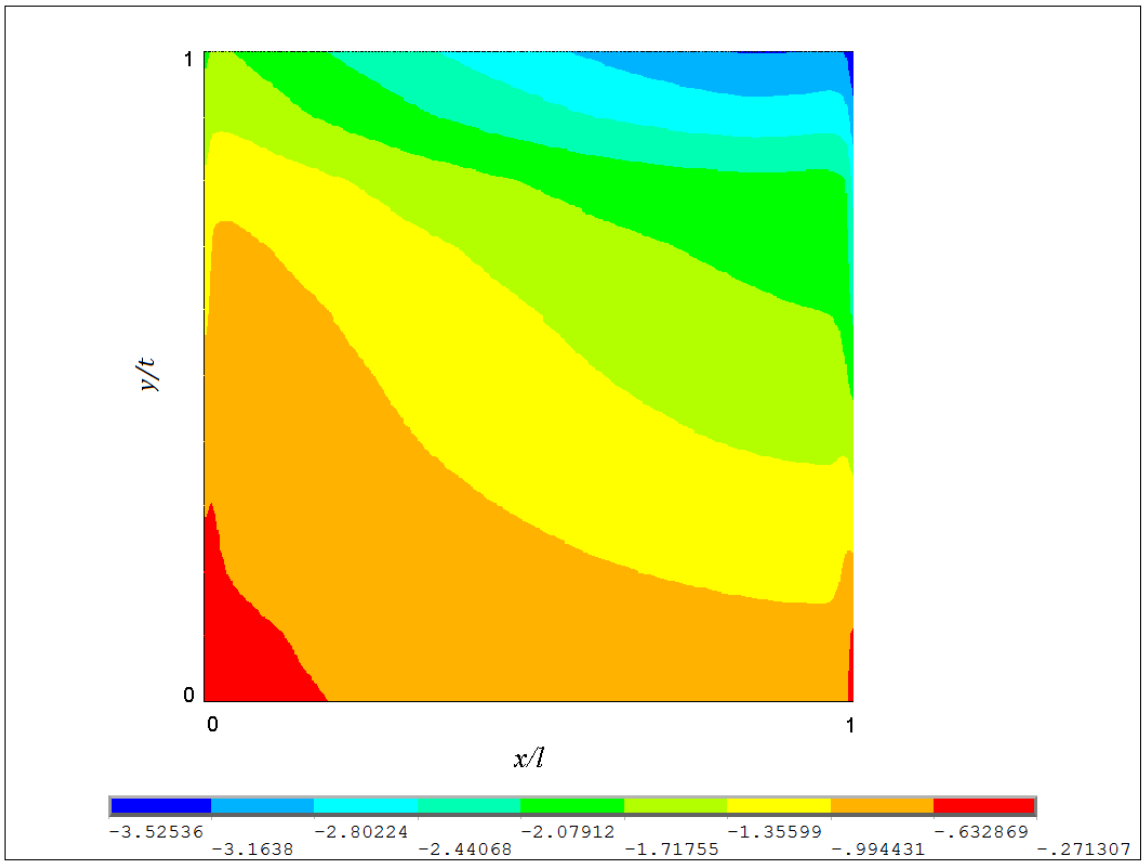

Figure 74. Normalized stress under clamped boundary conditions

5.0 CONCLUSIONS AND DISSCUSSIONS

In this study, thermoelastic behaviors of a multi-dimensional FGM plate comprised of ZrO_2, Ti-6Al-4V and Al_2O_3 with temperature-dependent material properties estimated by the modified WT model were analyzed. First we obtained temperature-dependent thermophysical material properties for ZrO_2, Ti-6Al-4V and Al_2O_3. Next we compared different rule of mixtures for material property estimation and determined that the WT model is the most eligible one. We modified WT model for spatially transitioning FGMs expanded it for three materials systems.

Using the material properties obtained from the modified WT model, we performed thermoelastic analysis for a two-dimensional FGM plate using finite element method. Temperature distributions, thermal stresses and failure criteria of the plate under heating and sudden cooling conditions are analyzed. During the entire heating-cooling cycle we find stress in x-direction is much larger than that in y-direction and shear stress. Thermal stresses greatly rise during the beginning of sudden cooling and the material is most likely to fail at that moment.

We also analyzed other design parameters such as shape of the plate and volume fraction laws. As a result, we obtained the optimal volume fraction function that would lead to the smallest possibility of failure. Volume fraction law, in other words, FGM's structure, has a great influence on its thermoelastic performance. We find that plate shape does not have as much influence on temperature and stress distributions compared as volume fraction law.

Under clamped boundary conditions, thermal stresses can rise as high as 10 times due to more constraints.

The main contributions of this dissertation include:

(1). Wakashima-Tsukamoto model is modified to account for material composition transitions in functionally graded material, in order to provide more appropriate estimation of material properties. The WT model is also expanded to include more materials.

(2). The development of a finite element program for multi-dimensional functionally graded materials. This program allows user defined temperature-dependent material properties to be calculated by the modified WT model and varied with a user specified volume fraction law in two directions. This input file is written in ANSYS APDL format and is included in Appendix A. Using this readily developed model, future users can easily perform thermoelastic analysis for other materials or under other thermoelastic initial or boundary conditions by just changing several input parameters in the program.

(3). Failure analysis using normalized stress. As proved in this dissertation, only analyzing stress can not accurately predict when and where failure will occur for a FGM, as material strength is different at each location. By normalizing principal stresses with a critical stress, we can evaluate each position's failure criterion with respect to its own unique composition.

(4). The thorough investigation of a two-dimensional functionally graded materials with temperature dependent material properties. The development of a multi-dimensional FGM is crucial to adapting working conditions that involve 2D or 3D temperature gradient. Also, temperature dependent material properties are of vital importance to the accuracy of thermoelastic analysis, as material properties change greatly with temperature. We investigated

normal and shear stresses in different directions to find that stress in x-direction is more significant. We also found that volume fraction law has the most impact on FGM's thermalelastic performances than its shape. By examining different values of power law indices in the volume fraction law, we found an optimal FGM structure that has the lowest possibility of failure. Clamped boundary conditions can induce much higher thermal stresses.

Future studies can be focused on further investigation of the optimization problem. In this study we assumed volume fractions follow power laws and used power law indices as optimization parameter. Given more resources and computing time, one can directly calculate each position's volume fraction, and thus obtain a more convincing optimal structure.

Also, during the course of this study, we read the extensive literatures on FGMs and found that most of them are theoretical and numerical studies. Experimental data are rarely seen. Thus sometimes it is hard to validate the legitimacy of certain assumptions and models. There are many different popular approaches, but it is hard to justify which one is more applicable without comparing them to experimental data. To address this issue, more efforts should be made to experimental studies.

APPENDIX A

ANSYS APDL INPUT FILE

```
/FILNAME,FT1,1                  ! new file name FT1
/GRAPHICS,FULL
KEYW,PR_SET,1
KEYW,PR_THERM,1                 !Thermal analysis
/PREP7
*DIM,E1,ARRAY,5,,, , ,          !Material properties
E1(1)=266e9,255.2e9,244.4e9,236.3e9,228.2e9
*DIM,E2,ARRAY,5,,, , ,
E2(1)=386.9175e9,365.9175e9,344.9175e9,329.1675e9,313.4175e9
*DIM,E3,ARRAY,5,,, , ,
E3(1)=105.75e9,83.15e9,60.55e9,43.6e9,26.65e9
*DIM,Mu1,ARRAY,5,,, , ,
Mu1(1)=0.3426,0.3554,0.3682,0.3778,0.3874
*DIM,Mu2,ARRAY,5,,, , ,
Mu2(1)=0.2411,0.247,0.2537,0.2594,0.2656
*DIM,Mu3,ARRAY,5,,, , ,
Mu3(1)=0.2986,0.3114,0.3242,0.3338,0.3434
*DIM,k1,ARRAY,5,,, , ,
```

k1(1)=2.0014,2.0291,2.1958,2.4122,2.7068

*DIM,k2,ARRAY,5,,, , ,

k2(1)=10.334,7.3235,6.3719,6.0972,5.9693

*DIM,k3,ARRAY,5,,, , ,

k3(1)=6.2,13,19.8,24.9,30

*DIM,A1,ARRAY,5,,, , ,

A1(1)=6.535e-6,6.427e-6,7.0428e-6,7.9797e-6,9.3238e-6

*DIM,A2,ARRAY,5,,, , ,

A2(1)=7.0595e-6,7.7863e-6,8.2102e-6,8.4526e-6,9.6683e-6

*DIM,A3,ARRAY,5,,, , ,

A3(1)=8.8559e-6,10.0039e-6,10.2911e-6,10.291e-6,10.291e-6

*DIM,D1,ARRAY,5,,, , ,

D1(1)=5600,5557.9,5495.3,5388.5,5199.6

*DIM,D2,ARRAY,5,,, , ,

D2(1)=3935.7,3893.6,3848.5,3814.5,3781.5

*DIM,D3,ARRAY,6,,, , ,

D3(1)=4420,4367.4,4312.6,4273.2,4234.3

*DIM,C1,ARRAY,5,,, , ,

C1(1)=461.407,585.843,627.111,642.984,676.713

*DIM,C2,ARRAY,5,,, , ,

C2(1)=1184,1252,1309.1,1351.2,1393.2

*DIM,C3,ARRAY,5,,, , ,

C3(1)=537.7,639.3,726.9,885.8,1204.2

```
*DIM,kcalc,ARRAY,5,,, , ,

*DIM,ccalc,ARRAY,5,,, , ,

*DIM,dcalc,ARRAY,5,,, , ,

*DIM,ecalc,ARRAY,5,,, , ,

*DIM,mucalc,ARRAY,5,,, , ,

*DIM,acalc,ARRAY,5,,, , ,

*DIM,Ke1,ARRAY,5,,, , ,

*DIM,Ke2,ARRAY,5,,, , ,

*DIM,Ke3,ARRAY,5,,, , ,

*DIM,Ge1,ARRAY,5,,, , ,

*DIM,Ge2,ARRAY,5,,, , ,

*DIM,Ge3,ARRAY,6,,, , ,


*do,nt,1,5                          !Calclate FGM material property using WT model

Ke1(nt)=E1(nt)/(3*(1-2*Mu1(nt)))

Ge1(nt)=E1(nt)/(2*(1+Mu1(nt)))

Ke2(nt)=E2(nt)/(3*(1-2*Mu2(nt)))

Ge2(nt)=E2(nt)/(2*(1+Mu2(nt)))

Ke3(nt)=E3(nt)/(3*(1-2*Mu3(nt)))

Ge3(nt)=E3(nt)/(2*(1+Mu3(nt)))

*enddo

t=0.015                              !plate dimension

l=0.3

RECTNG,0,l,0,t

esize=t/10

nsl=l/esize

nst=t/esize

lesize,1,,,nsl
```

```
lesize,2,,,nst
lesize,3,,,nsl
lesize,4,,,nst
et,1,77
amesh,all
mx=0.3                          !define volume fraction law
my=2
*get,en,element,0,NUM,MAX       !calculate FGM material properties for each element
*DO,ie,1,en,1
gx=CENTRX(ie)
gy=CENTRY(ie)
v3=1-(gy/t)**my
v1=((gx/l)**mx)*(1-v3)
v2=(1-(gx/l)**mx)*(1-v3)
Vs1=V2+V3
Vs2=V1+V3
Vs3=V2+V1
Vs12=V2/Vs1
Vs13=V3/Vs1

*do,nt,1,5
ccalc(nt)=v1*C1(nt)+v2*C2(nt)+v3*C3(nt)
dcalc(nt)=v1*D1(nt)+v2*D2(nt)+v3*D3(nt)

!*******material 1*******          !WT model
Kes1=Ke2(nt)*Vs12+Ke3(nt)*Vs13
Ges1=Ge2(nt)*Vs12+Ge3(nt)*Vs13
As1=A2(nt)*Vs12+A3(nt)*Vs13
```

ks1=k2(nt)*Vs12+k3(nt)*Vs13

ap1=(Kes1*(3*Ke1(nt)+4*Ge1(nt)))/(Ke1(nt)*(3*Kes1+4*Ge1(nt)))

bbp1=(9*Ke1(nt)+8*Ge1(nt))/(6*Ke1(nt)+12*Ge1(nt))

bp1=Ges1*(1+bbp1)/(Ges1+Ge1(nt)*bbp1)

Kep1=Ke1(nt)+((ap1*Vs1*Ke1(nt))*(Kes1-Ke1(nt)))/(V1*Kes1+ap1*Vs1*Ke1(nt))

Gep1=Ge1(nt)+((bp1*Vs1*Ge1(nt))*(Ges1-Ge1(nt)))/(V1*Ges1+bp1*Vs1*Ge1(nt))

Ap1=A1(nt)+((1/Kep1-1/Ke1(nt))*(As1-A1(nt)))/(1/Kes1-1/Ke1(nt))

kp1=k1(nt)+((k1(nt)*Vs1)*(ks1-k1(nt)))/(k1(nt)+(V1/3)*(ks1-k1(nt)))

! *******material 2*******

Vs21=V1/Vs2

Vs23=V3/Vs2

Kes2=Ke1(nt)*Vs21+Ke3(nt)*Vs23

Ges2=Ge1(nt)*Vs21+Ge3(nt)*Vs23

As2=A1(nt)*Vs21+A3(nt)*Vs23

ks2=k1(nt)*Vs21+k3(nt)*Vs23

ap2=(Kes2*(3*Ke2(nt)+4*Ge2(nt)))/(Ke2(nt)*(3*Kes2+4*Ge2(nt)))

bbp2=(9*Ke2(nt)+8*Ge2(nt))/(6*Ke2(nt)+12*Ge2(nt))

bp2=Ges2*(1+bbp2)/(Ges2+Ge2(nt)*bbp2)

Kep2=Ke2(nt)+((ap2*Vs2*Ke2(nt))*(Kes2-Ke2(nt)))/(V2*Kes2+ap2*Vs2*Ke2(nt))

Gep2=Ge2(nt)+((bp2*Vs2*Ge2(nt))*(Ges2-Ge2(nt)))/(V2*Ges2+bp2*Vs2*Ge2(nt))

Ap2=A2(nt)+((1/Kep2-1/Ke2(nt))*(As2-A2(nt)))/(1/Kes2-1/Ke2(nt))

kp2=k2(nt)+((k2(nt)*Vs2)*(ks2-k2(nt)))/(k2(nt)+(V2/3)*(ks2-k2(nt)))

! *******material 3*******

Vs31=V1/Vs3

Vs32=V2/Vs3

Kes3=Ke2(nt)*Vs32+Ke1(nt)*Vs31

```
Ges3=Ge2(nt)*Vs32+Ge1(nt)*Vs31
As3=A2(nt)*Vs32+A1(nt)*Vs31
ks3=k2(nt)*Vs32+k1(nt)*Vs31
ap3=(Kes3*(3*Ke3(nt)+4*Ge3(nt)))/(Ke3(nt)*(3*Kes3+4*Ge3(nt)))
bbp3=(9*Ke3(nt)+8*Ge3(nt))/(6*Ke3(nt)+12*Ge3(nt))
bp3=Ges3*(1+bbp3)/(Ges3+Ge3(nt)*bbp3)
Kep3=Ke3(nt)+((ap3*Vs3*Ke3(nt))*(Kes3-Ke3(nt)))/(V3*Kes3+ap3*Vs3*Ke3(nt))
Gep3=Ge3(nt)+((bp3*Vs3*Ge3(nt))*(Ges3-Ge3(nt)))/(V3*Ges3+bp3*Vs3*Ge3(nt))
Ap3=A3(nt)+((1/Kep3-1/Ke3(nt))*(As3-A3(nt)))/(1/Kes3-1/Ke3(nt))
kp3=k3(nt)+((k3(nt)*Vs3)*(ks3-k3(nt)))/(k3(nt)+(V3/3)*(ks3-k3(nt)))

Kef=Kep1*V1+Kep2*V2+Kep3*V3
Gef=Gep1*V1+Gep2*V2+Gep3*V3

ecalc(nt)=(9*Kef*Gef)/(3*Kef+Gef)
mucalc(nt)=(3*Kef-2*Gef)/(6*Kef+2*Gef)
acalc(nt)=Ap1*V1+Ap2*V2+Ap3*V3
kcalc(nt)=kp1*V1+kp2*V2+kp3*V3
*enddo

MPTEMP,1,300,700,1100,1400,1700
MPDATA,EX,ie,1,ecalc(1),ecalc(2),ecalc(3),ecalc(4),ecalc(5)
MPDATA,PRXY,ie,1,mucalc(1),mucalc(2),mucalc(3),mucalc(4),mucalc(5)
MPDATA,KXX,ie,1,kcalc(1),kcalc(2),kcalc(3),kcalc(4),kcalc(5)
MPDATA,KYY,ie,1,kcalc(1),kcalc(2),kcalc(3),kcalc(4),kcalc(5)
MPDATA,KZZ,ie,1,kcalc(1),kcalc(2),kcalc(3),kcalc(4),kcalc(5)
UIMP,ie,REFT,,,300              !Reference Temp
MPDATA,ALPX,ie,1,acalc(1),acalc(2),acalc(3),acalc(4),acalc(5)
```

```
MPDATA,ALPY,ie,1,acalc(1),acalc(2),acalc(3),acalc(4),acalc(5)
MPDATA,ALPZ,ie,1,acalc(1),acalc(2),acalc(3),acalc(4),acalc(5)
MPDATA,C,ie,1,ccalc(1),ccalc(2),ccalc(3),ccalc(4),ccalc(5)
MPDATA,DENS,ie,1,dcalc(1),dcalc(2),dcalc(3),dcalc(4),dcalc(5)

esel,s,elem,,ie
mpchg,ie,ie
allsel,all
*enddo
fini

/solu                          !Solution
LSCLEAR,ALL
SOLCONTROL,ON
ANTYPE,4
TIMINT,ON                      !Transient analysis
TUNIF,300                      !Initial temperature
tref,300
tbotm=300                      !Bottom temperature
nsel,s,loc,y,0
d,all,temp,tbotm
allsel,all
TRNOPT,FULL
EQSLV,ITER,5

nsel,s,loc,y,t                 !Apply heat flux at top surface
SF,all,HFLUX,300000            !heat flux q=300000
allsel,all
```

```
TIME,0.001                !Set 1
AUTOTS,-1
DELTIM,.01,.005,60,0
KBC,1
TINTP,,,,0.75,0.5,0.1
solve

TIME,0.1                  ! Set 2
SOLVE
TIME,0.5                  ! Set 3
SOLVE
TIME,1                    ! Set 4
SOLVE
TIME,2                    ! Set 5
SOLVE
TIME,3                    ! Set 6
SOLVE
TIME,4                    ! Set 7
SOLVE
TIME,5                    ! Set 8
SOLVE
TIME,7                    ! Set 9
SOLVE
TIME,10                   ! Set 10
SOLVE
TIME,20                   ! Set 11
SOLVE
```

```
TIME,30                    ! Set 12
SOLVE
TIME,50                    ! Set 13
SOLVE
TIME,70                    ! Set 14
SOLVE
TIME,100                   ! Set 15
SOLVE
TIME,200                   ! Set 16
SOLVE
TIME,300                   ! Set 17
SOLVE

!***Cooling*************************************************************
LSCLEAR,ALL                !Clear all previous loads

AUTOTS,-1
DELTIM,.01,.005,60,0       !Solution control
KBC,1
TINTP,,,,0.75,0.5,0.1
nsel,s,loc,y,0
d,all,temp,tbotm
allsel,all
LSEL,S,LOC,y,t
SFL,ALL,CONV,1000,,300     !Apply cooling convection, with h=1000, T=300K
allsel,all

TIME,300.001               ! Set 18
```

```
solve
TIME,300.1              ! Set 19
solve
TIME,300.5              ! Set 20
SOLVE
TIME,301                ! Set 21
SOLVE
TIME,302                ! Set 22
SOLVE
TIME,303                ! Set 23
SOLVE
TIME,304                ! Set 24
SOLVE
TIME,305                ! Set 25
SOLVE
TIME,306                ! Set 26
SOLVE
TIME,307                ! Set 27
SOLVE
TIME,308                ! Set 28
SOLVE
TIME,310                ! Set 29
SOLVE
TIME,320                ! Set 30
SOLVE
TIME,330                ! Set 31
SOLVE
TIME,350                ! Set 32
```

```
SOLVE
TIME,370                ! Set 33
SOLVE
TIME,400                ! Set 34
SOLVE
TIME,500                ! Set 35
SOLVE
TIME,600                ! Set 36
SOLVE
TIME,700                ! Set 37
SOLVE
fini

/post1                          !Post processing
/DSCALE,ALL,OFF
/RATIO,1,1,20                   !display non-dimensionalized shape
/UDOC,1,TYPE,OFF                !display settings
/UDOC,1,DATE,OFF
/UDOC,1,TYP2,OFF
/UDOC,1,INUM,OFF
/UDOC,1,BCDC,OFF
/UDOC,1,SURF,OFF
/UDOC,1,BODY,OFF
/UDOC,1,VECT,OFF
/UDOC,1,GWIN,OFF
/UDOC,1,VIEW,OFF
/UDOC,1,PSTA,OFF
/UDOC,1,MISC,OFF
```

```
/TRIAD,OFF
/PLOPTS,MINM,0
/AXLAB,X,x/l
/AXLAB,Y,z/t

SET,FIRST                    !Print result temperature distribution for 1st set
PlNSOL,TEMP

SET,NEXT
PlNSOL,TEMP

SET,FIRST                    !change for different sets
ETABLE,TE1,TEMP,
PlNSOL,TEMP
*get,maxtemp01,plnsol,0,max  !Store results in array
fini

!!!!!!!!!!!!!!!!!!Structrual!!!!!!!!!!!!!!!!!!
```

```
ANTYPE,0
LSCLEAR,ALL

TIME,0.001
tref,300
nsel,s,loc,x,0                          !Simply supported boundary condition
nsel,r,loc,y,0
D,all,UX,0
D,all,UY,0
allsel,all
D,2,UY,0
allsel,all
LDREAD,TEMP,1,, , ,'FT1','rth',' '      !Change for different  steps
SOLVE
FINISH

/POST1
EPLOT
/PBF,TEMP, ,1                           !Display settings
/PBC,ALL, ,0
/REP
SET,FIRST                               !Result for 1st set
PLNSOL, S,1, 0,1.0
*STAT                                   !Show all parameters
```

BIBLIOGRAPHY

Akira Kawasaki, R. W. (2002). Thermal Fracture Behavior of Metal/Ceramic Functionally Graded Materials. Engineering Fracture Mechanics, 69(14-16), 1713–1728.

Alpay Oral, J. L., Gunay Anlas. (2008). Crack Initiation in Functionally Graded Materials Under Mixed Mode Loading: Experiments and Simulations. Journal of Applied Mechanics, 75(5), 051110.

Belytschko, P. K. T. (1996). Analysis of Thin Shells by the Element-Free Galerkin Method. International Journal of Solids and Structures, 33(20-22), 3057–3078.

Ch. Zhang , M. C., J. Wang, X.W. Gao, J. Sladek, V. Sladek. (2011). 3D Crack Analysis in Functionally Graded Materials. Engineering Fracture Mechanics, 78(3), 585-604.

Chen Kang , X. X.-w. (2013). TRANSIENT THERMAL STRESS ANALYSIS OF TWO-DIRECTIONAL GRADED COMPOSITE PLATES. Engineering Mechanics, 30(2), 434-442.

Chuanzeng Zhang , J. S., Vladimir Sladek. (2004). Crack Analysis in Unidirectionally and Bidirectionally Functionally Graded Materials. International Journal of Fracture, 129(4), 385-406.

Cubberly, W. H. (1989). Metals Handbook 9th ed: ASM.

Fumio Watari, A. Y., Fuminori Saso, Motohiro Uo, Takao Kawasaki. (1995). Functionally graded dental implant composed of titanium and hydroxyapatite. Proc. of the Third Int'l. Symp. on Structural and Functioanl Gradient Materials, Presses Polytechniques et Universitaires Romandes, Lausanne, 703-708.

G. W. Goward , D. A. G., R.C. Krutenat. (1994).

G.N. Praveen, J. N. R. (1998). Nonlinear Transient Thermoelastic Analysis of Functionally Graded Ceramic-Metal Plates. International Journal of Solids and Structures, 35(33), 4457-4476.

H. Nguyen-Xuan, L. V. T., Chien H. Thai, T. Nguyen-Thoi. (2012). Analysis of functionally graded plates by an efficient finite element method with node-based strain smoothing. 54, 1-18.

H. Nguyen-Xuana, L. V. T., Chien H. Thaib, T. Nguyen-Thoia, b. (2012). Analysis of functionally graded plates by an efficient finite element method with node-based strain smoothing. Thin-Walled Structures, 54, 1-18.

Hill · R D Carpenter , G. H. P., Zuhair A Munir, Jeffery C. Gibeling. (2002). Fracture Testing of a Layered Functionally Graded Material. Astm Special Technical Publication, 1409, 169–186.

I.V. Ivanov, T. S., D. Pietras. (2013). Crack Propagation in Functionally Graded Strip under Thermal Shock. European Physical Journal-Special Topics, 222(7), 1587–1595.

J.R. Cho, D. Y. H. (2001). Averaging and finite-element discretization approaches in the numerical analysis of functionally graded materials. Materials Science and Engineering, A302, 187-196.

Ji Ying, C. L., C.W. lim. (2009). 3D thermoelasticity solutions for functionally graded thick plates. Journal of Zhejiang University Science A, 10(3), 327-336.

Jorge Abantobueno, J. L. (2006). An Experimental Study of Mixed Mode Crack Initiation and Growth in Functionally Graded Materials. Experimental Mechanics, 46(2), 179–196.

K Y Dai, G. R. L., Kok Meng Lim, Xu Guang Han, Shuyan Du. (2004). A Meshfree Radial Point Interpolation Method for Analysis of Functionally Graded Material (FGM) Plates. Computational Mechanics, 34, 213–223.

Kenji Wakashima, H. T. (1991). Mean-field micromechanics model and its application to the analysis of thermomechanical behaviour of composite materials. Materials Science and Engineering, A146, 291-316.

Kyungsu Na, J. K. (2006). Nonlinear Bending Response of Functionally Graded Plates Under Thermal Loads. Journal of Thermal Stresses, 29(3), 245-261.

L. F. Qian, R. C. B. (2004). Transient Thermoelastic Deformations of a Thick Functionally Graded Plate. Journal of Thermal Stresses, 27, 705-740.

Li, W. K. L. W. H. S. (2000). Numerical Simulations of Large Deformation of Thin Shell Structures Using Meshfree Methods. Computational Mechanics, 25(2-3), 102–116.

M. Nemat-Alla, N. N. (2000). Edge Crack Problem in a Semi-Infinite FGM Plate with a Bi-Directional Coefficient of Thermal Expansion under Two-Dimensional Thermal Loading. Acta Mechanica, 144(3-4), 211-229.

M. NIINO, A. K., R. WATANABE, Y. DOI. (1984). Fabrication of high pressure thrust chamber by the CIP forming method. AIAA Paper No. 84-1227.

M. Steigemann , M. S.-N., M. Fulland, H.A. Richard. (2010). Simulation of Crack Paths in Functionally Graded Materials. Engineering Fracture Mechanics, 77(11), 2145-2157.

Mohammad Bagher Nazari, M. S., Mohammad Reza Eslami, Behrooz Hassani. (2011). Computation of Stress Intensity Factor in Functionally Graded Plates under Thermal Shock. Strojniški vestnik -Journal of Mechanical Engineering, 7-8(57), 622-632.

Morris A. Steinberg. (1986). Materials for Aerospace, US goals for subsonic, supersonic and hypersonic flight and for space exploration call for alloys and composites notable for strength, light weight and resistance to heat. Scientific American, 244.

Munro, R. G. (1997). Evaluated Material Properties for a Sintered α-Alumina. Journal of the American Ceramic Society, 80(8), 1919 - 1928.

Noda, N. (1991). Thermal stresses in materials with temperature-dependent properties. Applied Mechanical Review, 44, 383-397.

Oonishi, H. (1990). Mechanical and chemical bonding of artificial joints. Clinical Materials, 5(2-4), 217-233.

R.C. Batra, B. M. L. (2005). Crack Propagation due to Brittle and Ductile Failures in Microporous Thermoelastoviscoplastic Functionally Graded Materials. Engineering Fracture Mechanics, 72, 1954–1979.

Reddy, J. N. (2000). Analysis of functionally graded plates. Internatonal Journal for Numerical Methods in Engineering, 47, 663-684.

S. Kapuria, M. B., A. N. Kumar. (2008). Theoretical modeling and experimental validation of thermal response of metal-ceramic functionally graded beams. Journal of Thermal Stresses, 31, 759-787.

S.K. Chan, Y. F., M. Grimsditch, Z. Li, M.V. Nevitt, W.M. Robertson, and E.S. Zouboulis. (1991). Temperature dependence of the elastic moduli of monoclinic zirconia. Journal of American Ceramics Society, 74(7), 1742–1744.

Shtrikman, Z. H. S. (1962). On Some Variational Principles in Anisotropic and Nonhomogeneous Elasticity. Journal of the Mechanics and Physics of Solids, 10(4), 335-342.

Shtrikman, Z. H. S. (1963). A Variational Approach to the Theory of the Elastic Behaviour of Multiphase Materials. Journal of the Mechanics and Physics of Solids, 11(2), 127–140.

T. Hirano, J. T., T. Yamada. (1990). On the design of functuonally gradient materials. Paper presented at the Proc. of The First Int'l Symp. on FGM's 90, Tokyo, Japan.

Tada, Y. (1995). Space and aerospace vehicle components.

Tobioka, M. (1989). ACE COAT AC 15 aluminum oxide coated cutting tool for highly efficient machining. Technical Report "Sumitomodenki", 135, 190-196.

Touloukian, Y. S. (1973). Thermophysical Properties of Matter 1: JFI/Plenum.

Voight, W. (1889). Wied, Ann., 38, 573-583.

X. Zhao, K. M. L. (2009). Geometrically nonlinear analysis of functionally graded paltes using the element-free kp-Ritz method. Comput. Methods Appl. Mech. Engrg., 198, 2796-2811.

Y Kuroda, K. K., A Moro, M Togawa. (1991). Evaluation tests of ZrO2/Ni functionally gradient materials for regeneratively cooled thrust engine applications. Ceramic Transactions, 34, Proc, of The Second Int'l Symp. on FGM'92, American Ceramic Society, 289-296.

Y. Miyamoto, W. A. K., B.H. Rabin, A. Kawasaki, R.G. Ford. (1999). Functionally Graded Materials: Design, Processing and Applications: Kluwer Academic Publishers.

Zhong, Z. E., Shang. (2008). Closed-form solutions of three-dimensional functionally graded plates. Mechanics of Advanced Materials and Structures, 15, 355-363.